THE DEVELOPMENT AND PROCESSING OF NOVEL ALUMINUM POWDER METALLURGY ALLOYS FOR HEAT SINK APPLICATIONS

by

Logan Smith

Submitted in partial fulfilment of the requirements
for the degree of Master of Applied Science

at

Dalhousie University
Halifax, Nova Scotia
August 2013

Table of Contents

List of Tables

List of Figures

Abstract

The majority of the aluminum heat sinks produced to date have been processed using a cast or wrought approach. The objective of this research was to investigate the feasibility of producing a competitive heat sink material from aluminum using a PM processing method. Alloying elements were carefully chosen so to minimize their required concentration while yielding a high sinter quality through liquid phase sintering. The selected aluminum alloys were ternary formulations from the Al-Mg-Sn system, ranging in concentration from 0.4-2.0 wt.%. The sintering response of each alloy was quantified through density measurements using Archimedes principal, electron microscopy and chemical analysis. Two methods of thermal analysis were employed in order to determine the thermal conductivity of each alloy. This first consisted of individual analysis of the specific heat capacity (C_p), thermal diffusivity (α) and density (ρ) as a function of temperature for each alloy. The thermal conductivity (K) was subsequently determined through the relationship: $K = C_p \alpha \rho$. The second means of thermal analysis was a direct thermal conductivity measure using a transient plane source (TPS). Results indicated very low levels of porosity for a range of alloy chemistries. The lowest sintered density (96.5% of full theoretical) was attributed to insufficient tin (0.4 weight%). Microstructural analysis confirmed highly dense sintered products with relatively pure α-aluminum grains surrounded by varying concentrations of a tin-based secondary phase. The thermal diffusivity and density of samples were both found to decrease with temperature in a linear fashion. Conversely, the specific heat capacity was found to increase with temperature. The only measured thermal property that appeared to be influenced by the alloy chemistry was the thermal diffusivity (and subsequently the calculated thermal conductivity). Both means of thermal analysis showed high thermal conductivity in alloys with low concentrations of magnesium, demonstrating the significance of having alloying elements in solid solution with aluminum. Overall, several alloys were developed using a press and sinter approach that produced higher levels of thermal conductivity than conventional aluminum heat sink materials.

List of Abbreviations Used

CTE	Coefficient of thermal expansion
DSC	Differential scanning calorimetry
EPMA	Electron probe micro-analysis
LFA	Laser flash analysis
LPS	Liquid phase sintering
OAL	Overall length
PM	Powder metallurgy
RT	Room temperature
STC	Sample temperature control
TPS	Transient plane source
UTS	Ultimate tensile strength
WDS	Wavelength dispersive spectroscopy
XRD	X-Ray diffraction

Acknowledgements

The authors would like to acknowledge the funding support provided by the Auto21 Network of Centers of Excellence via grant 502-CPM. They are also indebted to Dr. Steven Corbin and his research group for their assistance with the instrumentation employed for select thermal property tests, Dr. Bernd Mais (Ecka Granules) for the provision of powdered materials and finally Dean Grijm for his aid in sample preparation.

CHAPTER 1. INTRODUCTION

1.1 Thermal Properties of Metals

It is important to understand the thermal properties of materials as well as the factors that influence them in order to develop new materials with the ability to conduct heat in a more efficient and effective manner. There are three important characteristics that aid in defining the thermal properties of a given material, namely, thermal conductivity, thermal diffusivity and heat capacity as discussed in detail below. Metals are, in general, superior conductors of heat due to their ability to facilitate electrical charge carriers throughout their crystal structure [1]. Due to the relatively low cost, ease of production, and inherently high thermal properties, metals are ideal candidates for heat sink applications.

1.1.1 Thermal Conductivity

Thermal conductivity (K), by definition, is the ability of a given material to conduct heat. Whenever a temperature gradient (ΔT) is established within a material, there is an associated heat flow (q), given by Fourier's Law [2], which is dictated by the material constant 'K'.

$$q = -K\Delta T \tag{1}$$

For example, if a good thermal conductor, such as silver, were to come into contact with a hot surface, more energy, or excitation, would be passed through it compared to a poorly conducting material such as a glass or polymer. In the case of solid materials, excitations in the form of particles or waves are what give rise to this thermal conduction [3]. The two dominant forms of excitation in solid metals are free electron movement (electrical conductivity) and lattice waves (phonons). Therefore, the total thermal conductivity of a material, K, can be expressed as a sum of these two principal components:

$$K = K_e + K_g \tag{2}$$

where K_e is the electronic conductivity and K_g is the lattice conductivity. In most *pure* metallic elements, the contribution of the lattice conductivity term becomes low (~2-

20%) around room temperature, as the conductivity due to electrical charge carriers is dominant [4]. In metallic systems comprised of two or more elements, the lattice conductivity can become more significant at higher temperatures due to the increased order/rigidity of the lattice and subsequently the lower contribution due to electrical charge carriers. As one would expect, the thermal conductivity of solids is greatly affected by temperature, as are the other modes of heat transfer. At lower temperatures, scattering of particle and wave carriers is minimized, however there is far less energy present, resulting in lower thermal conductivity. At elevated temperatures, electrons have more energy and subsequently higher velocity, resulting in a higher probability of collisions and thus conduction reaches a peak. Thermal conductivity becomes difficult to measure experimentally at high temperature due to the increasing contribution of other heat transfer modes such as radiation. It is for this reason that theoretical means of analysis become important in order to predict the behavior of materials at temperatures far exceeding room temperature.

Another important concept in understanding thermal conductivity is that materials are assumed to have a mean free path through which these means of heat transfer can flow. Intuitively, the greater the mean free path (the less obstacles), the better the thermal conduction through a given material will be. For the movement of lattice waves, these obstacles can be other (anharmonic) lattice waves, grain boundaries, second phase particles, dislocations, porosity and other imperfections present within the crystal lattice. Similarly, the flow of electrons can be disrupted by imperfections, second phases with lower electrical conductivity, and of course voids within the material. More specifically, the microstructure of a material becomes very influential towards its thermal conductivity. A study by Barghout et al. [5], displayed in Figure 1, shows that the electrical resistivity of Al-1.5Fe only becomes slightly affected when the grain size is decreased to below 20μm. It is important to note, electrical resistivity (ρ) is the reciprocal of electrical conductivity (σ), which is related to thermal conductivity by the Wiedemann-Franz law, which states:

$$\frac{K}{\sigma} = LT \qquad 3)$$

where L is the Lorenz factor, which is equal to 2.45×10^{-8} $W\Omega/K^2$ [6]. Since electrical resistivity quantifies a materials inherent ability to impede the flow of electrons, and given that metals rely heavily on electrical charge carriers to transfer heat, metals with higher levels of electrical resistivity exhibit lower thermal conductivity.

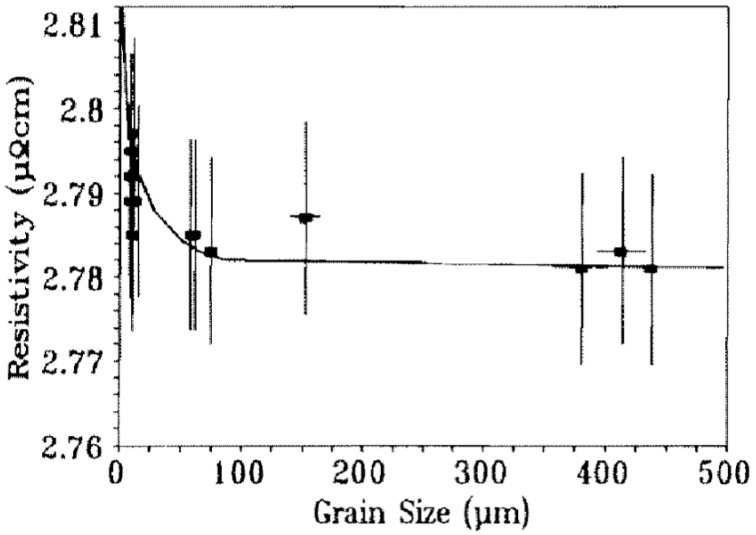

Figure 1. Effect of grain size on electrical conductivity of Al-1.5Fe [5].

In the same study, Barghout analyzed the effect of second phase particles on the overall electrical resistivity of several aluminum-iron alloys using experimental data and Bruggeman's, as analysis shown in Figure 2, below. Bruggeman's analysis relates the volume fraction of second phase particles to the ratio of electrical, and subsequently, thermal conductivity between the matrix and the second phase [5]. This shows that increasing the volume fraction of Al_3Fe particles in an aluminum matrix increases the overall resistivity in a linear manner, effectively decreasing the thermal conductivity. This is due to an increasing disruption of the continuous aluminum matrix. Therefore, a lower mean free path results in increased electron scattering, which increases the electrical resistivity.

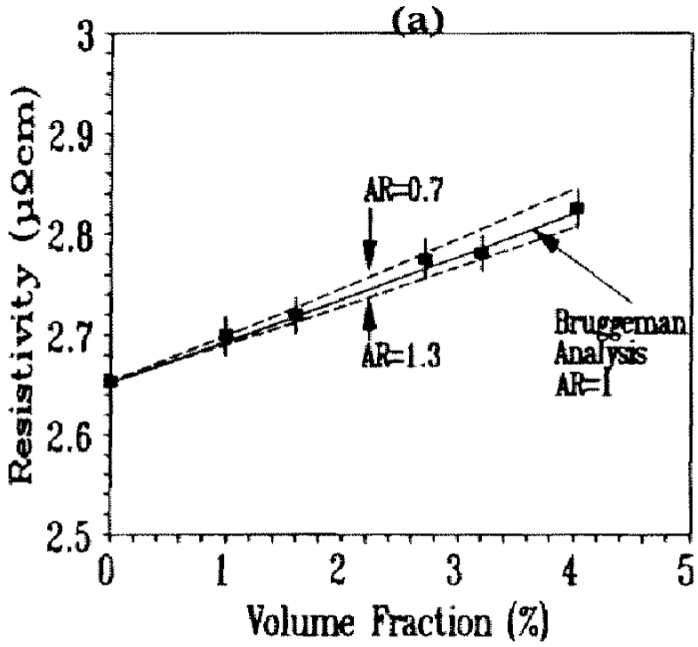

Figure 2. Effect of second phase particles on electrical conductivity [5].

Barghout also analyzed the effect of plastic deformation on several aluminum-magnesium alloys. As Figure 3 illustrates, not only does plastic deformation increase the resistivity in these aluminum alloys, but also it increases with increasing amounts of magnesium present in solid solution. This slight increase in resistivity was attributed to electron scattering by dislocations [5]. Again, this decrease in the mobility of electrical charge carriers, which is so vital in metals, is what causes diminishing thermal conductivity.

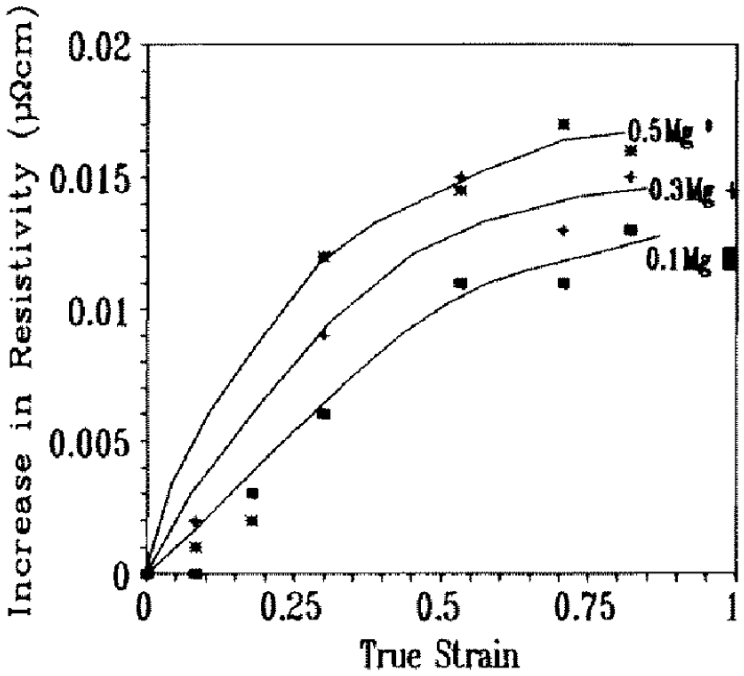

Figure 3. Effect of plastic deformation on electrical resistivity in Al-Mg alloys [5].

Increased amounts of porosity certainly affect the mechanical properties of a material, but they can also have a negative effect on the thermal conductivity. The presence of pores can be treated as a second phase (air) having a far lower *K* than any metal making up the matrix [7]. This is shown in Figure 4 for a cast 380-aluminum alloy, where the thermal conductivity decreases steadily with an increased volume fraction of porosity.

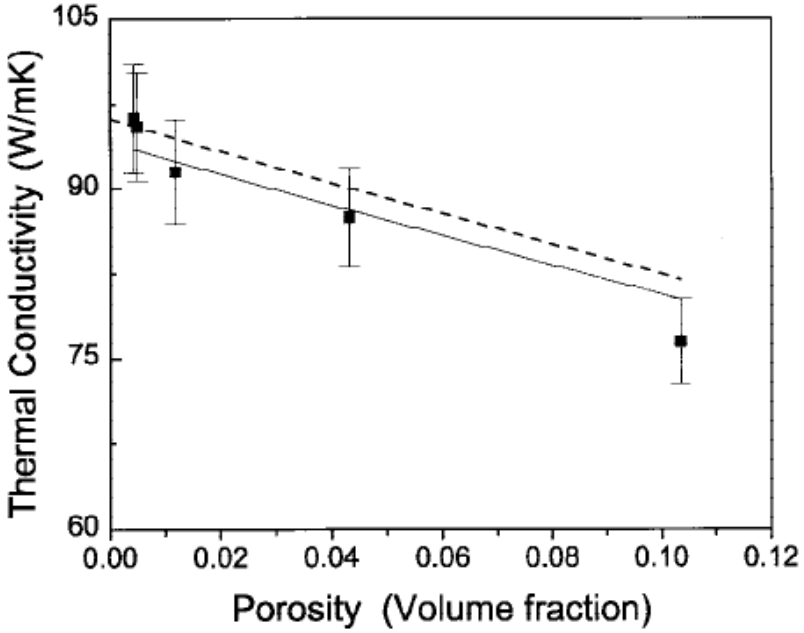

Figure 4. Effect of porosity on *K* for aluminum alloy 380 [7].

1.1.2 Thermal Diffusivity

Another important variable in defining the thermal properties of a material is thermal diffusivity. This is a measurement of the rate at which a material can adapt to a thermal disturbance travelling through it. Whereas thermal conductivity measures the rate at which thermal energy travels through a body, thermal diffusivity deals specifically with the associated rise in temperature measured in m^2/s [8]. Another way of defining thermal diffusivity is by treating it as a diffusion coefficient for the transport of internal energy (constant volume) or enthalpy (constant pressure). When dealing with a material of constant volume, the thermal diffusivity is the proportionality constant relating the transfer of heat (thermal flux) to the internal energy gradient within a solid. Furthermore, heat conduction (q) at constant volume can be quantified by the relationship:

$$q = -\alpha H_v \qquad 4)$$

where H_v is the enthalpy per unit of volume and α is the thermal diffusivity [9].

Isothermal measurement of thermal diffusivity using laser flash analysis (LFA), is a widely accepted method. One example is a Netzsch LFA 427 which uses a vertical

assembly comprised of several key features, including: an atmosphere controlled furnace holding the sample carrier, an IR detector, and a laser system (Figure 5). The furnace can be run in either air or with flowing gas. The incident beam travels along a fiber optic cable from its source and is then focused through a lens and directed toward the sample. The apparatus works by sending a laser pulse through a sample of given thickness (l) and measuring the associated time required for the signal to reach the InSb detector. In order to maintain a stable temperature, the IR detector is cooled with liquid nitrogen. The resulting signal (either ΔV or ΔT) shows an initial pulse followed by a gradual rise to a maximum value (Figure 6). From this information, a simple calculation is used to determine the thermal diffusivity at a given temperature:

$$\alpha = 0.1388\, l^2\, t_{0.5}^{-1} \qquad 5)$$

where $t_{0.5}$ is the half-rise time. The corrected model uses a relative voltage increase and thus calibration to zero is not necessary. The testing process and parameters are discussed in further detail in Section 2.2.

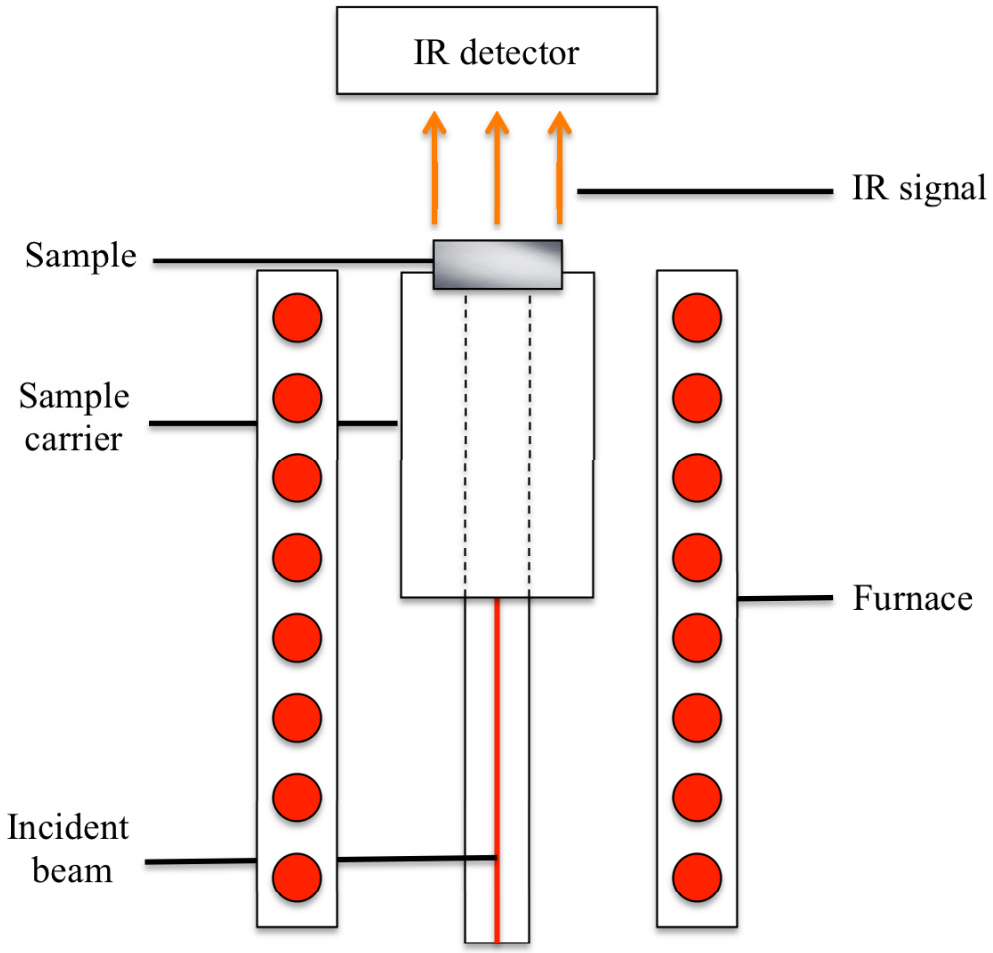

Figure 5. Schematic of a LFA measurement assembly.

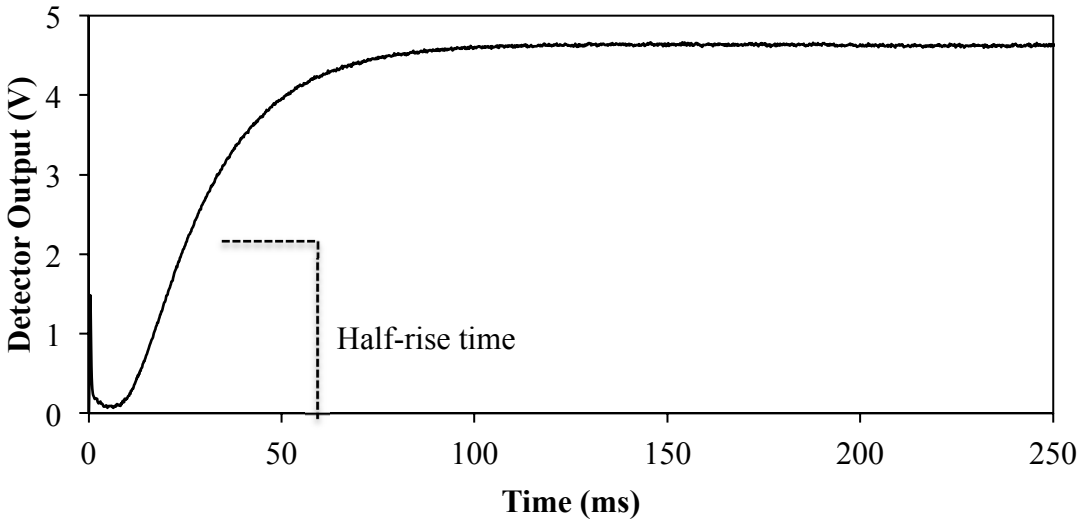

Figure 6. Typical corrected output of a laser shot.

Similar to K, α is also a function of temperature, and in liquids and solids, generally materials showing good thermal conductivity exhibit good thermal diffusivity as well. It is therefore safe to assume that many of the same factors that affect thermal conductivity have a similar effect on α. This cannot always be said for the effect of porosity, which has not been thoroughly studied in the past. Since air has a much higher thermal diffusivity than conductivity, porosity can have less of a detrimental effect on α. This can be seen in Figure 7 where the same 380-aluminum alloy viewed above, shows little to no variation in thermal diffusivity with increased porosity.

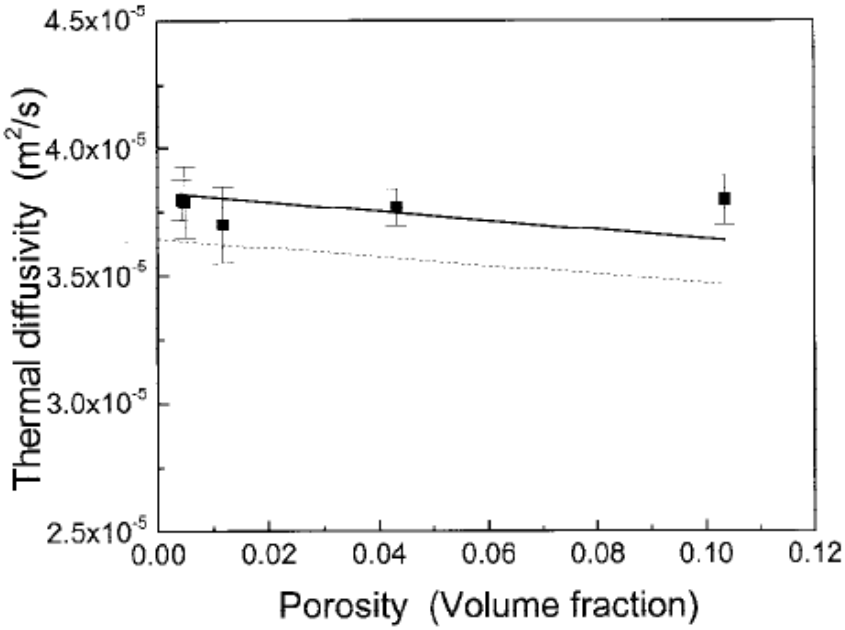

Figure 7. Effect of porosity on α for a 380-aluminum alloy [7].

1.1.3 Specific Heat Capacity

A third important parameter is the specific heat capacity. The specific heat capacity of a material is defined as the amount of energy required to raise the temperature of a given mass by one degree (at constant pressure) and is expressed by the equation:

$$C_p = \frac{Q}{m\Delta T} \tag{6}$$

where Q is the energy applied, m is the mass and ΔT is the resulting temperature change. The specific heat of a metal is not greatly affected by the crystal structure and therefore plastic deformation or alterations in grain size have little effect. A change in temperature, however does affect the heat capacity of a material due to the increase in electron/phonon activity [10]. Since heat capacity is essentially the change in enthalpy with respect to temperature, a more accurate representation of its behavior can be expressed as:

$$C_p = \left(\frac{\partial H}{\partial T}\right)_p \tag{7}$$

where H is the enthalpy of the system [11].

Similar to thermal conductivity, heat capacity has an electronic contribution, as well as a phononic. In terms of the electronic contribution, the heat capacity of a metal is dictated by the number (or density) of thermally excitable electrons at the Fermi level. This is in turn dictated by the Fermi energy of the atoms [12]. Again, the phonon contribution in metals at low temperatures is overshadowed by the electronic contribution and was therefore not discussed in detail.

The specific heat capacity is affected in the same was as thermal conductivity in relation to increasing porosity. This, again, can be attributed to the pores (air) having a lower heat capacity than the matrix, as well as causing increased electron scattering, and effectively lowering the net value, as seen in Figure 8 which includes experimental data along with two theoretical model fits.

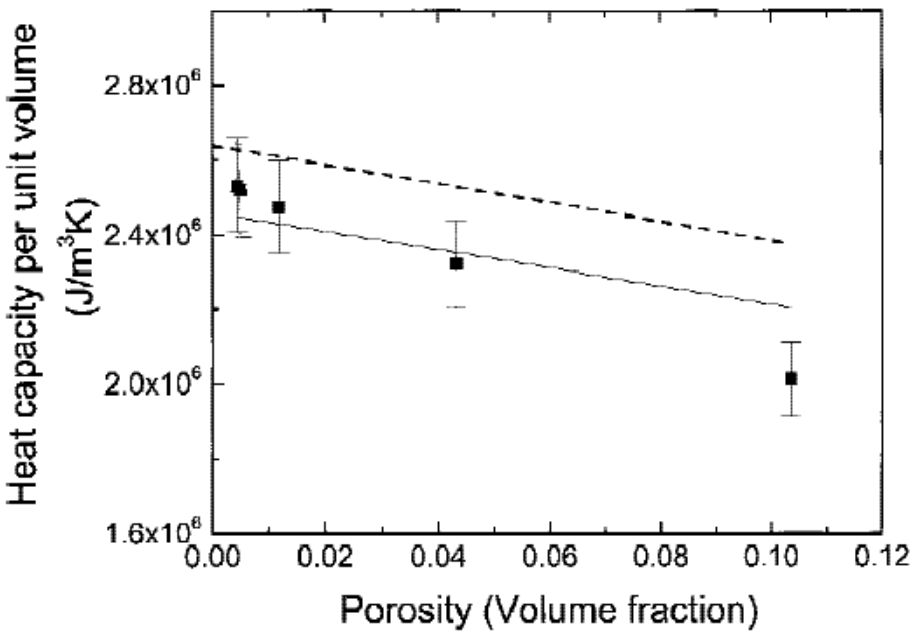

Figure 8. Effect of porosity on C_p for a 380-aluminum alloy [7].

The specific heat capacity of a material can be measured using a differential scanning calorimeter (DSC) (Figure 9). The measurement head consists of a sample carrier, which holds two separate crucibles: one holding the sample, and the other remaining empty.

Attached to the bottom of each crucible holder is a thermocouple that measures the heat flow of each crucible as the assembly is heated in an insulated, atmosphere-controlled furnace. The differential heat flow is then calculated by subtracting the heat effects from the reference crucible as well as the surrounding apparatus. What remains is an accurate measure of the amount of heat consumed (endothermic), or emitted (exothermic), from the sample. In order to calculate the heat capacity, a known standard is first run at a set temperature profile. The unknown specimen is then run using the identical temperature profile and compared with the known standard (Figure 10), always maintaining an empty reference crucible. Using the ratio method, and the data obtained from the two runs, it is possible to determine the heat capacity of the unknown material. It is important to note that the heat capacity can only be measured accurately if the heating rates of the two runs are exactly the same.

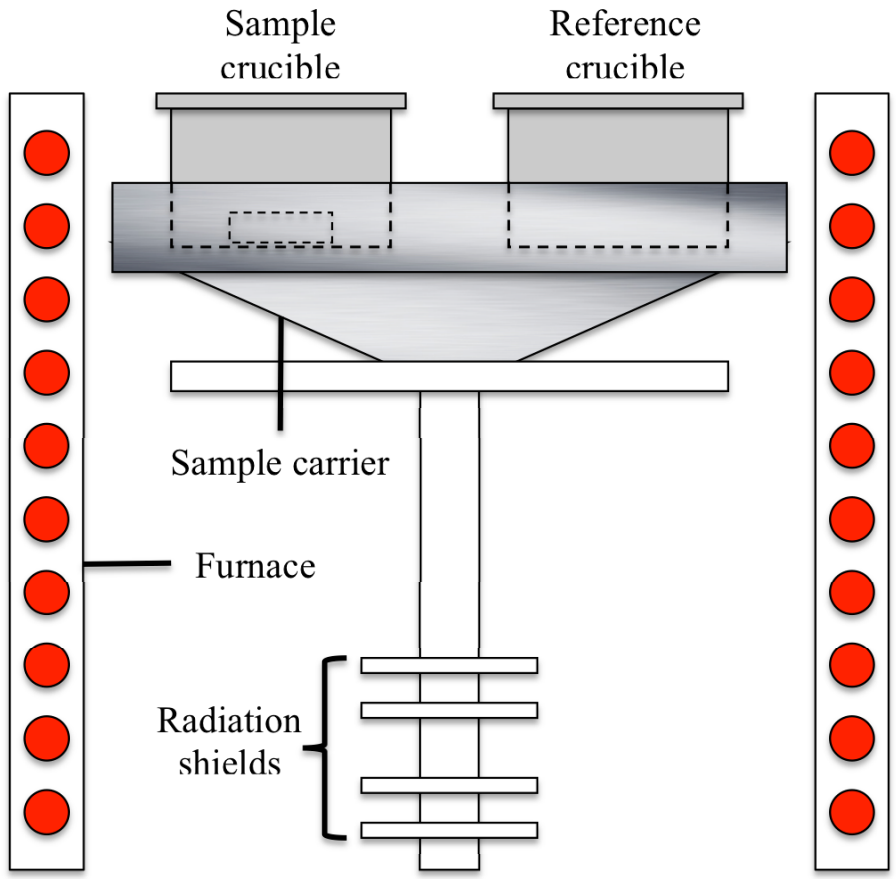

Figure 9. Schematic of a DSC head assembly.

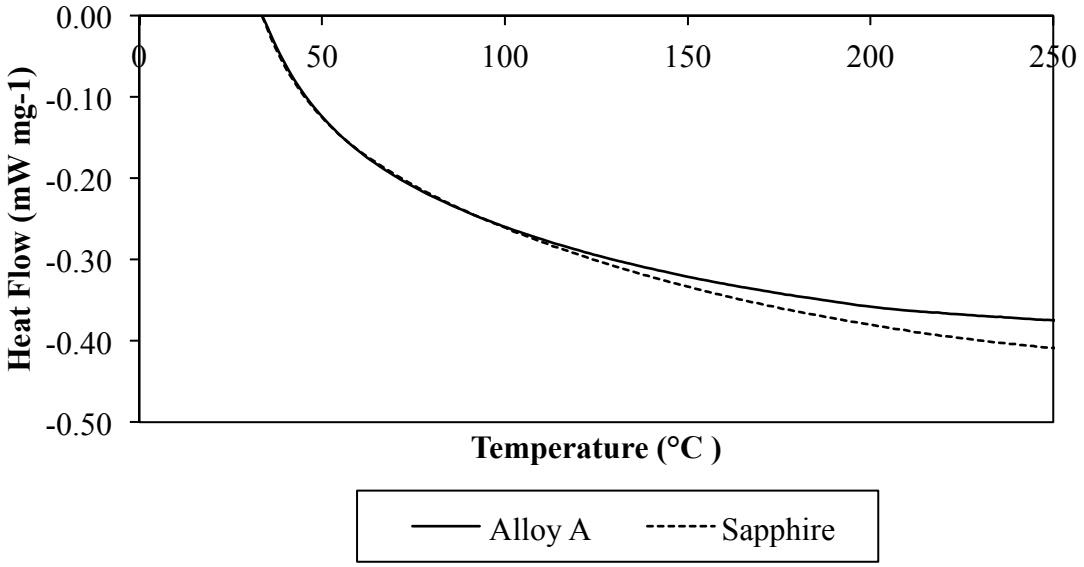

Figure 10. Example of a DSC output signal for an unknown sample (Alloy A) and a known standard (Sapphire).

1.1.4. Thermal Expansion

Thermal expansion is defined as the amount a material expands or contracts upon heating, under constant pressure. Since aluminum does not exhibit negative expansion, the focus of this section is on the phenomenon of positive thermal expansion. Furthermore, materials may not always experience isotropic expansion, resulting in dimensional distortion, however for the sake of this paper, isotropy was assumed.

Due to the complexity of molecular structures, the exact mechanisms of thermal expansion at the atomic level are not well understood. One accepted theory is based on the central force binding adjacent atoms. As a material is heated and the atoms gather energy, they begin to vibrate. Since the vibrations are not in unison (anharmonic), the result is an increase in the mean distance between atomic sites [13]. The volumetric coefficient of thermal expansion (CTE) (α_v) refers to the fraction of volumetric change resulting from changes in temperature (Equation 8).

$$\alpha_V = \frac{1}{V}\left(\frac{\partial V}{\partial T}\right)_p \qquad 8)$$

Similarly, the coefficient of linear expansion represents this change, however in a single dimension as opposed to all three.

Various factors influence the thermal expansion of materials, including point defects (vacancies, impurities and interstitial atoms), alloying elements and phase changes [13] Essentially, anything that alters the atomic structure has some effect on thermal expansion. An example of the effect of alloying elements on the thermal expansion of aluminum is shown in Figure 11. Transition metals, in particular, tend to exhibit unpredictable effects [13] in terms of altering the thermal expansion of the parent material. However, in most cases, adding an element into solution with a lower CTE than the matrix will result in a lower net thermal expansion.

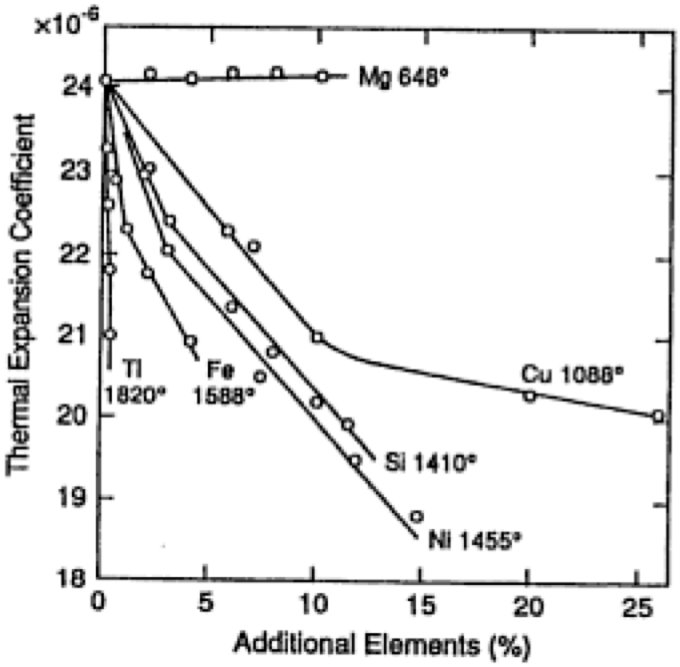

Figure 11. The effect of common alloying elements on the coefficient of thermal expansion of aluminum [14].

There are various techniques used to measure the thermal expansion of materials, from x-ray diffraction to dilatometry, and even visual inspection. X-ray diffraction works through precise measurement of the lattice parameter at various temperatures [15]. A simpler more efficient method of macroscopic analysis is dilatometry. An example of a commercial system designed for this purpose is the Netzsch 402 C dilatometer. The assembly (Figure 12) consists of an insulated furnace with both vacuum and inert gas atmosphere capability encasing the sample chamber. The Al_2O_3 sample chamber contains

a push-rod, connected to a precise (8 nm/digit) transducer which measures the change in length with increasing temperature (Figure 13).

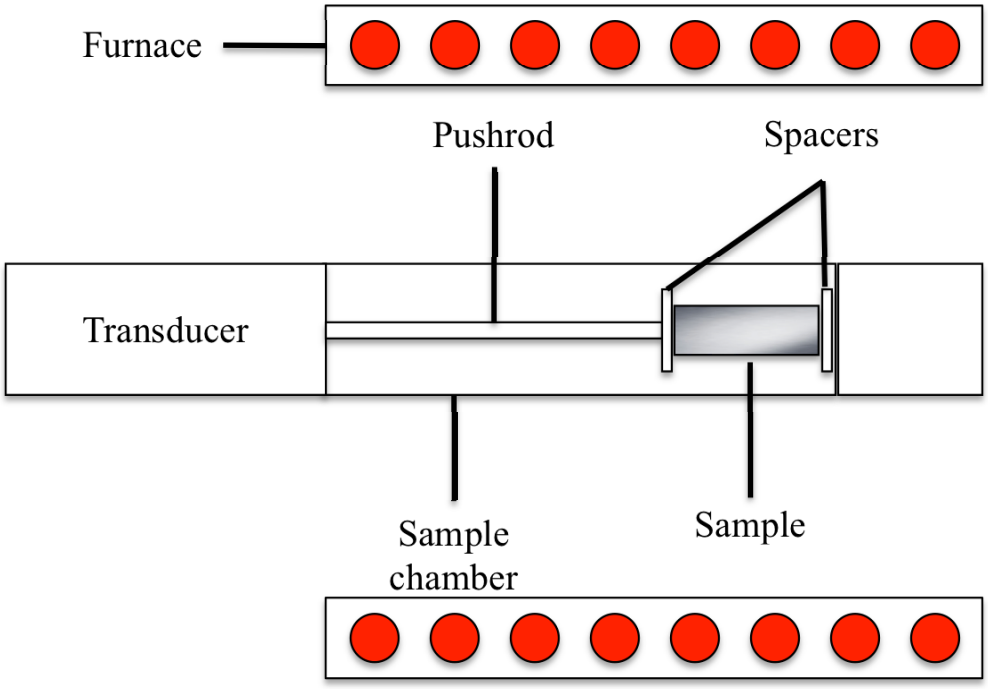

Figure 12. Schematic of a horizontal, push-rod dilatometer.

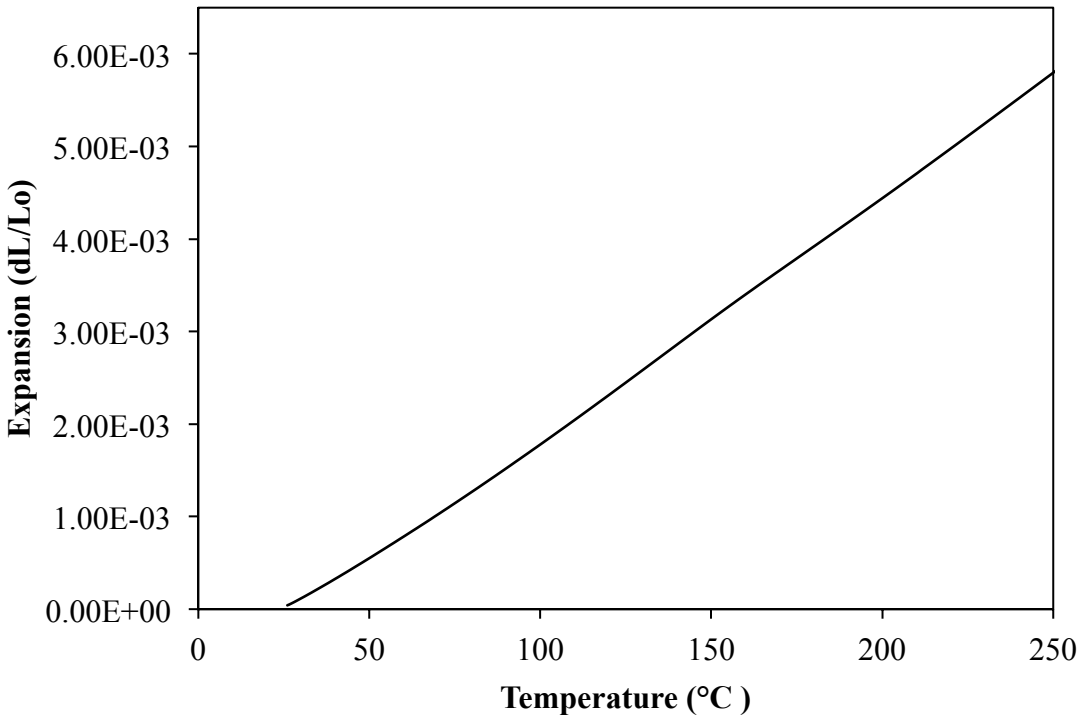

Figure 13. Typical dilatometer data output for a material with positive thermal expansion.

1.1.5 Summary of Thermal Properties

Every material has a corresponding thermal conductivity that can be tailored to a degree through the processing method, thermal or mechanical treatments and/or chemical alterations. The three important parameters, which dictate the thermal properties of a material, are related through equation 9.

$$\alpha = \frac{k}{\rho C_p} \qquad 9)$$

This makes it easy to calculate the thermal conductivity of a material through measuring α and C_p, and knowing the density of the material for any specified temperature through dilatometry. All of these variables are temperature dependent but only α and K are acutely dependent on the microstructure of the material. Table 1 illustrates the differences between K, α and C_p for common metals. It is evident that certain metals, such as aluminum, copper and silver are much better thermal conductors than others. It also illustrates that pure elements are generally more conductive than alloys for the reasons discussed above. The effect of porosity is not very well studied, however it can be

concluded that it will generally have a negative impact on the thermal properties of materials.

Table 1. Thermal properties of common metals and alloys ranging from RT to 100°C [16].

Material	k (W/m-K)	C_p (J/kg-K)	ρ (kg/m^3) x10^{-3}	α* (m^2/s) x10^5
Pure Te	2-3	201	6.24	0.159-0.239
Zr alloys	8-40	280-502	-	-
Gray cast iron	20-80	460	-	-
Pure Sn	52-74	205-238	7.26	3.49-4.28
Cast Al-Cu (2xx.x series)	96-108	875-963	-	-
Wrought Al-Mg (5xxx series)	112-205	879-963	-	-
Pure Mg	153-167	1060	1.74	8.30-9.05
Cast Al-Sn (8xx.x series)	167-184	963	-	-
Wrought Al-Mg-Si (6xxx series)	142-284	887-963	-	-
Pure Al	221-247	895-933	2.70	9.14-9.80
High Cu alloys	80-410	360-420	-	-
Pure Au	292-316	126-130	19.3	12.0-12.6
Cast Cu	346-391	389-420	-	-
Pure Ag	417-428	235-239	10.5	16.9-17.0

*Calculated using equation 3)

1.2 Electrical Conductivity of Materials

As aforementioned, the thermal conductivity of metals is closely related to electrical conductivity through the Wiedemann-Franz law. This is, again, due to the inherently high density of conductive electrons present in metallic bonding. Given this and the relevance of metallic materials to this thesis, the inclusion of a concise overview of electrical conductivity was prudent. Electrical conductivity in solids is caused by the flow of electrons passing through a material. The conductivity of a material depends greatly on the type of bonding, be it ionic, covalent or metallic. Ionic bonding is an electrostatic type of bond resulting from the attraction between two oppositely charged ions. A simple example is in NaCl, where the valence shell of sodium has a single electron and chlorine has seven. It requires little energy to liberate the single electron from sodium, which is

taken by chlorine forming two stable atoms. In doing so, sodium becomes Na^+ and chlorine becomes Cl^-. This results in an attraction, leaving the two ions tightly bound. Therefore, a material with ionic bonding is essentially made up of oppositely charged ions with stable valence shells. Because the valence shells are all stable, it takes a large amount of energy to liberate an electron to create a current and thus results in low electrical conductivity [17]. Ionic bonding is formed between metallic and non-metallic atoms and generally creates insulators with very low electrical conductivity. Figure 14 shows the ionic bond between NaCl.

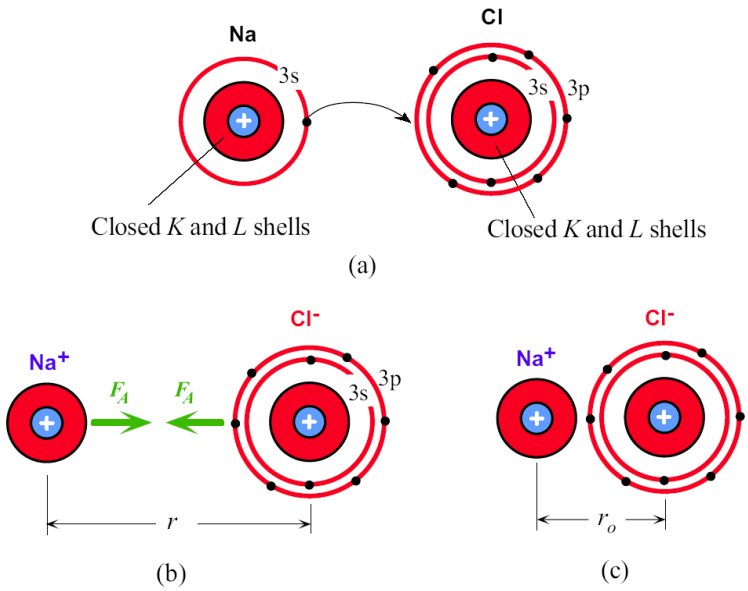

From *Principles of Electronic Materials and Devices, Third Edition*, S.O. Kasap (© McGraw-Hill, 2005)

Figure 14. Schematic of an ionic bond between Na and Cl [18].

Covalent bonding occurs between non-metallic atoms and instead of atoms donating electrons from their valence shells, they share so that they are essentially both stable. The atoms still maintain charge neutrality, therefore, the bond between them is not as strong as ionic. However, energy is still needed to liberate an electron from the valence shell in order to allow conduction. Semiconducting materials are typically covalently bonded. Figure 15 shows the covalent bonding in a single molecule of methane. The valence shell of carbon contains four electrons whereas hydrogen contains only one. For carbon to be stable, four hydrogen atoms must share an electron.

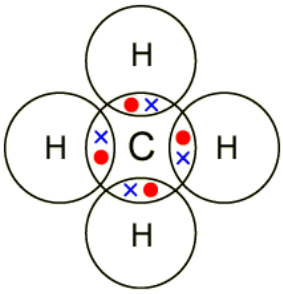

Figure 15. Schematic of covalent bonding between hydrogen and carbon, making methane.

Metallic bonding, intuitively, is the bonding between two metallic atoms. Metals, being on the left portion of the periodic table, have one, two or three valence electrons. When metallic atoms come into contact, there is no way to create a stable outer shell, therefore the electrons essentially form a cloud and are shared by all surrounding cations. The net result of this is that since the electrons are not tightly bound to a single atom, it takes little to no energy to make the material conductive. This is the reason pure metals such as copper or aluminum have such high electrical conductivity, as electrons are able to freely flow throughout the material without having to disrupt any bonding.
Figure 16 shows a typical metallically bonded matrix.

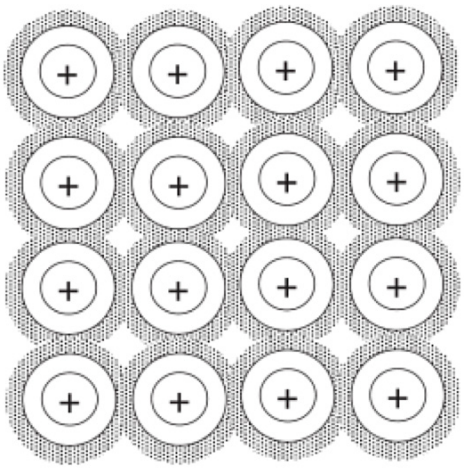

Figure 16. Schematic denoting the metallic bond [19].

When an electric potential difference is applied between, for example, two ends of a metallic wire of a certain length, an electrical field is generated which causes the acceleration of electrons in order to establish equilibrium. Therefore, in addition to the random electron movement throughout the material, this acceleration due to the potential

difference causes another velocity in the direction of the electric field, which causes the flow of electrons (electrical current) [20, 21].

Electrical conductivity (σ) has two contributing factors: charge density ($N_e e$) and mobility (μ_e). Charge density is essentially the amount of mobile electrons in a material, whereas mobility is related to the mean free path. In metals, electrons have relatively low mobility, however there is a huge concentration of electrons giving it a very high charge density [20]. Similar to thermal conductivity, discussed above, there are various factors that affect the electrical conductivity of solid metals. Lattice imperfections, secondary phases and grain boundaries all contribute to scattering of electrons and therefore lower the electrical conductivity. The main contrast between the two parameters is their temperature dependence. Where thermal conductivity increases with temperature, electrical conductivity actually decreases. This is due to the increased lattice vibration and subsequent increase in the probability of electrons colliding with atoms in the crystal structure [22, 23]. Since phonons do not transport electrons, this is where there is a deviation between electrical and thermal conductivity.

Table 2 shows the electrical resistivity of various materials at 300 degrees Kelvin. Again, pure metals show lower resistivity than alloys. This is due to the metallic bonding and single-phase matrix, as previously discussed.

Table 2. Electrical resistivity of various materials at 300K [24].

Material	Electrical Resistivity ρ (Ω-cm)
Copper, annealed	1.67×10^{-6}
Copper, reduced 75% by cold drawing	1.71×10^{-6}
Cartridge brass, annealed (Cu-30Zn)	6.20×10^{-6}
Aluminum, annealed	2.65×10^{-6}
Iron, annealed	9.71×10^{-6}
Constantan (Cu-45Ni)	49×10^{-3}
Nichrome (Ni-20Cr)	108×10^{-3}
Semi-Conductors	
Germanium	10^{-3} to 60
Silicon	10^{-3} to 2.5×10^{-3}
Insulators	
Alumina	10^{13}
Diamond	10^{14}

1.3 Heat Sinks

1.3.1 Principles of Operation and Fabrication

The transfer of heat is underpinned by three key mechanisms – radiation, conduction and convection (natural/forced). Two of these mechanisms come into play when looking at the means of heat dissipation in lower temperature applications (discussed in the following section). In particular, radiation becomes an ineffective method of heat transfer, thus leaving conduction and convection as the dominant forms of heat dissipation [25, 26]. Although Fourier's law describes the flow of energy through a solid, in heat sinks it is important to know the actual change in temperature through a solid, with the general equation being:

$$\frac{\partial T}{\partial t} = \alpha \left[\frac{\partial^2 T}{\partial x^2} + \frac{\partial^2 T}{\partial y^2} + \frac{\partial^2 T}{\partial z^2}\right] \qquad 10)$$

where α is the thermal diffusivity of the material [27]. This can be determined experimentally, and is dependent completely on the material properties. Therefore, when designing a heat sink, to improve efficiency of conduction, it is desirable to have good thermal diffusivity. Convection, however, depends far more on the geometry of the heat sink. Convection is much more complicated to model, and depends on various factors such as the exposed area for convection, the surface characteristics of the material, the

velocity of fluid or gas (if forced convection), and the convective heat transfer coefficient of the fluid or gas [27]. For the purpose of this study, the means of convection are not important, therefore the only variable of interest is maximizing the area for convection. This area is generally amplified using fins. A study by Morrison looked at optimizing heat sink performance by altering the size and spacing of fins, shown below in Figure 17 and Figure 18. This study was done for parallel plates with natural convection, i.e. a passive heat sink. It can be seen that thinner pins are effective to a minimum of ~0.5 mm, and subsequently degrade at a faster rate at smaller thicknesses. In terms of spacing, between 6 and 7.5 mm of free space were found to result in the lowest temperature. This was likely due to the impingement of airflow with closer fin positioning. Larger spacing would effectively decrease the number of pins, resulting in a lower surface area. Again, as the spacing becomes too small, the thermal efficiency drops at a higher rate. So, it is more complicated than simply maximizing the surface area of fins to optimize the heat dissipation by a heat sink.

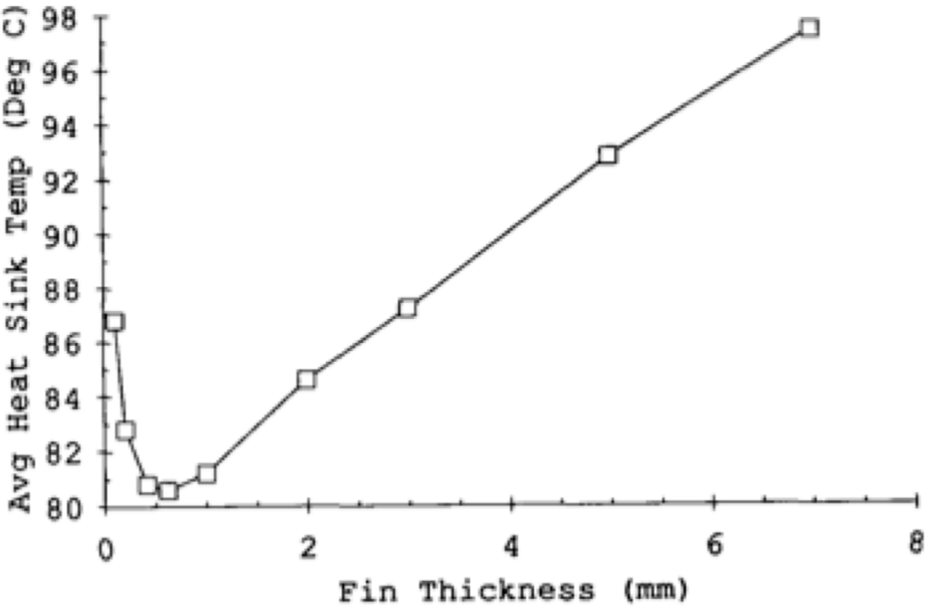

Figure 17. Effect of fin thickness on efficiency of a heat sink [28].

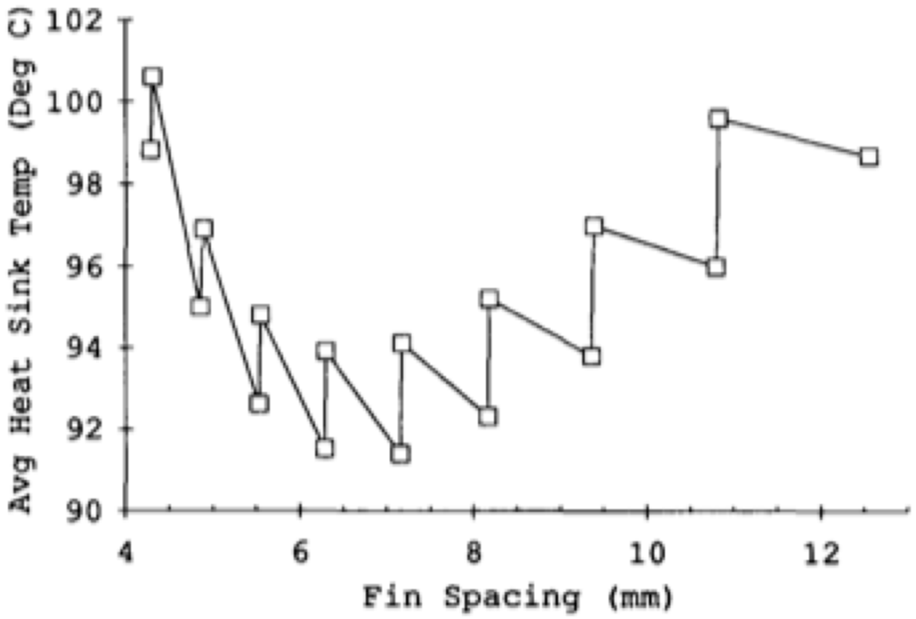

Figure 18. Effect of fin spacing on efficiency of a heat sink [28].

How heat sinks operate is dependent upon the type employed. There are five general categories of heat sinks, organized by their associated cooling methods: passive heat sinks, semi-active heat sinks, active heat sinks, liquid cooled cold plates, and phase change recirculating systems [26]. For the purpose of this research, only the first three categories bear significant relevance. Each is describe in the paragraphs below.

Passive heat sinks provide the most basic form of cooling as they rely solely on natural convection, conduction and radiation. These are typically among the cheapest heat sinks, along with semi-active heat sinks. Due to the lack of forced convection, this type of heat sink is the least effective and can only handle up to approximately 5 W of power, which is ideal for portable electronic devices, but insufficient for higher demands [29]. Passive heat sinks are inherently the most reliable due to the absence of any moving parts. Semi-active heat sinks are similar in design, however, they partly rely on existing airflow from fans within the system and use a mixture of forced and natural convection. Since both active and semi-active heat sinks rely on some form of convection, they generally both incorporate the use of fins or pins in order to maximize surface area. Figure 19 shows

passive/semi-active heat sink design, consisting of a thermally conductive base along with multiple pins.

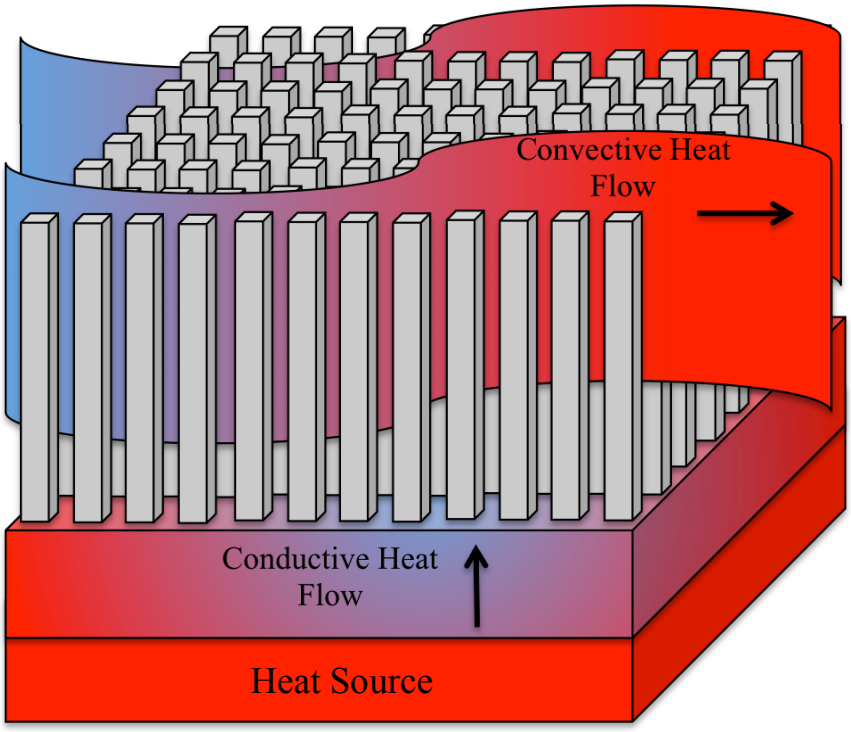

Figure 19. Schematic of a passive or semi-active heat sink.

Fully active heat sinks can dissipate the most heat (~25-60 W) [29], due to forced convection from an attached fan, pump or air-jet (Figure 20). These heat sinks are more expensive and typically less reliable due to the mechanical component. Active heat sinks allow for the use of materials with lower thermal conductivity (i.e. aluminum as opposed to copper) without compromising the energy dissipation capabilities. The most important factors in active heat sinks are the parameters surrounding the fan. Two of these parameters are the internal pressure of the system, which accounts for the thermal resistance and the required flow rate of air [29]. Active heat sinks also offer a degree of variability in terms of their efficiency, depending on the required application. If, for example, the ambient temperature drop warranted less heat dissipation, an active heat sink can easily be converted into a passive heat sink by disengaging the fan.

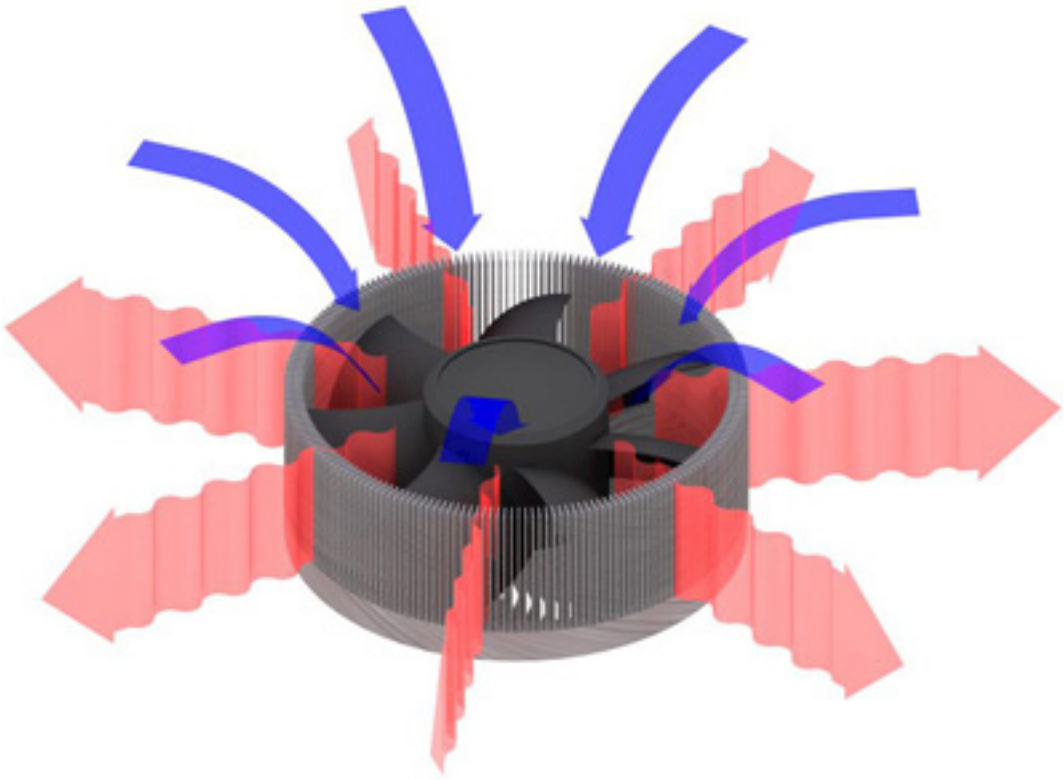

Figure 20. Active heat sink with attached fan [30].

The aforementioned types of heat sinks are typically fabricated in several different ways. Principal amongst these are stamping, extrusion, and casting [26]. Szumera et al. categorize metal stamping into five different methods: 1) swaging or coining, 2) bend forming, 3) draw forming, 4) deep draw forming and 5) blanking [31]. Swaging, also referred to as forging (hot or cold), is essentially the compression of a material into a given shape. This production method is ideal for powder metallurgy alloys with residual porosity, as hot forging can cause the collapse of pores and a subsequent increases in density while producing the desired near-net shape [32]. Bend forming, as the name suggests, is the bending of a flat metal plate into the desired geometry, without altering the starting thickness of the material. Bend forming is a common method for creating fins, which can be later bonded or attached to a heat sink base (either extruded or cast). Draw forming and deep draw forming are similar to extrusion and blanking is akin to machining (removing material), and thus do not warrant further discussion. Certain stamped heat sinks may require secondary processing to achieve a final geometry with fins. The success of stamping operations is highly dependent on material properties. In

order to cold form a material, it must have a high level of ductility so to avoid cracking. Even in highly ductile materials, depending on the amount of deformation, it is not uncommon to have multiple stages with subsequent annealing operations in between. An example of a stamped heat sink is shown in Figure 21.

Figure 21. Stamped aluminum heat sink [33].

Extrusion is similar to forging in that it is the plastic deformation of a material to reduce its area. Extrusion works by forcing a billet of metal through a die with a reduced cross-sectional area (Figure 22). Contrary to stamping, extrusion is a continuous process by which successive operations (machining, bonding or skiving) are often employed. Extrusion can be classified in two general categories: direct and indirect [34]. Figure 22 shows an example of direct extrusion where the extrusion direction is the same as the applied force from the ram. The result is a high frictional force between the die and the billet, requiring in turn, a higher pressure from the ram.

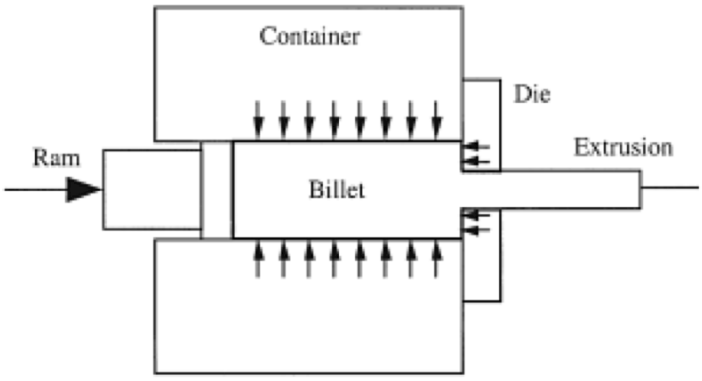

Figure 22. Schematic of an extrusion operation [34].

Indirect extrusion (Figure 23) reduces the contact area for countering frictional forces to occur between the billet and the container, effectively reducing the required load as seen in Figure 24. The three stages shown represent the stages of extrusion: I) the billet reaches a local peak stress as it is forced against the die, II) the force required for 'steady-state extrusion' is overcome and as the material begins to flow, stress is relieved, and III) there is a sharp rise caused by the end of the billet as it is pushed through the die [34].

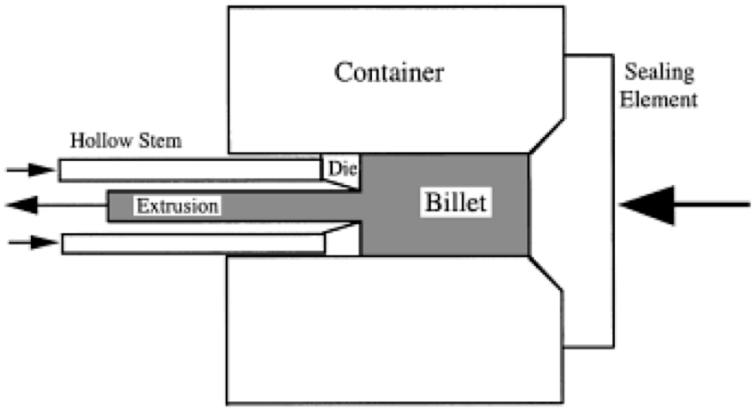

Figure 23. Schematic showing indirect extrusion [34].

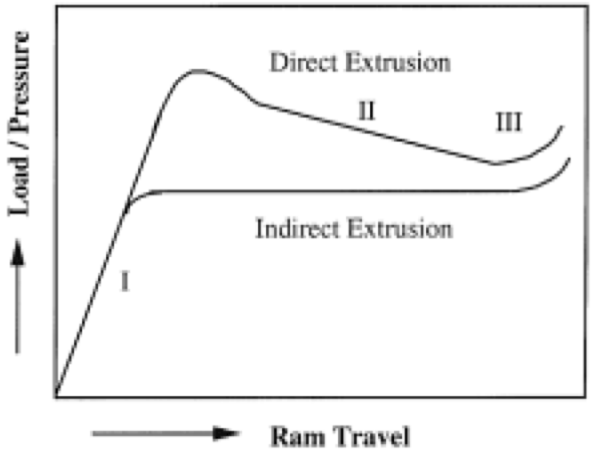

Figure 24. Pressure requirements for both direct and indirect extrusion [34].

In terms of adopting this common processing technique to heat sink applications, secondary operations are usually required. One method is using the extruded section as a simple rectangular base and having fins bonded directly to it through soldering or adhesives. This operation can be costly and there is often a difference in thermal conductivity at the point of adhesion [35]. Another factor to consider is that of varying CTE between the extruded base and the adhesive material (see Section 1.3.2.). Heat sinks can also be machined directly from a simple block of extruded material. However, this is an expensive method of fabrication that invariably generates a significant amount of scrap material.

Casting of metal can be accomplished through several means categorized by the type of mould used to shape the final part. The most popular techniques used for light metals such as aluminum, magnesium and zinc are sand casting, permanent mould casting, and die-casting [36]. Sand casting is a slow batch process wherein the mould is destroyed in order to eject the part. It provides the lowest level of dimensional control and requires post-production machining, thus increasing cost and overall production time. Furthermore, since casting sand has relatively low thermal conductivity, the molten metal takes longer to cool resulting in coarser grains with less finely dispersed strengthening mechanisms. While this has a negative impact on mechanical properties and production time, there is a trade off in that the thermal properties are generally higher in the slow-cooled, annealed state. A typical sand casting mould is shown in Figure 25. The molten

metal is poured through the pouring basin into the main sprue (gating system) at the slowest rate possible to ensure minimal porosity caused by trapped gasses. Risers allow for new liquid metal to be added to slow-cooling, high volume sections, which contract upon solidification [36]. Venting allows for excess air to escape and further reduces residual porosity.

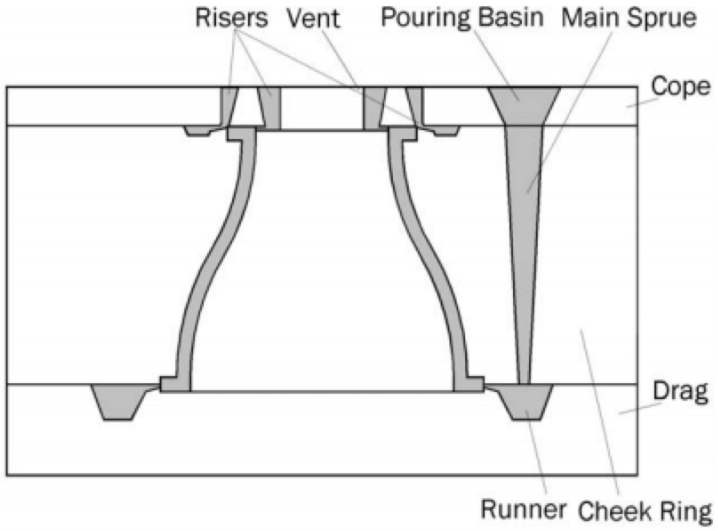

Figure 25. Schematic of a sand casting mould [36].

Permanent moulds (including dies) are more suited for large-scale, high volume production since moulds are reusable and yield inherently better dimensional tolerances and better surface finish. Permanent moulds are generally made from fine-grained cast iron [37] and consist of two halves tightly sealed together in the place of sand. The overall design is essentially the same as shown in Figure 25. This type of mould is either gravity fed or uses low pressure to inject molten metal. Increasing the feed pressure allows for better quality parts in terms of strength, surface finish, lower porosity and process automation. This is turn increases the consistency of parts by controlling the inlet velocity and flow rate [36].

Die-casting is a form of permanent mould casting, with closed dies and generally higher inlet pressure. By excluding the use of risers, less material is wasted and machining is minimized [37]. Dies are often water cooled in order to increase the rate of solidification. In die-casting aluminum, it is desirable to minimize the contact between molten

aluminum and steel since, thermodynamically, iron tends to diffuse into aluminum resulting in die degradation as well as lower quality alloys [37]. Figure 26 illustrates a cold chamber die-casting setup where the inlet feed tube is lined with a nickel alloy. The cool die allows for a high rate of solidification thus resulting in minimal contamination from the steel die. The elevated injection force along with a closed die results in high strength parts with elevated thermal conductivity (low porosity), high strength (less defects, elevated cooling rate) and good surface finish with the tighter dimensional tolerances than other casting methods [36]. Since these dies undergo high pressure and stress, they are generally fabricated from tool steels shown in Table 3, where select alloys are rated on a 1 – 10 basis (10 being the best). There is more emphasis on toughness and hot hardness since high levels of abrasion and impact are not encountered in production.

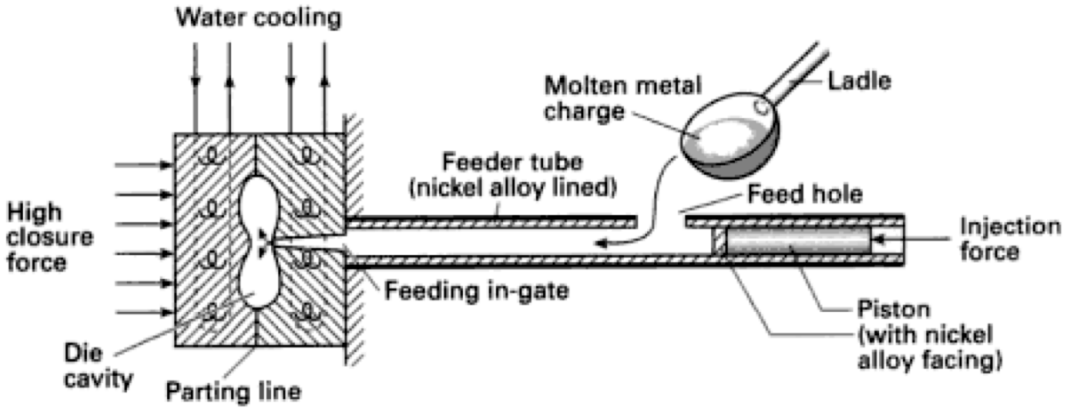

Figure 26. Cold chamber die-casting setup suitable for aluminum alloys [37].

Table 3. Tool steels for use in die-casting dies [38].

	Rating for:		
Steel	**Wear resistance**	**Toughness**	**Hot hardness**
P20	1	8	2
H11	3	9	6
H13	3	9	6
H12	3	9	6
H14	4	6	7
H21	4	6	8
H19	5	6	7
H23	5	5	8

1.3.2 Heat Sink Materials and Applications

Aluminum and copper are by far the most common heat sink materials, due to a combination of good thermal properties and affordability. The largest application of heat sinks is in the cooling of electronics [39-41]**.** In certain applications, where the heat sink is bonded directly to a silicon chip, there are issues with varying coefficients of thermal expansion (CTE) between the silicon and the heat sink (Al or Cu), as shown in Figure 27. The different CTE lead to differing levels of expansion upon heating and subsequent thermal stresses which can lead to failure [39].

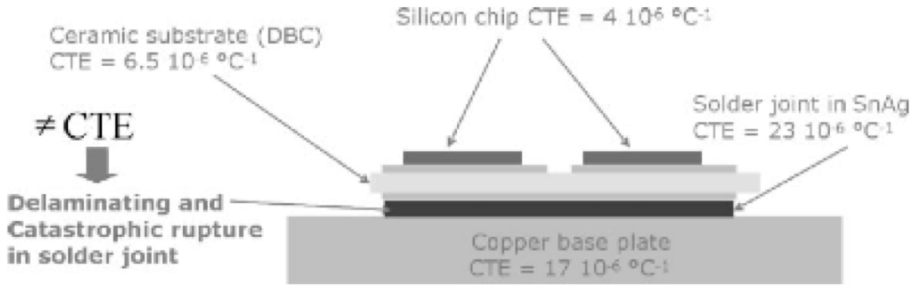

Figure 27. Typical microchip assembly [39].

For this reason, aluminum matrix composites with different CTE are being developed for certain heat sink applications using a PM approach. Additions of 60% SiC to aluminum results in a lower thermal conductivity (160 from 221 W/m-K) and higher density (2.94 from 2.70 g/cm^3), but lowers the CTE to better match that of the microchip [40]. In automotive applications, where weight is an important parameter, low alloy aluminum becomes a clear choice as copper has a density of 8.94 g/cm^3, which is over three times that of aluminum. A study by Tan, et al [41] comparing the thermal properties of a 'pure' aluminum PM material (aluMIM^{TM}) with that of a commercial aluminum 6061 alloy, which is common for general heat sink applications, showed better performance by aluMIM^{TM}, even with only 93% of the theoretical density of aluminum. The aluMIM^{TM} was produced through powder injection molding to the final shape, thereby facilitating a higher efficiency of material utilization. The AA6061 was extruded and then machined to have square pins. This extrusion operation also resulted in uniaxial grain elongation and subsequently, anisotropic thermal properties. Another common material in heat sinks is die cast A380 aluminum. In general, this alloy has relatively low thermal properties due

to the high concentrations of alloying elements. In particular, an appreciable concentration of silicon is added in order to effectively die cast the material. However, this element lowers the thermal conductivity by approximately 50% [7]. One benefit of using the A380 alloy is that fins can be cast directly, as opposed to machined, therefore cost and material loss is minimized.

A list of typical commercial aluminum heat sink materials and their thermal properties is displayed in Table 4. For the cast alloys, it can be seen that the 356.0 T51 alloy sand cast has the best thermal properties, likely due to the lack of copper, which has a high solubility in aluminum and readily forms intermetallic compounds. It is also important to note that this particular temper represents the lowest strength condition of the 356.0 series resulting in higher thermal properties. When comparing the sand cast vs. the permanent mould at the same T6 temper, the permanent mold is superior. The wrought alloys show better properties than the cast, as expected, with wrought 6063 having the highest thermal conductivity and diffusivity. Overall, the best thermal properties are typically realized in materials that have been annealed and recrystallized, due to the larger, strain-free grains and relatively low concentrations of finely dispersed precipitates.

Table 4. Thermal properties of commercial aluminum heat sink alloys at RT [42, 43].

Aluminum Alloy & Temper	K (W/m-K)	C_p (J/kg-K)	ρ (kg/m^3) x10^{-3}	α* (m^2/s) x10^5
Cast Alloys				
308.0 (Al-5.5Si-4.5Cu)				
As-cast	142	963	2.79	5.28
356.0 (Al-7Si-0.3Mg)				
T51, sand	167	963	2.685	6.46
T6, sand	151	963	2.685	5.84
T7, sand	155	963	2.685	5.99
T6, permanent mold	159	963	2.685	6.14
380.0 (Al-8.5Si-3.5Cu)				
As-cast	96.2	963	2.71	3.69
Wrought Alloys				
6061 (Al-1.0Mg-0.6Si-0.3Cu-0.20Cr)				
O	180	896	2.70	7.44
T4	154	896	2.70	6.36
T6	167	896	2.70	6.90
6063 (Al-0.7Mg-0.4Si)				
O	218	900	2.70	8.97
T1	193	900	2.70	7.94
T5	209	900	2.70	8.60
T6	200	900	2.70	8.23
PM Alloys				
aluMIM^{TM} (99.7% Al)	180	-	2.70	-

1.4 Aluminum Powder Metallurgy

1.4.1 Powder Compaction

In PM processing of materials, raw powder is compacted in order to increase density and strength, control porosity, and create a 'green' body with the desired dimensions of a final part [44]. There are several means of powder compaction used in PM processing, ranging from cold die compaction to powder rolling to hot/cold isostatic pressing [45-47]. Die compaction is the most common method employed. As it was also the only method used in the experimental section of this report it will be the only one discussed in detail. A typical uniaxial die compaction setup is shown in Figure 28. A single action press relies on a dynamic upper punch with a static lower punch. Double action presses compact the powder in two directions resulting in a reduced density gradient in the final product.

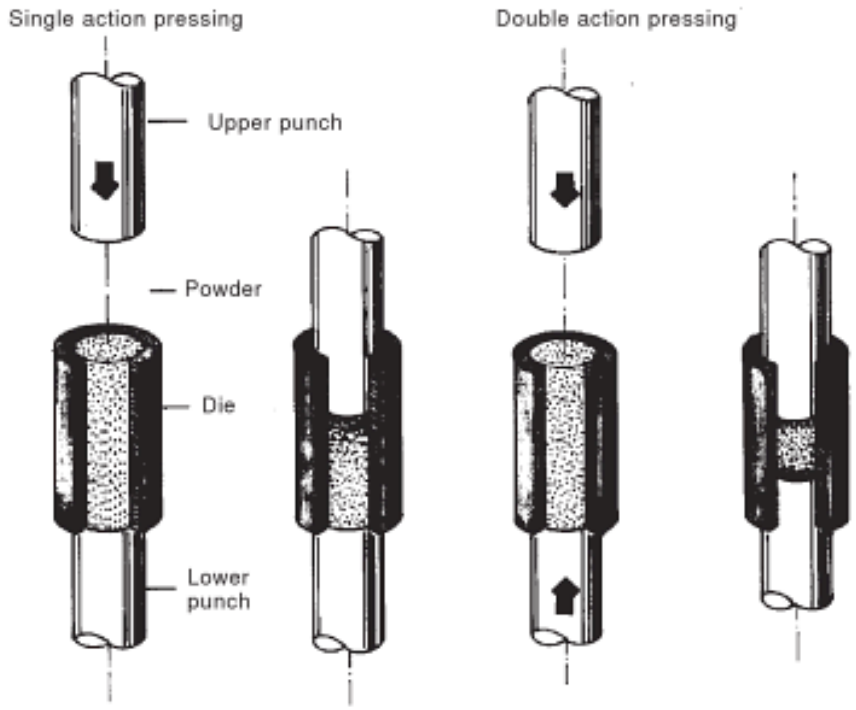

Figure 28. Uniaxial die compaction of metal powder [44].

During compaction, the powder undergoes various stages, beginning with the rearrangement of powder particles to fill in voids. The degree of densification obtained in this stage is largely based on the powder particle size distribution and morphology since there is no real particle deformation [48]. This packing density can be optimized through polyfraction mixtures, which is essentially varying the ratio of coarse and fine particles. This ratio is dependent on material and morphology as well and therefore must be found experimentally for a given material or mixture [49]. The next stage has to do with the elastic and plastic deformation of particles and is mainly dependent on the physical properties (compressibility) of the powders involved, such as strength, toughness and purity [50]. Throughout the compaction process, the powder is being work hardened and in the final stage, the only densification comes from cold working this powder and becomes a case of diminishing return, as can be seen in Figure 29.

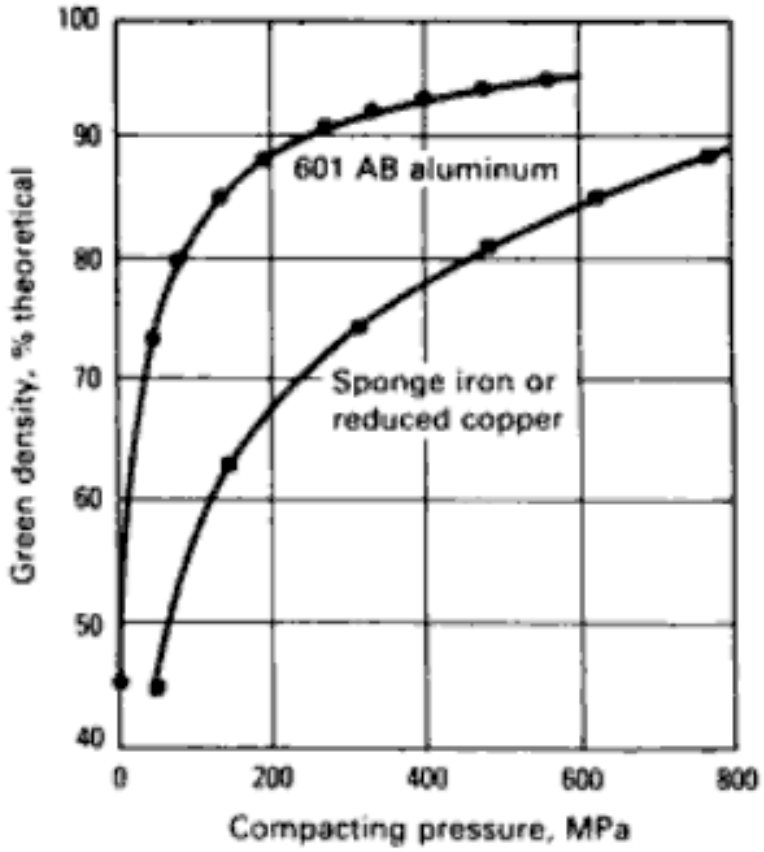

Figure 29. Compaction curve for several PM alloys [51].

The issue of die wall friction is a critical factor in uniaxial die compaction. This frictional force between the powder and the inner walls of the die inhibits the downward application of pressure and leads to density gradients within the 'green' compact [52] that can cause part distortion during sintering. Therefore, lubrication is either added to the die walls, admixed with the part, or both, in order to reduce friction [53]. Industrial admixed lubricants are generally made from metallic stearates or synthetic materials created for specific applications. Admixed lubricants generally lead to lower green strength as they inhibit the ability of the metallic particles to cold weld during the compaction process. In the compaction of aluminum, it is also important to choose a lubricant that vaporizes at a low temperature since the sintering temperature is generally on the order of ~600°C [54].

1.4.2 Liquid Phase Sintering

After the powder compaction stage comes sintering. Sintering is essentially heating the green compact to elevated temperatures for the purpose of creating interparticle fusion through the thermally induced movement of atoms. Sintering, by nature is performed at a temperature below the liquidus of the material (generally above half of the absolute melting temperature) [55], so that the green compact retains the original shape. Since diffusion rates increase with increasing temperature and are much higher within a liquid than a solid [56], it is desirable to sinter at the highest temperature possible and somehow incorporate the use of liquids. This is the rationale behind using liquid phase sintering (LPS) as a technique. LPS can be employed with a wide range of materials such as those of high (e.g. cemented carbides [57]) and low (e.g. aluminum alloys [58]) melting points. In order for LPS to work satisfactorily, several criteria must be satisfied. Namely that i) the element(s) responsible for the liquid phase must either have a low melting temperature (relative so the solid phase) or react with the base metal to form low melting point phases, eutectics, etc., ii) there should be high solubility of the solid in the liquid, iii) there should be low solubility of the liquid in the solid, and iv) the liquid phase must readily wet the solid particles [59]. Figure 30 shows the difference between a wetting, and non-wetting liquid. Important to note is that wetting liquids attract neighboring particles through capillary action whereas non-wetting liquids repel them.

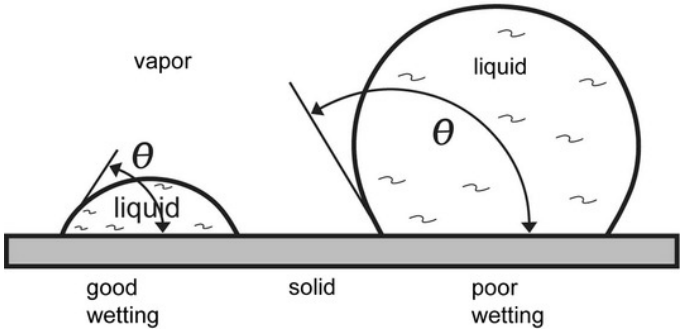

Figure 30. Contrast between wetting and non-wetting liquids based on contact angle [60].

There are several ways to introduce a liquid phase into the system. The most common is through simply admixing a low melting point constituent directly with the base powder. This additive powder should follow the characteristics listed above and therefore melt to directly create a liquid phase, of either a transient or preferably, persistent character [61].

Several sources [61-63] describe classic LPS as five overlapping stages that sequentially include the initial state of blended powders, solid state sintering, rearrangement, solution-reprecipitation, and final densification (Figure 31). As the powder blend is heated, liquid begins to form once the additive begins to melt. Solid state sintering initially occurs between contacting particles by diffusion. The rearrangement stage consists of the liquid being forcibly drawn between particles through capillary action. This results in a burst of densification due to the elimination of an appreciable fraction of internal pores. In the third stage, there is a significant amount of grain coarsening due to the variation in particle size. Smaller grains have a higher tendency to dissolve in the liquid, creating a concentration gradient within the surrounding liquid. This leads to the growth of larger grains at the expense of smaller ones, or Ostwald ripening. Eventually, the large grains begin to change shape in order to pack together more tightly. The net effect is the continued elimination of pores and an increase in density through the process of grain shape accommodation. The final stage of LPS results in slow densification due to the fact that the microstructure consists of large tightly packed solid grains with limited mobility. Therefore, any additional gains in densification can be attributed, again, to solid-state diffusion. This final stage should be kept short as a prolonged dwell within this stage can lead to a decrease in density.

One attribute that is both critical and unique to the LPS of aluminum alloys is the refractory oxide film that invariably exists on the surface of aluminum-based powder [64-66]. This stable refractory oxide layer has a high melting point and thereby impedes solid-state diffusion between contacting aluminum particles at the sinter temperature of interest (~600°C) [66]. However, since magnesium has an even higher affinity for oxygen, it has been proposed to act as a reducing agent. It is inferred that oxide reduction likely occurs through the following reaction:

$$3Mg + 4Al_2O_3 \leftrightarrow 3MgAl_2O_4 + 2Al$$

where $MgAl_2O_3$ is a spinel phase [66]. This reaction exposes the underlying metallic aluminum, thereby yielding free surfaces that exhibit good wettability, while promoting Al-Al inter-particle diffusion.

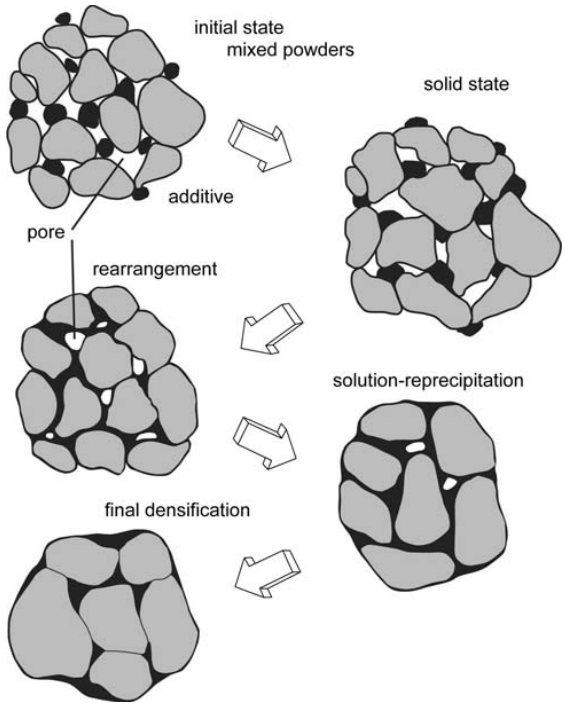

Figure 31. The five stages of classical LPS [60].

1.4.3 Effect of Alloying Elements

Alloying elements are almost always added to aluminum when creating sintered powder components in order to increase sintering response while enhancing mechanical properties. As mentioned above, pure aluminum has a higher thermal conductivity than any aluminum alloy but it cannot be sintered effectively through conventional means. This is due to the thermodynamically stable, refractory oxide/hydroxide layer found to coat aluminum powder particles [64-66]. When producing aluminum alloys through a PM approach for heat sink applications it is necessary to closely analyze the sintering response since high levels of porosity are so detrimental to the thermal properties [7]. Among the many alloying elements commonly added to aluminum (Cu, Zn, Si, Ni, Fe, Mg and Sn), Mg and Sn are perhaps the most prolific in terms of impacting the sintering response.

To illustrate the stability of the oxidized aluminum powder, thermodynamic analyses dictate that either the partial oxygen pressure must be lower than 10^{-50} atm [67] or the dew point must be below -140°C [68] in order to spontaneously reduce the aluminum oxide if sintering at 600°C. Magnesium, as an alloying addition was found to greatly

increase density in a pressed and sintered aluminum PM alloy [69] (Figure 32). This is attributed to magnesium disrupting the oxidation of aluminum by the creation of a spinel phase ($MgAl_2O_4$) resulting from solid-state diffusion.

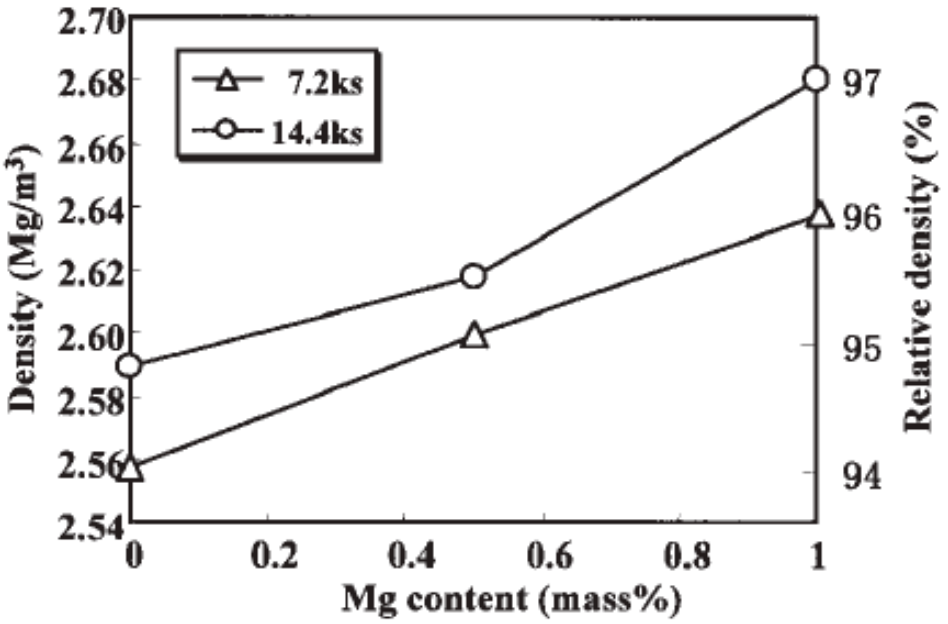

Figure 32. Effect of magnesium on the sintered density of aluminum, with varying sintering times [69].

When sintering aluminum in a nitrogen atmosphere, higher concentrations of magnesium allow for aluminum, now reduced, to react with nitrogen to form aluminum nitride [65]. Aluminum nitride has average thermal properties (~140 – 180 W/m-K) [70, 71]; however it is brittle and impedes densification. From the aluminum-magnesium binary phase diagram (Figure 33), it is evident that there is very little solid solubility of magnesium in aluminum and no liquid phase is expected to form while sintering at 630°C with low concentrations of Mg (<2.0 weight%). Small amounts of the intermetallic phase, Al_3Mg_2, are expected to form, which in turn should decrease the thermal properties of the alloy.

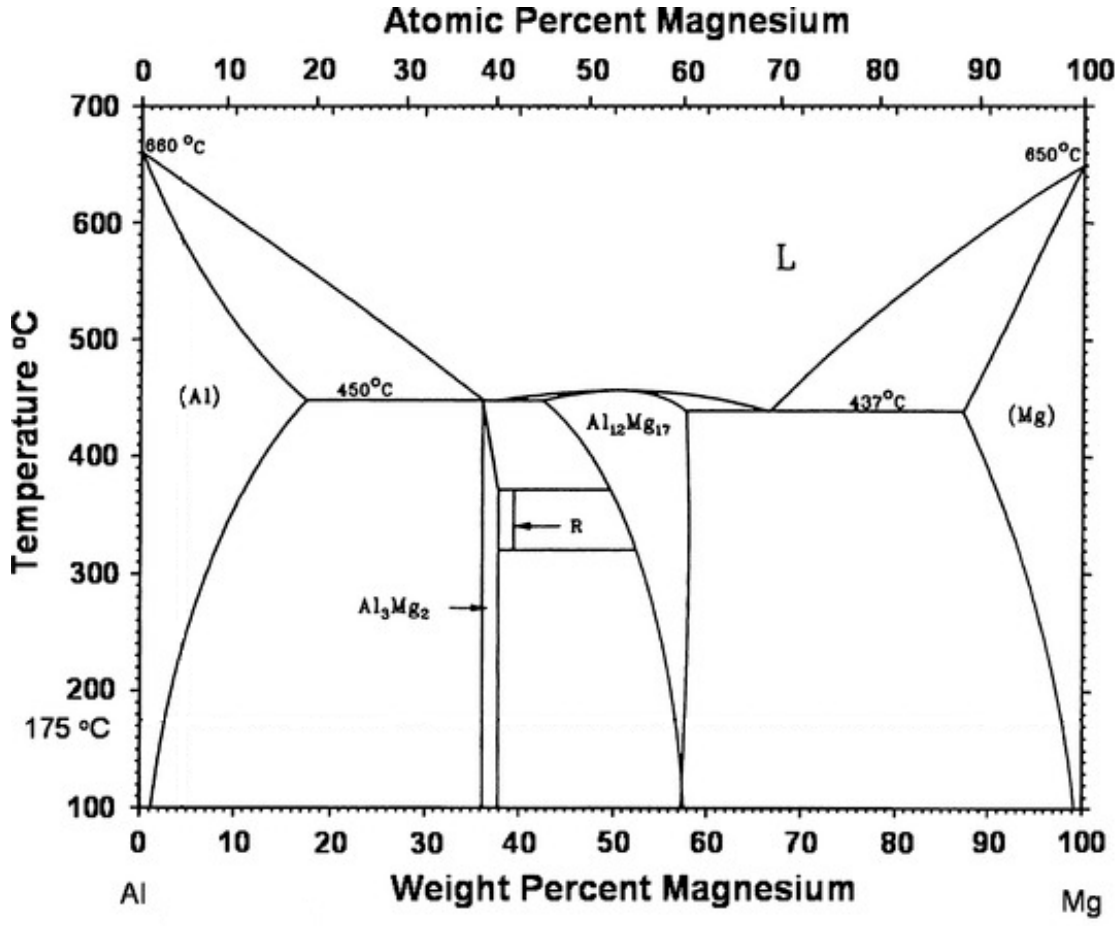

Figure 33. Al-Mg binary phase diagram [72].

Another element suitable to alloy with aluminum is tin [65, 73, 74]. The aluminum-tin phase diagram (Figure 34) indicates that tin is an excellent constituent to facilitate LPS, as this system matches the aforementioned solubility criterion, critical to LPS. In this sense, tin has a maximum solid solubility of ~0.15% in aluminum, whereas aluminum is 100% soluble in liquid tin. Tin also melts at a much lower temperature than aluminum (232°C for tin vs. 660°C for aluminum) yet it does not react with aluminum to form intermetallic aluminides.

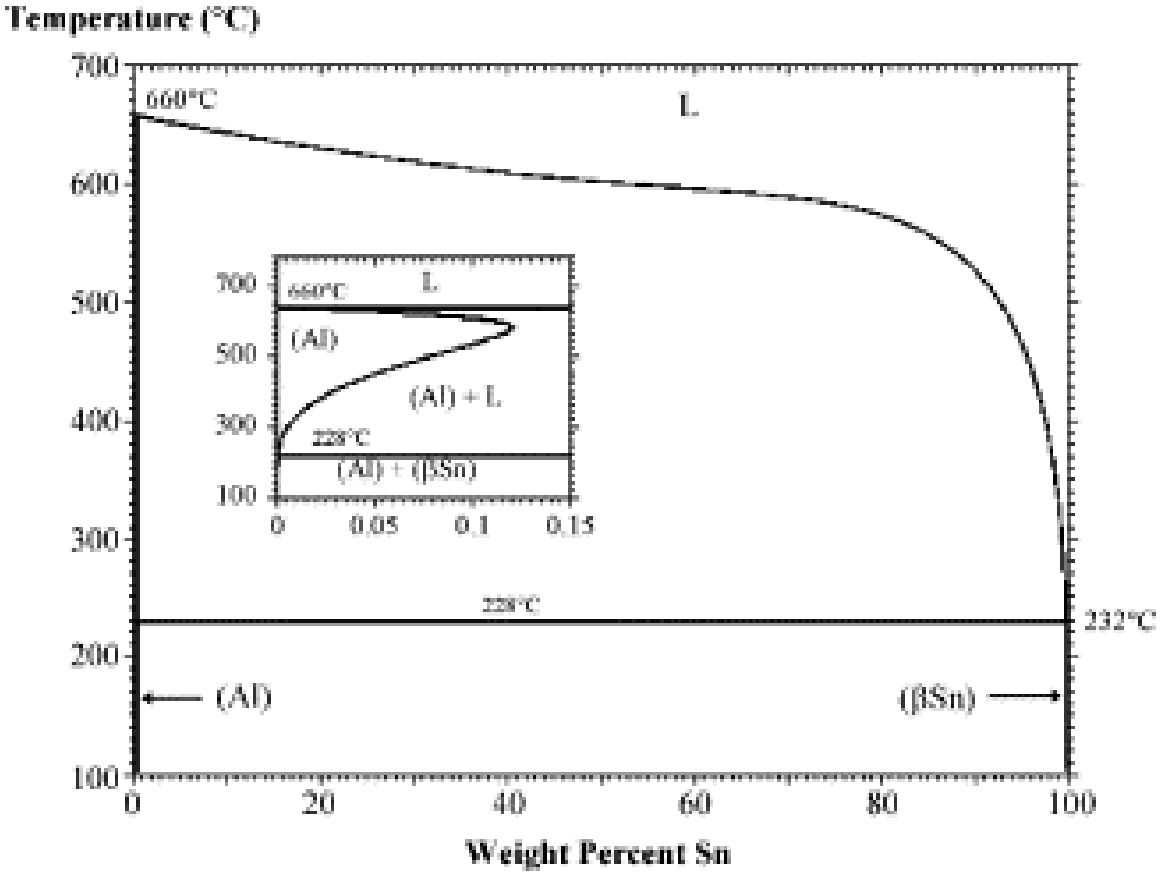

Figure 34. Al-Sn binary phase diagram [75].

Lumley et al. performed a study on the effects of magnesium and tin on the sintering of aluminum (Figure 35). They found that tin was not able to wet the surface of the oxidized aluminum particles and was therefore secreted from the material. By adding a small amount of magnesium (Figure 35b, c), the contact angle of the liquid tin was drastically decreased by exposing pure aluminum [66]. Another important characteristic of tin has been previously observed in the sintering of Al-Mg alloys. Sercombe et al. report a decrease in the amount of Al-Al bonding with an increase in tin, despite an increase in overall densification [76]. This was attributed to the fact that tin effectively creates an interface along grain boundaries and halts the solid-state diffusion between aluminum particles. This has a negative impact on the overall strength of the alloy [76] and should too, theoretically, have a negative impact on the thermal properties by disrupting/reducing the mean free path through the α-aluminum. Where magnesium promotes the formation of aluminum nitride when sintering under flowing nitrogen, tin minimizes it by wetting the aluminum surface and creating an interface for the nitrogen

gas. For this reason, tin has been found to be beneficial, in small concentrations (i.e. 0.1 weight%), to the densification of certain Al-Cu-Mg-Si alloys in nitrogen atmospheres [77].

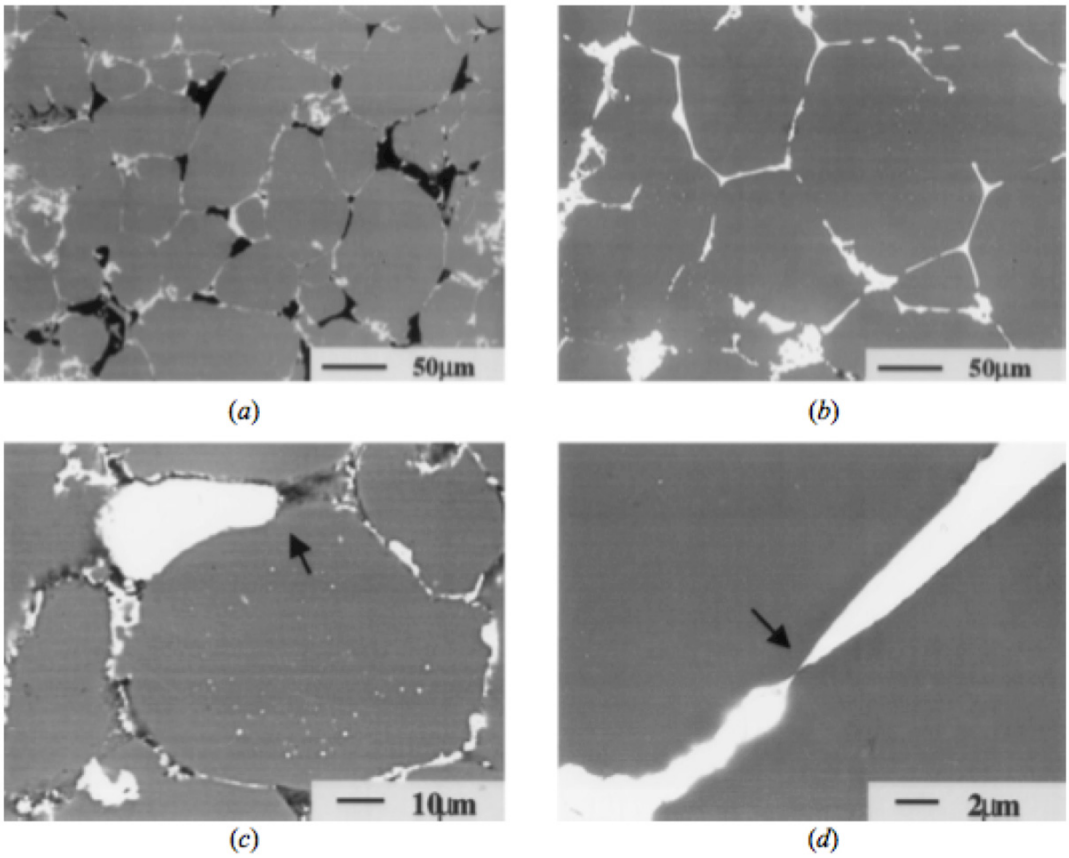

Figure 35. SEM backscatter images of aluminum PM alloys: (a, c) Al-8Sn and (b, d) Al-8Sn-0.15Mg. Tin is the white phase, aluminum is shown in grey and the black regions are pores [66].

So, it is not sufficient to alloy with magnesium alone as it promotes the formation of excessive amounts of aluminum nitride. Furthermore, alloying with a singular addition of tin is also ineffective as the liquid phase cannot breakdown the stable oxide film and it does not effectively wet the aluminum oxide layer. However, alloying with both tin and magnesium causes significant gains in densification. Furthermore, MacAskill et al. demonstrate that Al-Mg-Sn alloys exhibited a far superior sintering response when the magnesium was admixed as an elemental powder as opposed to using an Al-Mg master alloy (Figure 36) [65].

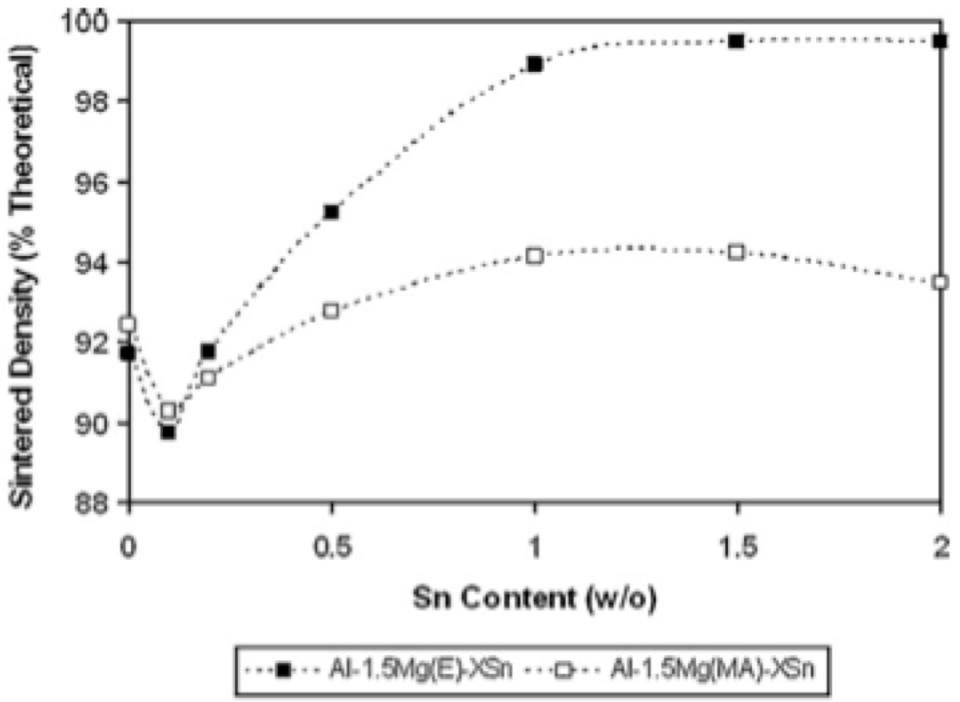

Figure 36. Sintered density of Al-Mg-Sn ternary alloys using both elemental (E) and master alloy (MA) magnesium sources [65].

According to the Mg-Sn binary phase diagram shown in Figure 37, magnesium and tin form a single intermetallic compound (Mg_2Sn) [78]. Furthermore, the Al-Mg-Sn ternary phase diagram reports no further intermetallic formulations between the three elements [79]. It is difficult to predict the interaction between magnesium and tin in PM systems due to the fact that magnesium, when in contact with aluminum will go into solid solution, but when in contact with tin, it will form an intermetallic. Since there is no way of telling how much magnesium is actually in physical contact with tin, it is difficult to predict the amount of interaction between the two elements.

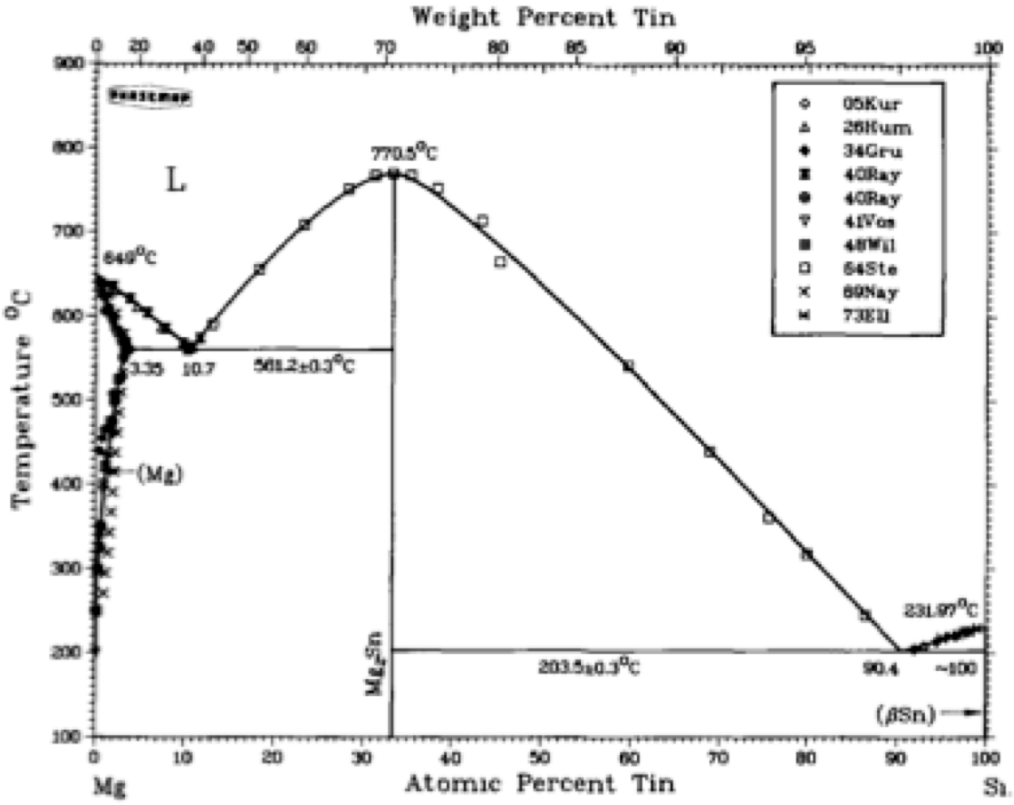

Figure 37. Magnesium-tin binary phase diagram [78].

1.4.4 Typical Alloys and Properties

There are several commercial aluminum PM alloys in production today, along with many others in development. Several popular alloys and their chemistries are listed in Table 5.

Table 5. Nominal chemistries of various aluminum PM alloys.

Concentration of Alloying Elements (weight%)	**Alumix 123**	**Alumix 231**	**Alumix 431D**
Cu	4.4	2.5	1.6
Mg	0.5	0.5	2.5
Si	0.6	15	-
Zn	-	-	5.5
Sn	-	-	0.2
Al	Bal.	Bal.	Bal.

Alumix 123 is an alloy comparable with 2xxx series wrought aluminum alloys due to the high copper content and is used widely in automotive applications. This alloy

incorporates the use of liquid phase sintering through the liquid formed between the Al-Al_2Cu eutectic [80]. Work has been done to incorporate a second liquid phase (between Al and Si) to Alumix 123 through small additions of Al-12Si (Figure 38) [80]. Incorporation of this second liquid phase was found to increase the sintered density, likely due to the segregation of the Al-Al_2Cu liquid phase to the surface of the Al-Si liquid, which, in turn, creates an interface to disrupt the diffusion of copper into the aluminum [80]. Alumix 123 is heat treatable and age hardening can occur through the dispersion of metastable variants of the Al_2Cu intermetallic phase. When heat-treated to the peak strength (T6) temper, Alumix 123 can reportedly achieve an ultimate tensile strength (UTS) of 320MPa, a yield strength of 300MPa, with 1% elongation [81].

Alumix 231 is the first commercial PM Al-Si alloy. This is due to the fact that high concentrations of silicon lead to poor compressibility and subsequently, difficulties in processing from a PM approach. For this reason, there is limited information available about its properties. A study was performed by Heard, et al [82] as to the optimal sintering temperature and associated tensile properties, as shown below in Figure 39. There is a sizeable increase in the mechanical properties with increased sintering temperature due mainly to the increased concentration of the Al-Si liquid phase. This is reiterated by a microstructural assessment (Figure 40) showing an under sintered product in Figure 40 (a) consisting of a high concentration of pores (black) with silicon (grey) still present within the master alloy particles. The optimal sintering temperature shown in Figure 40 (b) shows a good dispersion of the silicon phase, low porosity and uniform grain size. In the over sintered condition (Figure 40 (c)), there is conglomeration of the silicon phase, along with grain growth and a high degree of residual porosity [82]. This alloy typically exhibits high wear resistance due to the dispersed silicon phase. This further reinforces the importance of the liquid phase in the sintering of aluminum PM parts, regardless of the principal alloying elements.

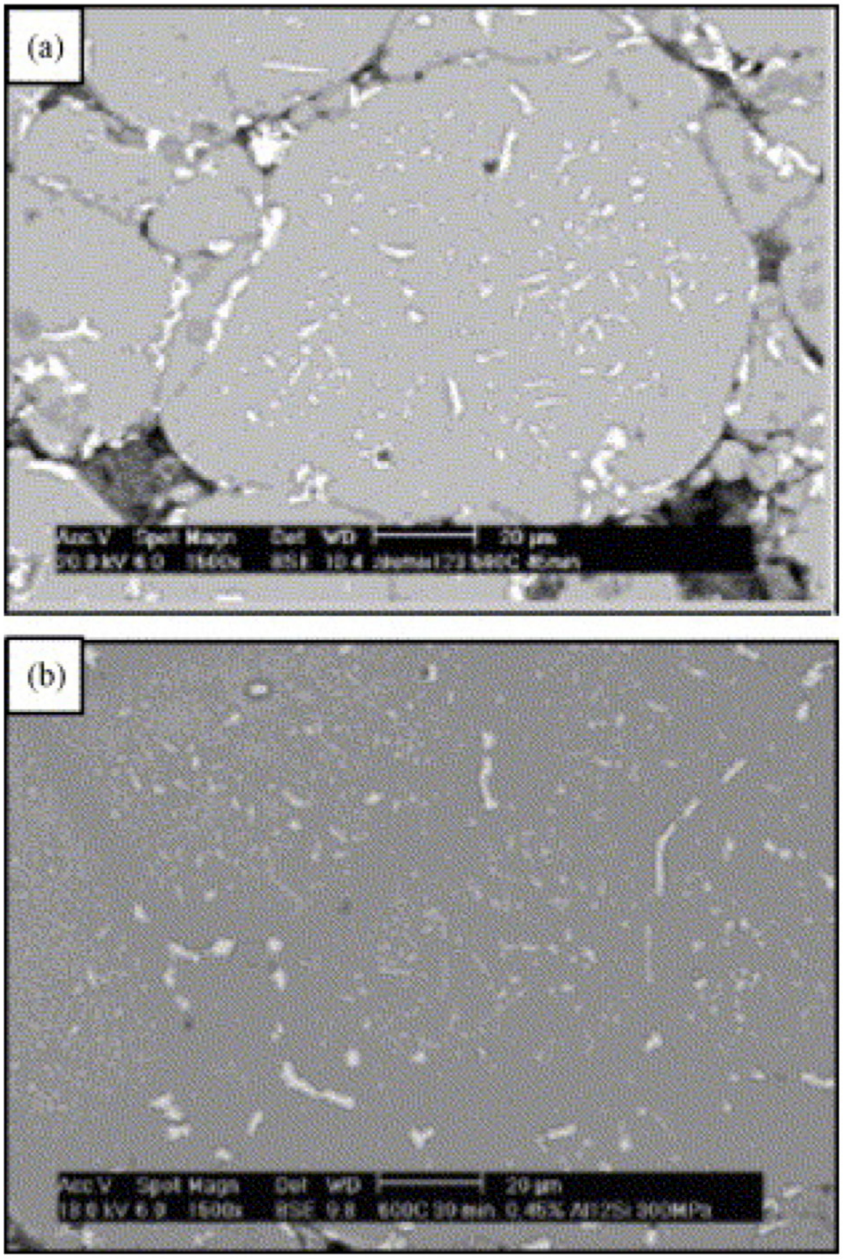

Figure 38. Sintered microstructures of (a) Alumix 123 and (b) Alumix 123 + 0.45 weight% Al-12Si [80].

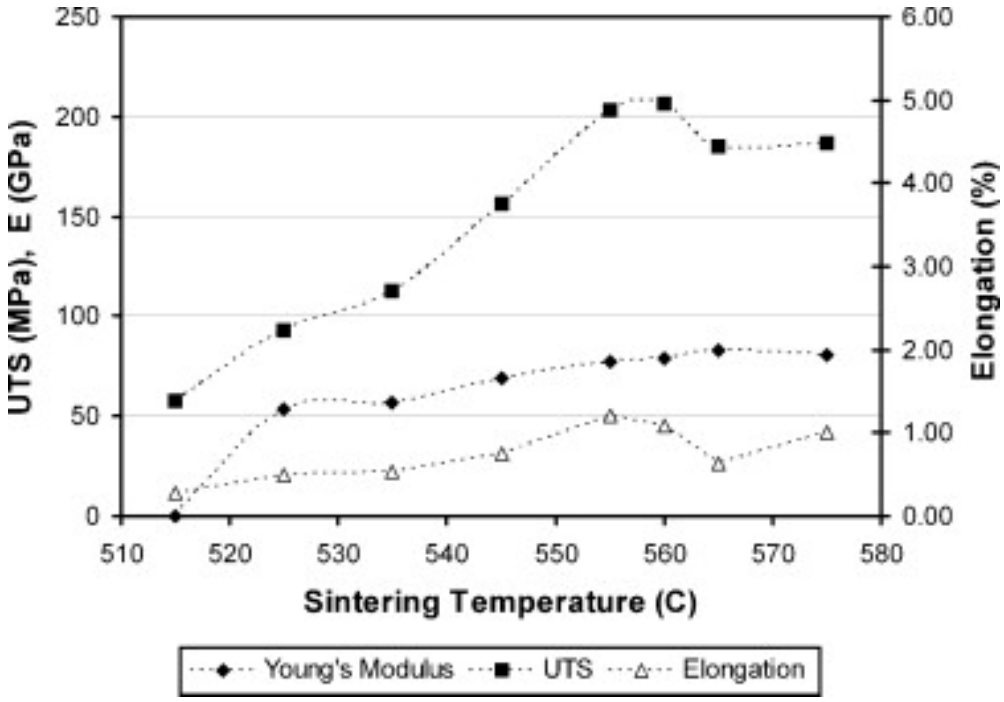

Figure 39. Tensile properties of Alumix 231 compacted at 600 MPa [82].

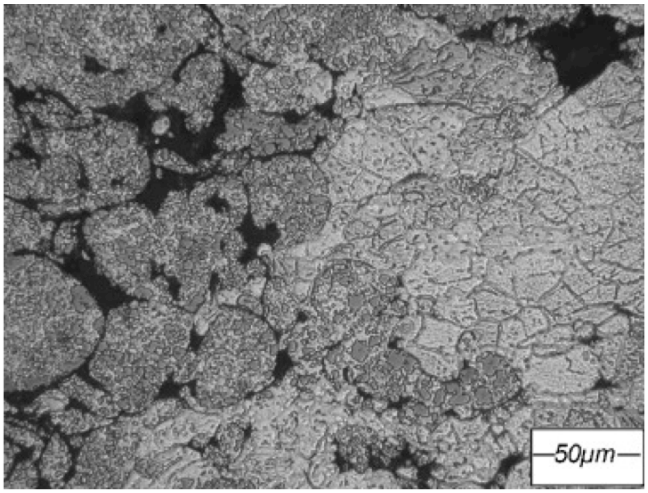

(a)

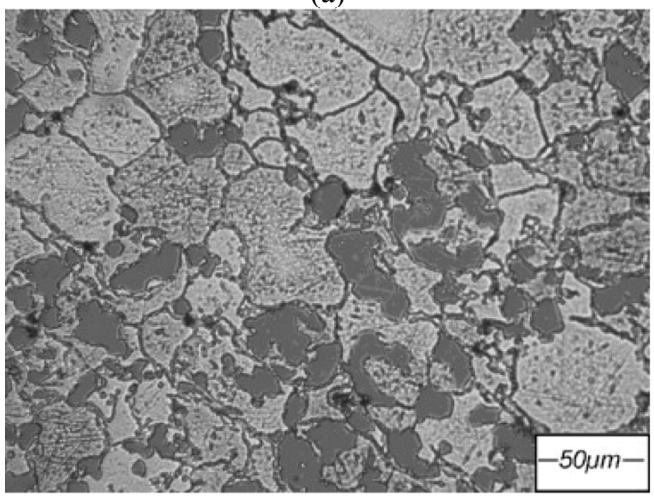

(b)

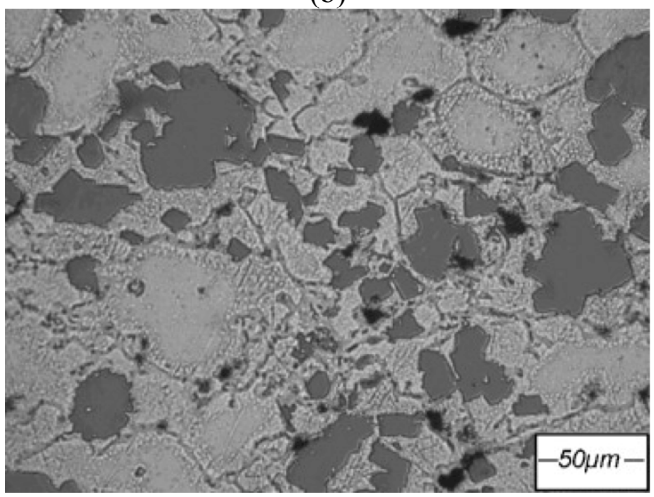

(c)

Figure 40. Sintered microstructures of Alumix 231 sintered at (a) 515 (b) 560 and (c) 575°C [82].

Another commercially available PM alloy is Alumix 431D, which is comparable to a 7xxx series wrought alloy (Table 6), given the relatively high concentrations of zinc and magnesium. This type of alloy exhibits a relatively high strength to weight ratio, which is attributed to strong densification during sintering and direct strengthening through precipitation hardening [83]. Similar to Alumix 123, Alumix 431D relies on age hardening as the principal strengthening mechanism, using intermetallics of the η-type ($MgZn_2$) as opposed to those from the θ (Al_2Cu) sequence. Since these alloys reach peak strength in the GP zone stage of heat treatment, they are more sensitive to thermal exposure than Al-Cu alloys [83]. For this reason, they are more suitable for low temperature applications. Tin is also present in this alloy to aid in sintering, again, due to the formation of a liquid phase at relatively low temperatures (T_{melt} = 232°C). An EPMA micrograph of the sintered product is shown in Figure 41. There is a low concentration of rounded porosity, along with a dispersed secondary phase along grain boundaries [83].

Table 6. Tensile properties of Alumix 431D compared with wrought 7075 [83].

System	Yield strength (MPa)	UTS (MPa)	Elongation (%)	E (GPa)
Alumix 431D-T1	279 ± 4.7	323 ± 2.9	1.4 ± 0.1	66 ± 2
Alumix 431D-T6	444 ± 8.1	448 ± 11	0.9 ± 0.1	65 ± 2
Wrought 7075-T6	485	550	14	71

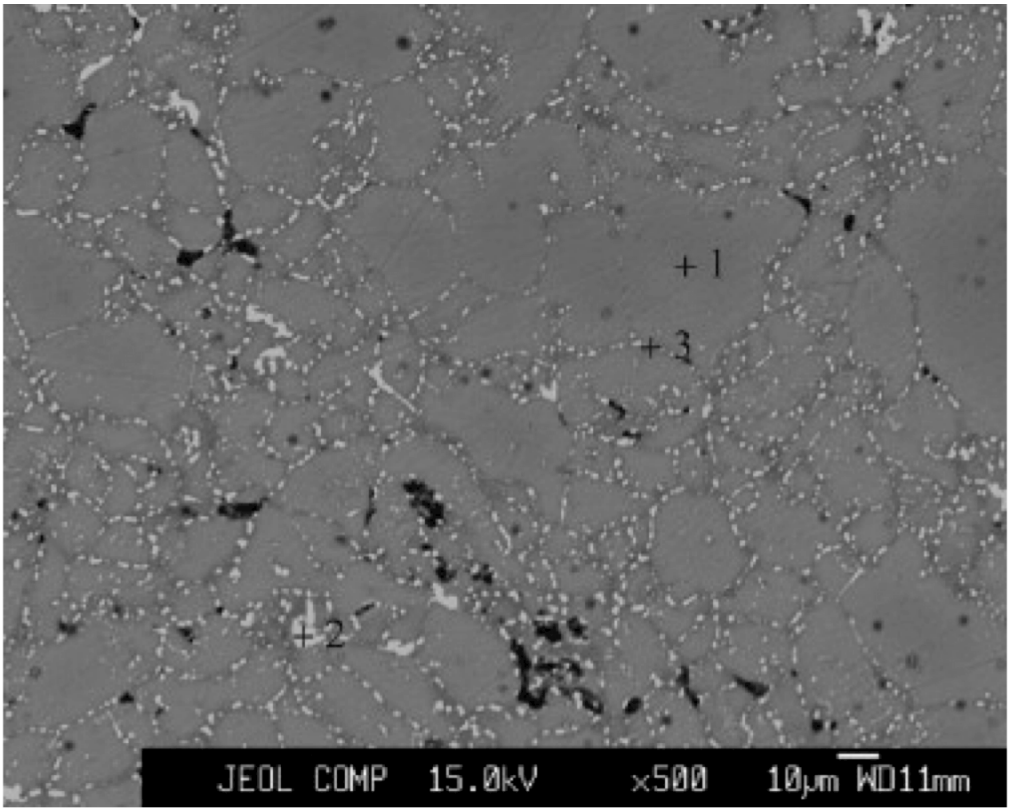

Figure 41. EPMA micrograph in compositional mode of Alumix 431D in the T1 condition (as-sintered) [83].

CHAPTER 2. RESEARCH OBJECTIVES

The main objective of this research was to delve into the untapped market of thermally conductive PM alloys. This is expected to be accomplished through minimizing alloying elements with precise control, taking advantage of liquid phase sintering to yield a highly dense sintered product, and developing processing strategies, which can be adapted to high volume production. Given a general knowledge of thermal properties, metallurgical factors leading to high levels of thermal conductivity, and the successful use of aluminum PM in mechanical applications, the ultimate goal was to produce a thermally conductive aluminum PM alloy competitive with wrought/cast counterparts.

CHAPTER 3. DEVELOPMENT AND PROCESSING OF NOVEL ALUMINUM POWDER METALLURGY MATERIALS FOR HEAT SINK APPLICATIONS

L.J.B. Smith[1], R.L. Hexemer Jr.[3], I.W. Donaldson[4] and D.P. Bishop[2]

1 – Graduate Student, Dalhousie University, Halifax, Nova Scotia, Canada
2 – Professor, Materials Engineering, Dalhousie University, Halifax, Nova Scotia, Canada
3 – Research Engineer, GKN Sinter Metals LLC, Conover, North Carolina, USA
4 – Director of R&D North America, GKN Sinter Metals LLC, Auburn Hills, Michigan, USA

Status: Submitted to *Metallurgical and Materials Transactions A,* May 2013

The following experimental procedures, results and discussions were completed by L.J.B Smith, with reviewer and editorial roles played by the subsequent authors.

Abstract

The objective of this research was to design aluminum powder metallurgy (PM) alloys and processing strategies that yielded sintered products with thermal properties that rivaled those of the cast and wrought aluminum alloys traditionally employed in heat sink manufacture. Research has emphasized PM alloys within the Al-Mg-Sn system. In one sub-theme of research the general processing response of each PM alloy was investigated through a combination of sintering trials, sintered density measurements, and microstructural assessments. In a second, the thermal properties of sintered products were studied. Thermal conductivity was first determined using a calculated approach through discrete measurements of specific heat capacity, thermal diffusivity and density and subsequently verified using a transient plane source technique on larger specimens. Experimental PM alloys achieved >99% theoretical density and exhibited thermal conductivity that ranged from 179 $Wm^{-1}K^{-1}$ to 225 $Wm^{-1}K^{-1}$. Thermal performance was largely dominated by the amount of magnesium present within the aluminum grains and in turn, bulk alloy chemistry. Data confirmed that the novel PM alloys were highly competitive with even the most advanced heat sink materials such as wrought 6063 and 6061 in terms of thermal properties.

Keywords: Aluminum Powder Metallurgy, Powder Compaction, Liquid Phase Sintering, Thermal Conductivity, Thermal Diffusivity, Heat Capacity, Heat Sink.

3.1. Introduction

Historically, the fabrication of heat sink devices has been accomplished through either casting or a wrought production approach [84-88]. Materials are generally selected by evaluating the thermal properties, formability, weight and of course cost. Pure metals, for example, are inherently superior conductors of heat due to their ability to facilitate electrical charge carriers throughout their crystal structure [1]. In the case of solids, excitations in the form of particles (charge carriers) or waves (phonons) are what give rise to thermal conduction [3]. Therefore, metals exhibiting good electrical conductivity are also able to generate high levels of heat transfer. There are several factors that influence the electrical properties and therefore thermal properties of metals, namely: multiple phases within the material, elements in solid solution, porosity and dislocation density [5]. In terms of malleability, pure metals can be easily formed into complex geometries through extrusion, which is often required for heat sinks. Machinability can also be a factor if the heat sink design is too complex for a mold or too brittle to be extruded.

Aluminum and copper are the most common heat sink materials due to a combination of good thermal properties and affordability. The largest application of heat sinks is in the cooling of electronics [39-41]. In automotive applications, however, aluminum is the clear choice as copper has a density over three times greater than that of aluminum. Common aluminum alloys used in heat sinks are cast aluminum 390 and wrought 6063, which have nominal thermal conductivity values of 134 and 200 W/m-K respectively [42, 43].

An emerging means of aluminum processing is powder metallurgy (PM) technology. Here, aluminum powder is blended with controlled alloying additions, compacted into a semi-dense ‘green’ body and then heated to sinter the particles into a coherent product [44]. This process allows for the production of components with an engineered geometry in a near-net-shape manner, promoting a high material utilization rate (>95%) with the need for little to no machining. It also allows for precise control over chemical additions, as well as a more homogeneous dispersion of precipitates and aggregates than can

typically be achieved when melting the constituents together [32]. This results in aluminum PM alloys that are highly competitive with comparable wrought alloys in terms of strength, fatigue and elevated temperature stability [9, 90]. As such, aluminum PM technology is now utilized in the manufacture of a growing list of automotive components in annual volumes that are on the order of $>10^6$ parts/year. Given the proven success of aluminum PM in scenarios that are dominated by mechanical property needs, it would seem logical that the near-net-shape advantages could also be leveraged in the manufacture of heat sink devices provided that adequate thermal properties could be realized. Hence, the objective of this research was to develop new aluminum-based PM materials with elevated thermal properties that would be competitive with those achieved in conventional of cast or wrought alloys.

3.2. Experimental Procedures

To fabricate the required samples, a press-and-sinter approach typical of high volume PM production was employed. Initially, assorted blends of aluminum, magnesium and tin powders, along with 1.5 weight% of a powdered lubricant (Licowax C™; Clariant Corporation) required for die compaction purposes were prepared using a Turbula model T2M mixer and a total mixing time of 30 minutes. Samples of the homogenized blends were then compacted using an Instron test frame at 200 MPa (model 5594-200HVL; 1 MN capacity) equipped with a floating die assembly. Two specimen geometries were produced – rectangular bars that measured 10 x 12.7 x 31.7 mm and cylinders with a 30 mm diameter and 10 mm overall length (OAL). Compacted specimens were then sintered in a laboratory scale tube furnace under an atmosphere of flowing, high purity nitrogen (99.999%). All samples were heated through a thermal profile that included a 20 minute hold at 400°C for de-lubrication purposes, a hold of 30 minutes at 630°C for sintering, and finally, gas quenching to ambient.

To evaluate the general response of each alloy to PM processing, data on sintered density, and microstructural observations were accumulated. Sintered density was measured using oil impregnation coupled with a standard Archimedes type of approach. Two samples

were measured in each instance with average values reported. Microstructural characterization included the use of electron probe micro-analysis (EPMA) and x-ray diffraction (XRD). EPMA studies were completed on samples that were mounted/polished using standard metallographic techniques, followed by carbon coating. Samples were then analyzed using a JEOL 8200 EPMA equipped with wavelength dispersive spectroscopy (WDS). The unit was operated in backscatter imaging mode at an accelerating voltage of 15 kV. For each specimen, the average of ten discrete measurements was used as a representative reading. XRD data were acquired with a Bruker D8 Advance operated with a tube voltage of 40 kV and tube current of 40 mA. The incident beam was Cu Kα radiation filtered with nickel foil.

Thermal property measurements included the use of a differential scanning calorimeter (DSC), laser flash analyzer (LFA), thermal dilatometer, and a transient plane source (TPS) thermal conductivity apparatus. For DSC testing, sintered bars were machined into cylinders (5.2 mm diameter x 1 mm OAL) and then cleaned with petroleum ether. Using a Netzsch DSC 404 F1, heat capacities (Cp) for each alloy were determined using the Ratio Method with a sapphire standard over a temperature range of 25 – 300°C in alumina-lined, platinum crucibles. DSC test parameters included a high purity (99.999%) argon atmosphere flowing at 50 mL/min, a heating rate of 20 K/min, and sample temperature control engaged. Each session consisted of two repeatable baselines (both crucibles empty) followed by a sapphire correction run, and finally a run on the sample of interest. Prior to testing, temperature and sensitivity calibrations were completed. There, small (~10 mg) samples of high purity In, Sn, Bi, Zn, Al, Ag, and Au were melted under the same conditions (atmosphere and heating rate) utilized when testing unknown PM samples. Next, the melting temperature and enthalpy of reaction were recorded and tabulated to create appropriate calibration files. LFA work was completed with a Netzsch model 472 laser flash apparatus. Flat, polished specimens with a nominal size of 10 x 10 x 4mm were prepared from each sintered alloy and coated with a thin layer of graphite to minimize reflectivity. Following two purge cycles with argon as the backfill gas, a temperature profile was set-up so that five shots were taken at temperatures of 50, 100, 150, 200 and 250°C with a two-minute delay between shots to allow for baseline re-

stabilization. During each test, a dynamic atmosphere of flowing argon (150 mL/min) was maintained, laser voltage was set at 360 V with a pulse width of 0.6 ms. The furnace was ramped at a rate of 5 K/min when heating to 50 and 100°C and then 10 K/min for the remainder of shots to compensate for the higher overshoot observed at lower temperatures. A minimum temperature stability of ±0.2 K/30 s was implemented to ensure an accurate temperature reading at the time of each reading. Afterwards, the Cowen + pulse correction model was applied using the Proteus LFA Analysis software to convert the half-rise time to a thermal diffusivity reading. Dilatometry testing was completed on machined cylinders (25 mm x 6 mm diameter) using a Netzsch model 402C pushrod dilatometer. All runs were conducted in air with a heating rate of 5 K/min from room temperature up to 350°C. Temperature calibration was accomplished by melting small specimens of high purity In, Sn, Bi, Zn, Al, and Ag sandwiched between two alumina disks. The melting temperature was recorded as the temperature at which the linear expansion showed an instantaneous drop. Displacement was calibrated by measuring the expansion of a single crystal of sapphire and comparing the results to known values. Finally, TPS tests were completed with a Thermtest model 1500 thermal conductivity system on 30 mm diameter cylindrical pucks to determine bulk material thermal conductivity. Each test was completed at 25°C using a pair of identical pucks with milled mating surfaces to ensure flush surface contact.

3.3. Materials

An assortment of aluminum PM alloys were produced for the purpose of this research. The reported chemistries of all such materials as well as the commercial materials tested for comparison purposes are expressed in weight% throughout the manuscript. All of the experimental PM alloys of interest were members of the Al-Mg-Sn ternary system. A total of 18 different alloys were assessed with magnesium and tin contents ranging from 0.4 to 2.0%. The balance was aluminum in all instances. All blends were formulated from elemental powders of aluminum, tin, and magnesium produced through atomization techniques. The morphology of each powder is shown in Figure 42. The aluminum powder particles were slightly rounded but mainly irregular with a measured average

particle size (D_{50}) of 116μm. The magnesium powder was made up of largely spherical particles with a smaller D_{50} of 32μm. The tin powder had the finest particle size with a D_{50} of 5μm. The morphology of the tin was largely spherical, matching that of the magnesium. For comparison purposes, samples of three commercial alloys were also tested in the research. One material was an industrially sintered slug of an aluminum alloy currently utilized in high volume PM processing – AC2014 [91, 92]. This particular alloy had a nominal chemistry of Al-4.5Cu-0.6Mg-0.8Si (weight%) and a sintered density of 2.52 g/cc (90.6% of theoretical). The second was die casting alloy 390 with a nominal chemistry of Al-17Si-4.5Cu-0.6Mg while the third commercial material was an extruded rod of wrought 6063-T1 (Al-0.7Mg-0.4Si).

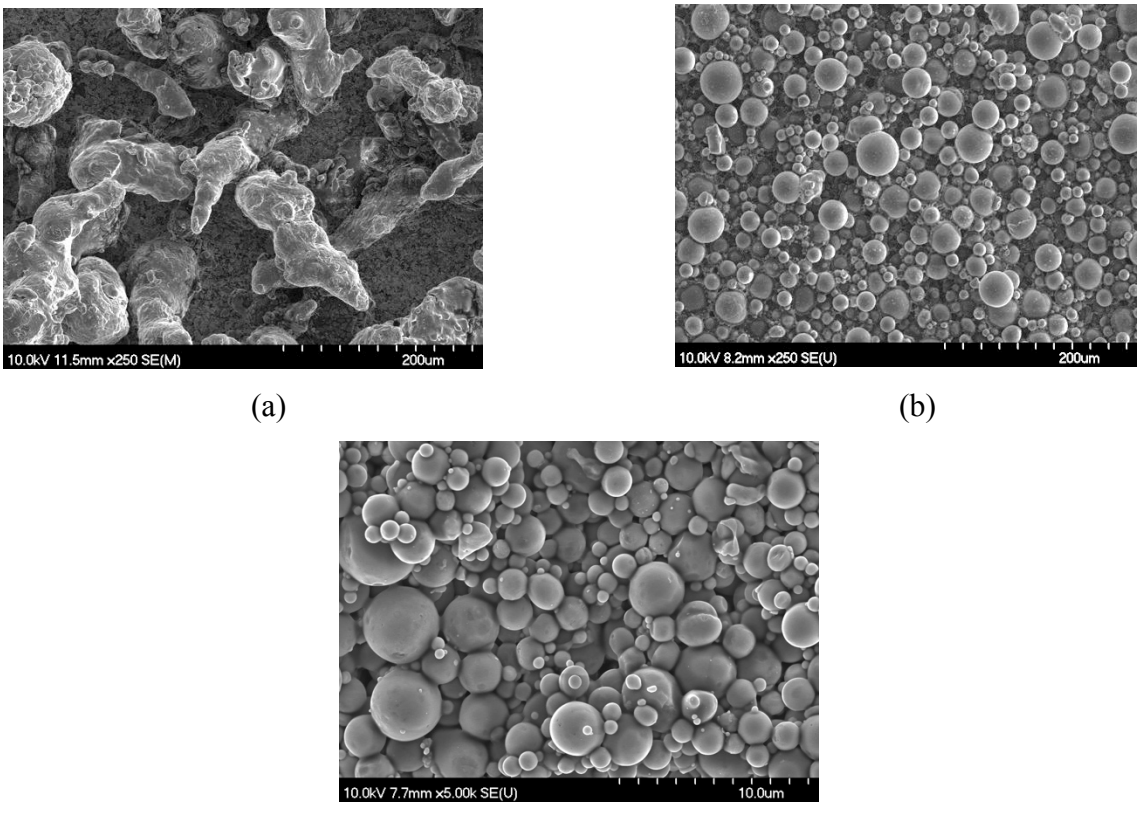

Figure 42. Images of the atomized metallic powders utilized to produce the PM alloys of interest. (a) Aluminum, (b) magnesium, and (c) tin.

3.4. Results & Discussion

In order to better understand the thermal properties of experimental PM alloys, it was first necessary to analyze the sintering response. More specifically, the density of each alloy was determined so that the effects of residual porosity on the thermal properties could be quantified. Next, the microstructure was studied using EPMA and XRD. Data on thermal conductivity (K) were then calculated using the expression $K = \alpha\, C_p\, \rho$ after separate evaluations of heat capacity (C_p), thermal diffusivity (α), and density (ρ). For comparison purposes, bulk measurements of K were also completed on select materials using a TPS unit.

3.4.1 PM Sintering Response

Sintered densities for the PM alloys studied are given in Figure 43. Measurements of this attribute for the alloys of varying tin content (Figure 43(a)) showed that final densities spanned from 96.5 to >99.7% of full theoretical. The only prolific drop in density occurred in the samples with tin concentrations ≤0.6%. All other density values lied within a relatively narrow range of 99.4 to 99.7%. These findings indicated that a minimum tin concentration of 0.8% was required to effectively densify the Al-1.5Mg-xSn series of PM alloys. The effects of magnesium on the sintered density of PM alloys with a constant tin content of 1.5%, were less dramatic (Figure 43(b)). Here, a steep decline in density was not observed in alloys with magnesium concentrations as low as 0.4% (unlike tin effects), as all ternary formulations reached a final density >99% of theoretical. The highest density measured was 99.7% and was achieved in samples with 1.8 and 2.0% magnesium. However, over the complete range of magnesium concentrations the trend of increasing densification with higher magnesium content was relatively subtle. It is common knowledge that atomized aluminum powders are covered in a thin film of aluminum oxide/hydroxide [64]. Furthermore, given the refractory nature of this film and its high thermodynamic stability, conventional sintering of aluminum powders is also known to be highly problematic [65]. To resolve this difficulty, powder blends typically contain magnesium, as this element reacts with the film to form spinel ($MgAl_2O_4$) so as to disrupt its continuous nature and thereby enable

sintering to proceed [65, 93]. Hence, it is postulated that the small gains in sintered density came as a result of a more progressively intense disruption of the oxide film. Overall, the majority of PM systems studied sintered to a comparable final density in excess of 99% of theoretical.

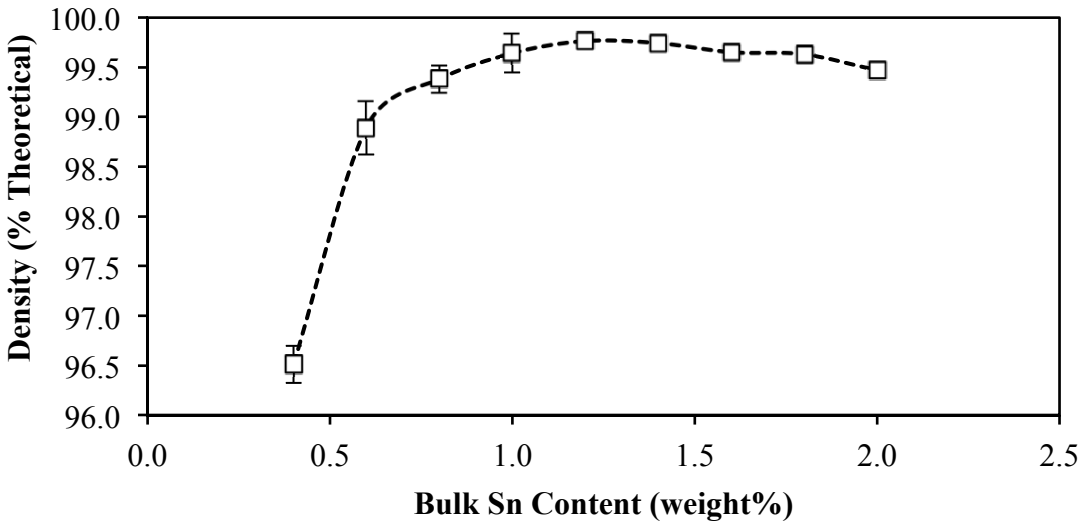

(a)

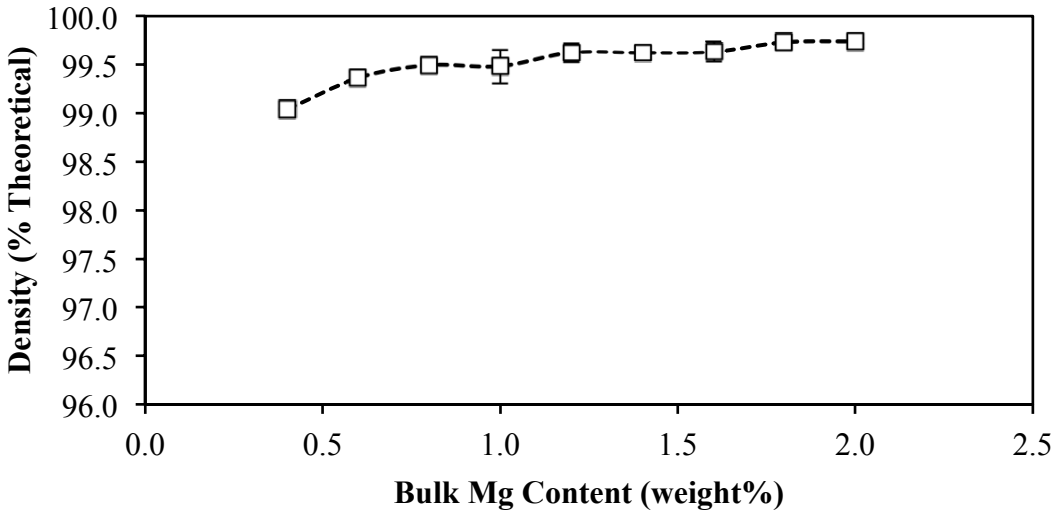

(b)

Figure 43. Effect of alloying additions on the sintered density of (a) Al-1.5Mg-xSn and (b) Al-xMg-1.5Sn ($0.4 \leq x \leq 2.0$) PM alloys.

3.4.2 Microstructure Characterization

Initial characterization of the sintered microstructures emphasized electron microscopy. In all instances sintered materials were principally comprised of a matrix of α-aluminum grains (grey) along with a bright intergranular component and the sporadic presence of residual porosity (black). Despite these similarities, certain differences were also observed. The most obvious came about when the alloys with varying tin concentration were analyzed. Here it was evident that the microstructure changed progressively as the concentration of tin was raised (Figure 44). In particular, there was a visible decrease in the number and size of the pores, along with an increase in the relative amount of the bright secondary phase. Conversely, imaging of sintered alloys with a fixed tin content (the Al-xMg-1.5Sn series) revealed that all samples were similar in the general appearance of their underlying microstructure, with no obvious transitions noted. An image of Al-1.4Mg-1.5Sn that is representative of these PM materials, and depicts all of the features consistently observed, is shown in Figure 45.

Chemical analyses indicated that as the bulk tin content was increased, there was a marginal, but somewhat inconsistent decrease in the amount of magnesium found within the α-aluminum grains (Figure 46(a)). In one instance (Al-1.5Mg-0.8Sn), the average concentration of magnesium in the bulk grains exceeded the total amount present in the alloy. This indicated that there were heterogeneities within the distribution of magnesium throughout this particular sample. This was further exemplified by the abnormally large standard deviation for this particular specimen. Furthermore, as the bulk magnesium content was increased in alloys with a static tin concentration of 1.5%, so too did the concentration of magnesium within the α-aluminum grains (Figure 46(b)). However, measured values consistently fell below the bulk magnesium concentrations indicating that a portion of this element was present in another phase(s) within the microstructure. The corresponding tin concentrations were marginally detectable in all instances (Figure 46) consistent with the negligible solubility of tin in aluminum.

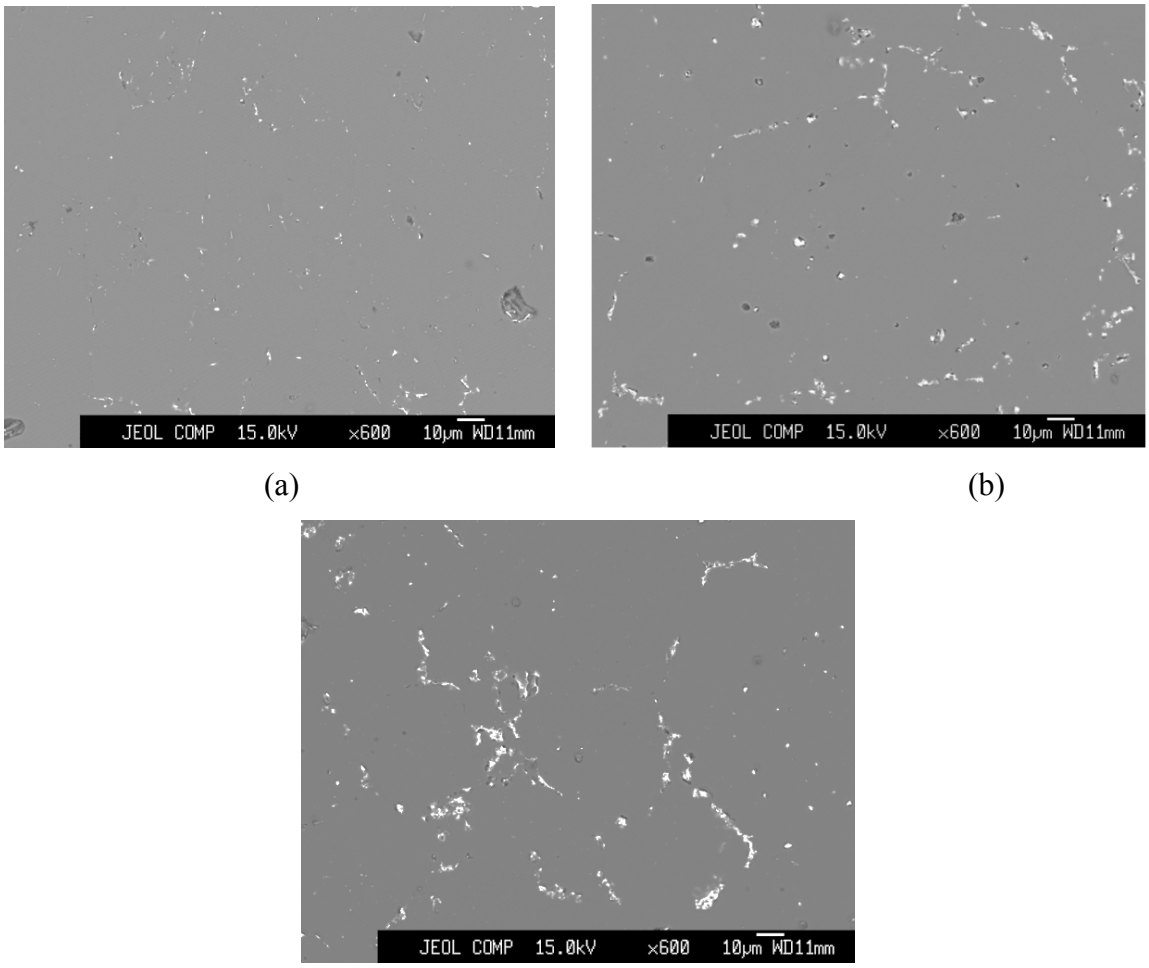

Figure 44. Microstructures of (a) Al-1.5Mg-0.4Sn, (b) Al-1.5Mg-1.2Sn, (c) Al-1.5Mg-2.0Sn as observed via EPMA in backscatter imaging mode.

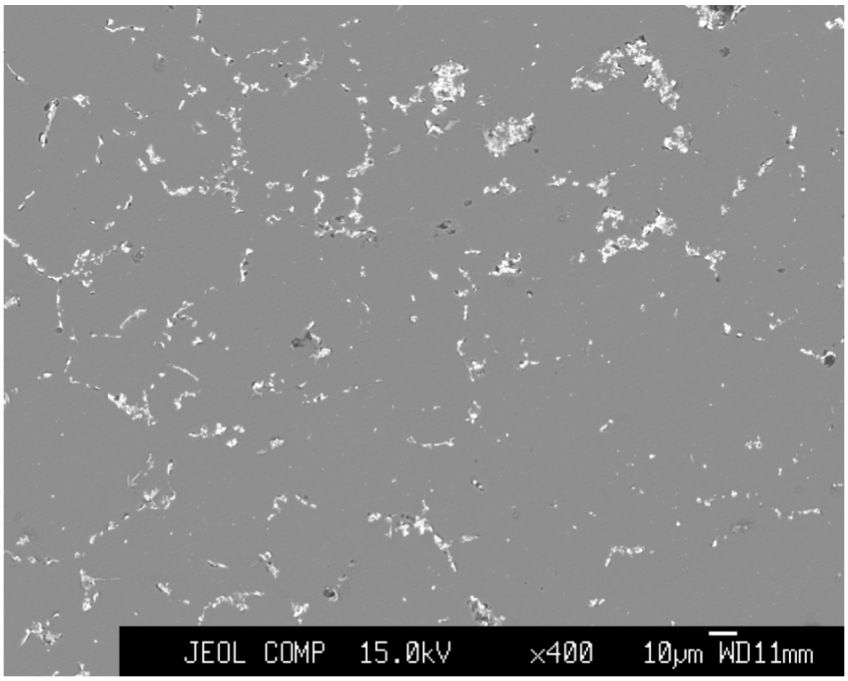

Figure 45. Microstructure of Al-1.4Mg-1.5Sn as observed via EPMA in backscatter imaging mode.

WDS analyses of the bright intergranular feature present in the PM alloys confirmed that it was enriched in magnesium and tin in all instances. The composition of this particular feature was found to vary to a considerable degree, suggesting that it was multi-phased in character. Higher magnification, scanning electron imaging was supportive of this (Figure 47) as atomic contrast indicated that there was multiple phases present albeit too small for distinct WDS analyses. However, the Mg:Sn atomic ratio approached a value of ~1:2 suggesting the possible presence of the binary intermetallic magnesium stannide (Mg_2Sn).

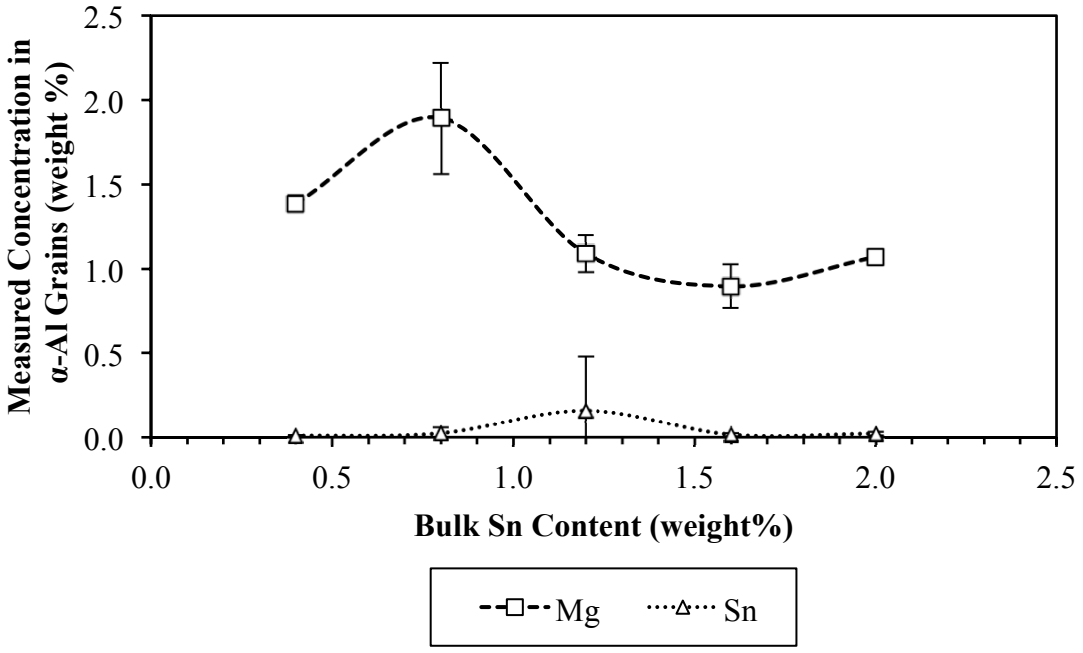

(a)

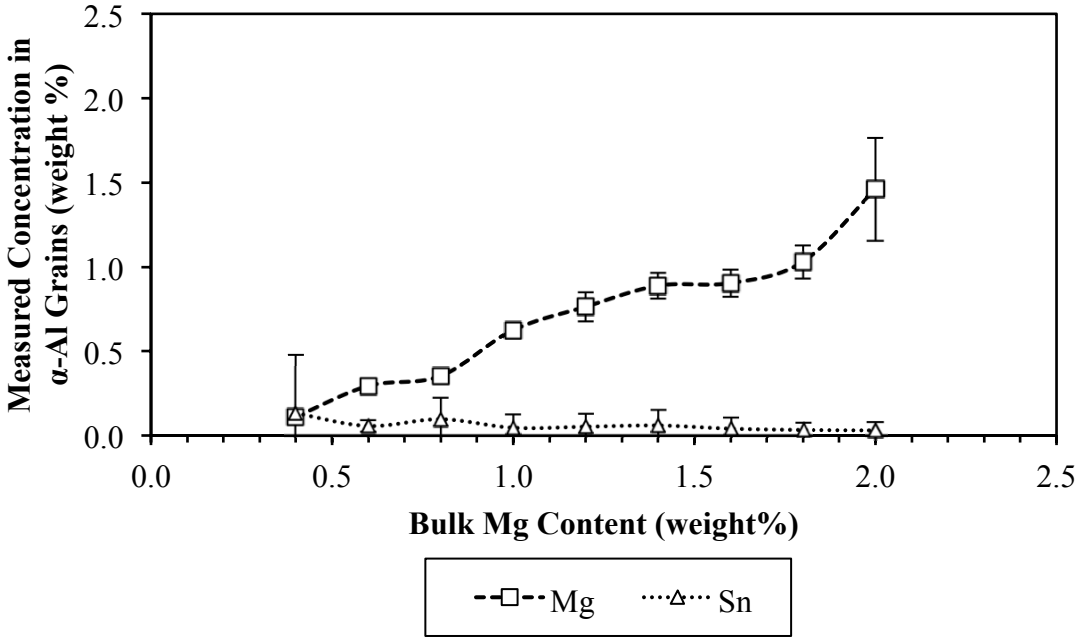

(b)

Figure 46. Average concentrations of magnesium and tin measured in the α-aluminum grains of (a) Al-1.5Mg-xSn and (b) Al-xMg-1.5Sn ($0.4 \leq x \leq 2.0$) PM alloys.

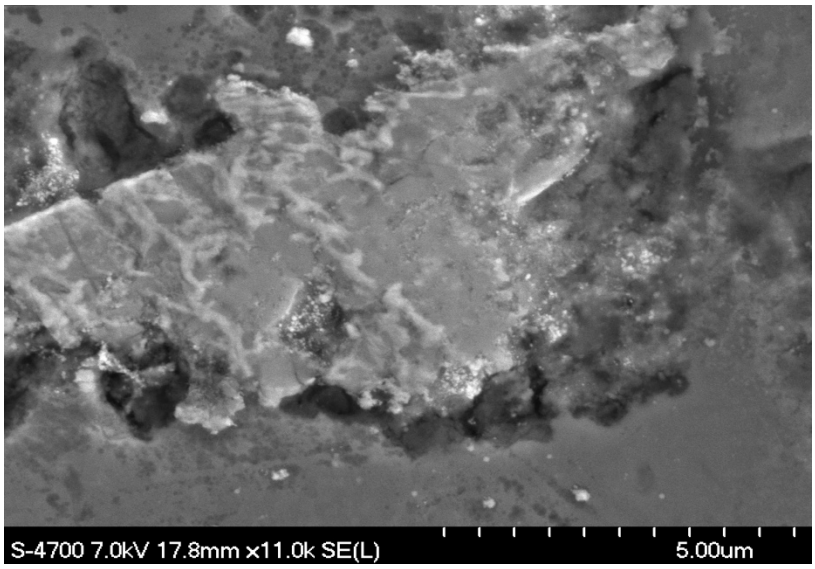

Figure 47. High magnification image of the bright intergranular feature commonly observed in Al-xMg-xSn ($0.4 \leq x \leq 2.0$) PM alloys.

XRD results confirmed that there were clear transitions in the types and amounts of the principal phases present in both series of experimental PM alloys. In the Al-1.5Mg-xSn family, the only phases detected in all spectra were α-aluminum and the intermetallic magnesium stannide (Mg_2Sn). Minor concentrations of free tin were only observed in the sample with the highest tin content of 2% (Figure 48(c)). Data confirmed that the peaks for Mg_2Sn increased in size with increasing amounts of tin, implying a progressively greater reaction between magnesium and this element. This reaction would have consumed magnesium and thereby reduced its concentration within the aluminum grains, consistent with the EPMA data (Figure 46). Interestingly, this was only effective up to a point, as the amounts of magnesium in the grains fell to a consistent value of ~1% despite the fact that progressively higher amounts of tin were still added.

Exemplary spectra that illustrate similar transitions in the Al-xMg-1.5Sn system are shown in Figure 49. In the alloy with 0.4% Mg, the confirmed phases were α-aluminum, elemental tin and a relatively low concentration of magnesium stannide. In alloys prepared with progressively higher concentrations of magnesium, the peaks for elemental tin steadily decreased while those for Mg_2Sn increased. This continued up to bulk magnesium contents ≥1.2%, at which point elemental tin was no longer detected. As

peaks were not observed in any spectra for elemental magnesium, this indicated that it had reacted completely during sintering to form Mg_2Sn and/or diffuse into the α-aluminum grains (Figure 49). For the latter, it was postulated that magnesium was primarily present in solid solution given that XRD analyses showed no firm evidence of any other Mg-bearing phases such as Al_3Mg_2.

Microstructural analyses confirmed that magnesium was able to diffuse into the α-aluminum grains and to react with tin to form Mg_2Sn upon sintering. Both Mg-based reactions occurred in all of the alloys studied regardless of bulk composition. Conversely, tin remained concentrated within the intergranular regions where it principally resided as Mg_2Sn in tandem with its elemental form in certain instances. Moreover, increasing the amount of tin allowed for a greater concentration of the intergranular constituent and also served to impede the diffusion of magnesium into solid solution, albeit to a small degree. Collectively, these general trends are consistent with ternary phase diagram predictions [94]. In this sense, tin is known to have negligible solubility in aluminum at all temperatures whereas significant levels of magnesium (~2% at 630°C) are dissolvable. Furthermore, within the region of concentrations explored, the only reported intermetallic that contains tin is Mg_2Sn.

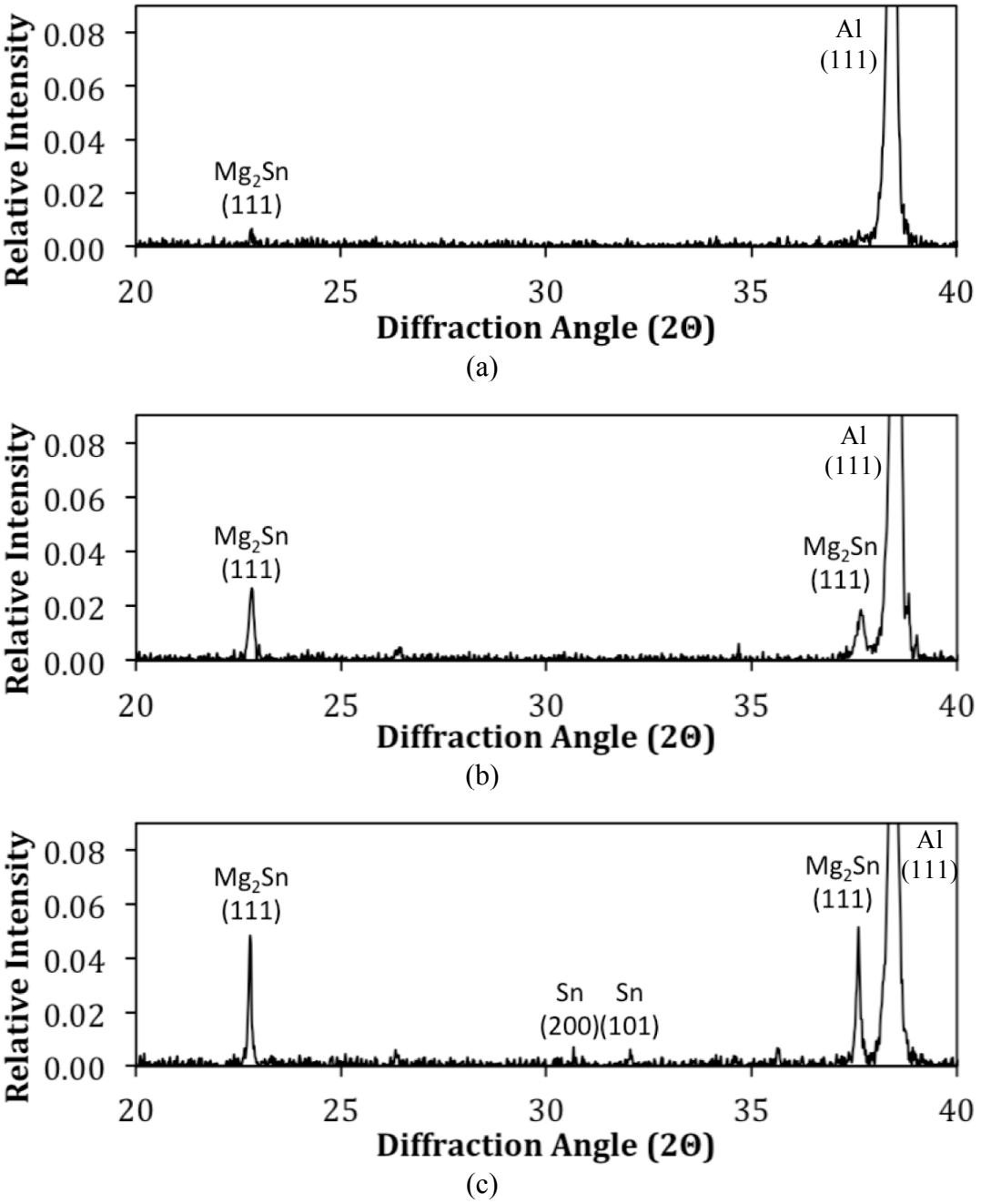

Figure 48. XRD spectra recorded from (a) Al-1.5Mg-0.4Sn, (b) Al-1.5Mg-1.2Sn, and (c) Al-1.5Mg-2.0Sn.

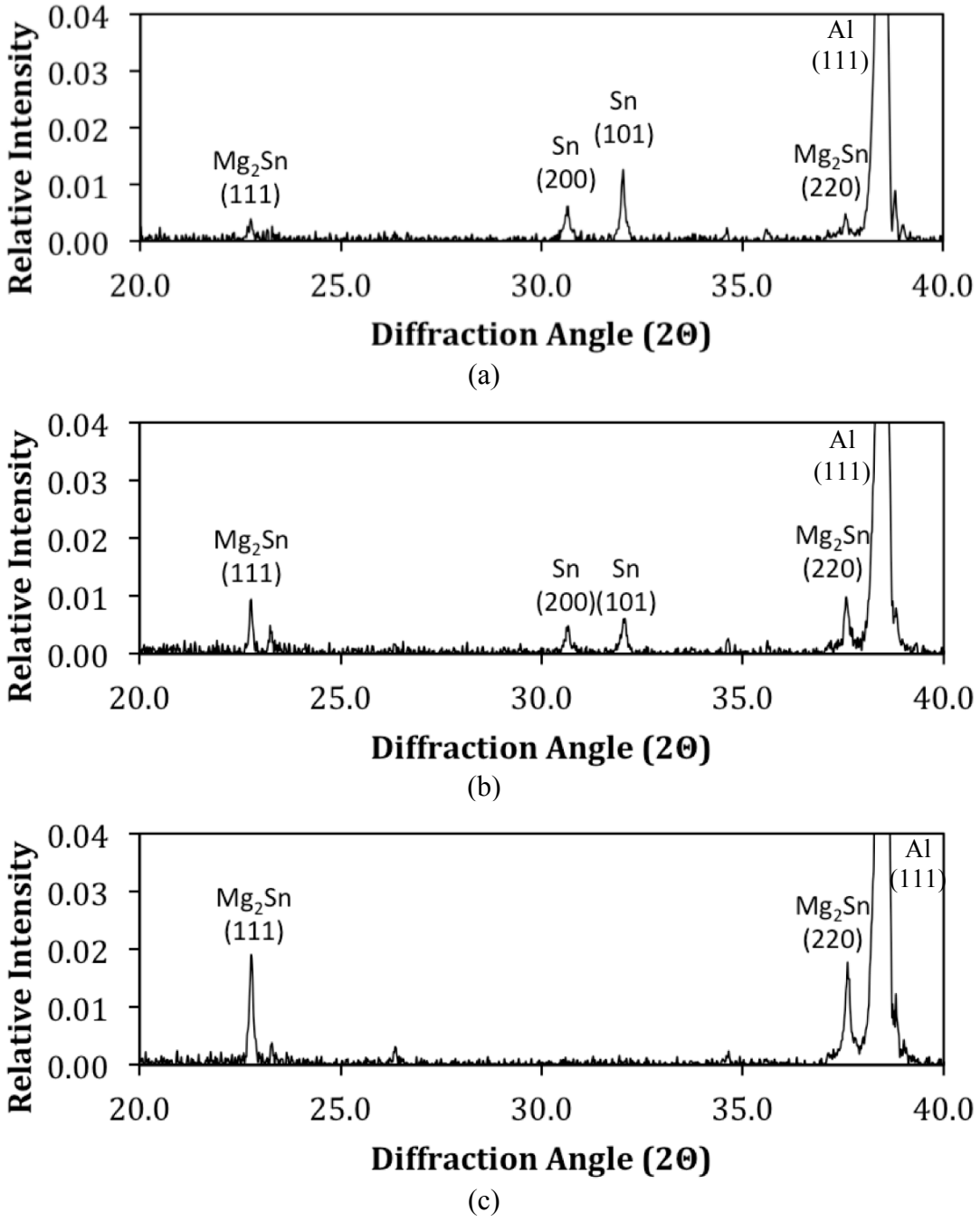

Figure 49. XRD spectra recorded from (a) Al-0.4Mg-1.5Sn, (b) Al-0.8Mg-1.5Sn, and (c) Al-1.2Mg-1.5Sn.

3.4.3 Thermal Property Measurements

Initially, specific heat capacity (C_p) curves were generated for each alloy using DSC. This property exhibited a gradual increase with rising temperature for both series of alloys (Figure 50). The variation among alloys within a particular series did not follow any definitive trend as all values were within close proximity for a given temperature. Therefore, it was concluded that changing the ternary formulations within the range studied had no perceptible effect on heat capacity and variation in data from the single runs was attributed to an acceptable level of error. It is worthy to note that residual porosity had minimal impact on C_p as well. This was evident by the fact that the alloy with the highest level of porosity (Al-1.5Mg-0.4Sn) exhibited an equivalent C_p to samples that were effectively fully dense. Overall, the only factor of any appreciable influence was temperature.

In the next sequence of tests data on thermal diffusivity (α) were acquired as functions of temperature. Exemplary results from LFA tests completed on a number of different alloys from ambient to 250°C are shown in Figure 51. With systematic increases in tin concentration, there was a progressive increase in α at all temperatures (Figure 51(a)) given the upward shift of the complete curve. Interestingly, the opposite trend was noted in alloys wherein the magnesium level changed (Figure 51(b)); here, α improved as bulk magneisum content decreased. It was also noted that separation among the α plots for alloys of differing magnesium content was appreciably larger than that observed in PM alloys of varying tin. For instance, at 100°C the maximum spread between α values was 6 mm^2/s in the Al-1.5Mg-xSn series but more than doubled to 14 mm^2/s in the Al-xMg-1.5Sn family. A more comprehensive view of this difference was illustrated by plotting α as a function of alloy chemistry for a fixed temperature (Figure 52). In the Al-1.5Mg-xSn series alloys, there was an overall trend towards moderately higher thermal diffusivity in materials with increased concentrations of tin. Conversely, in Al-xMg-1.5Sn alloys an opposing trend was observed in that the thermal diffusivity was found to steadily decrease with progressively higher concentrations of magnesium. These findings confirmed that both alloying elements influenced thermal diffusivity, but in opposing ways and that the effect was more pronounced for magnesium.

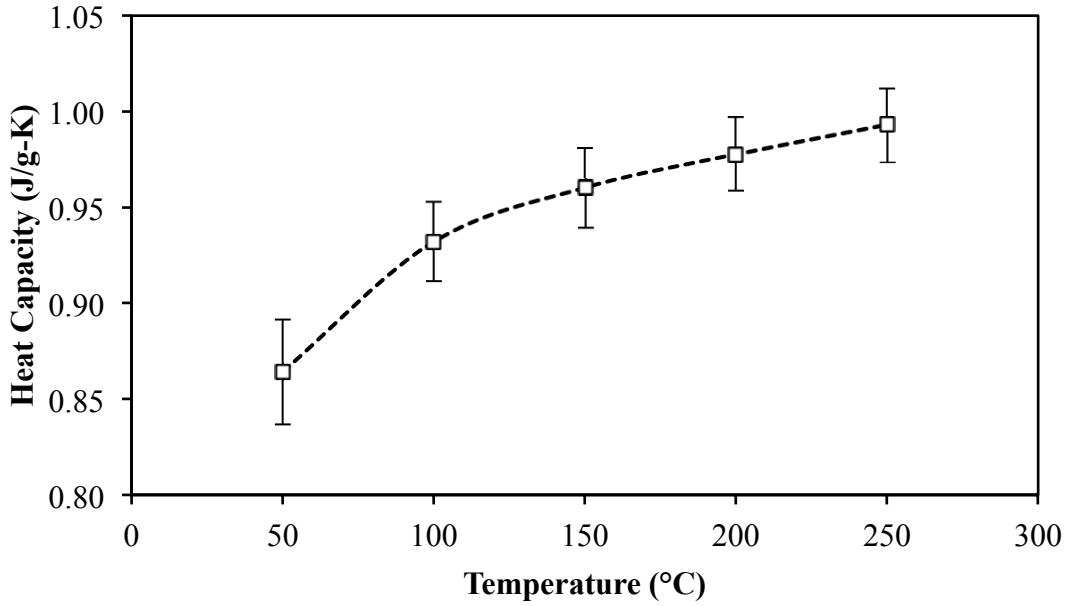

(a)

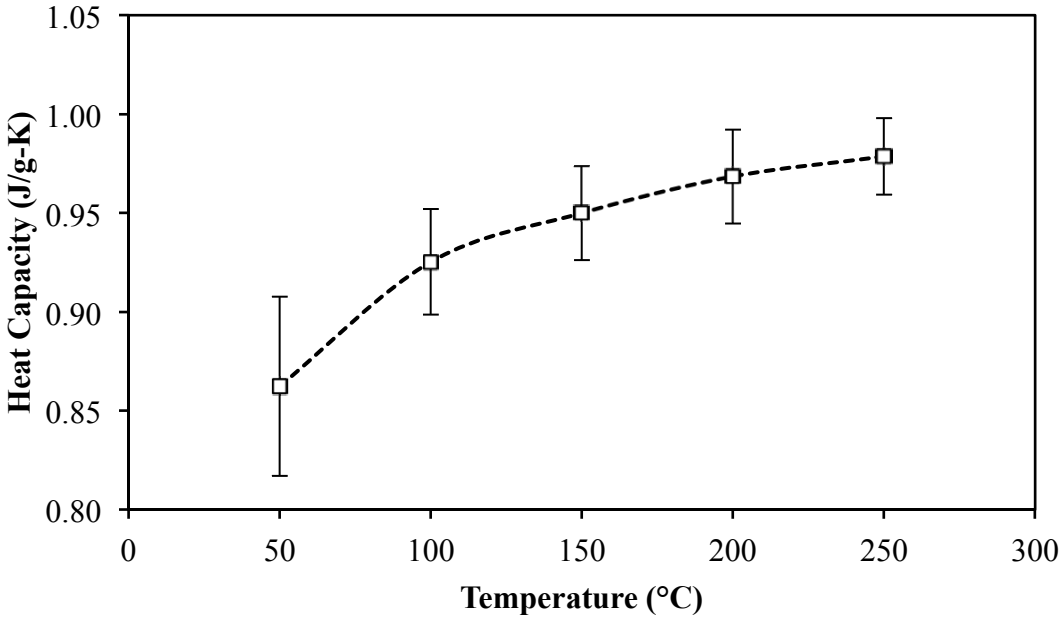

(b)

Figure 50. Influence of temperature on the average heat capacities of (a) Al-1.5Mg-xSn and (b) Al-xMg-1.5Sn PM alloys ($0.4 \leq x \leq 2.0$).

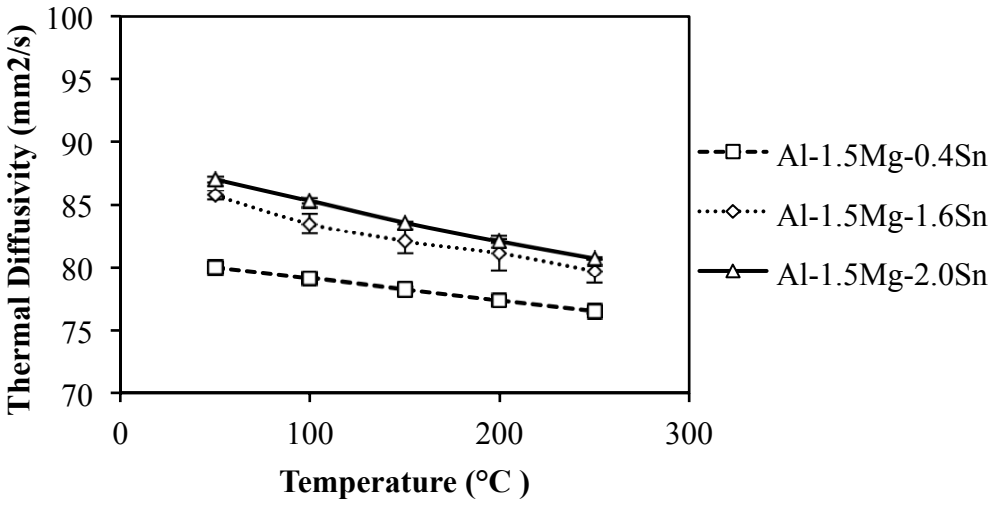

(a)

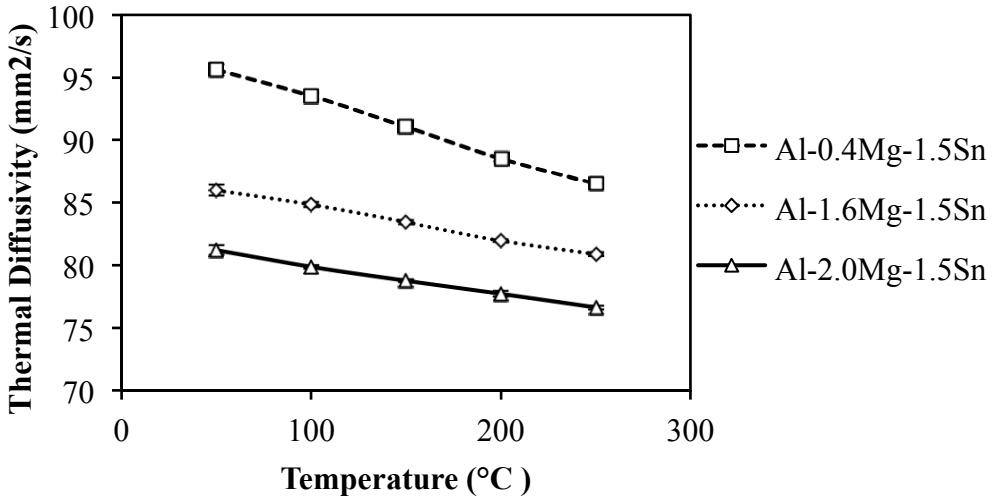

(b)

Figure 51. Influence of temperature on the thermal diffusivity of representative (a) Al-1.5Mg-xSn and (b) Al-xMg-1.5Sn PM alloys ($0.4 \leq x \leq 2.0$).

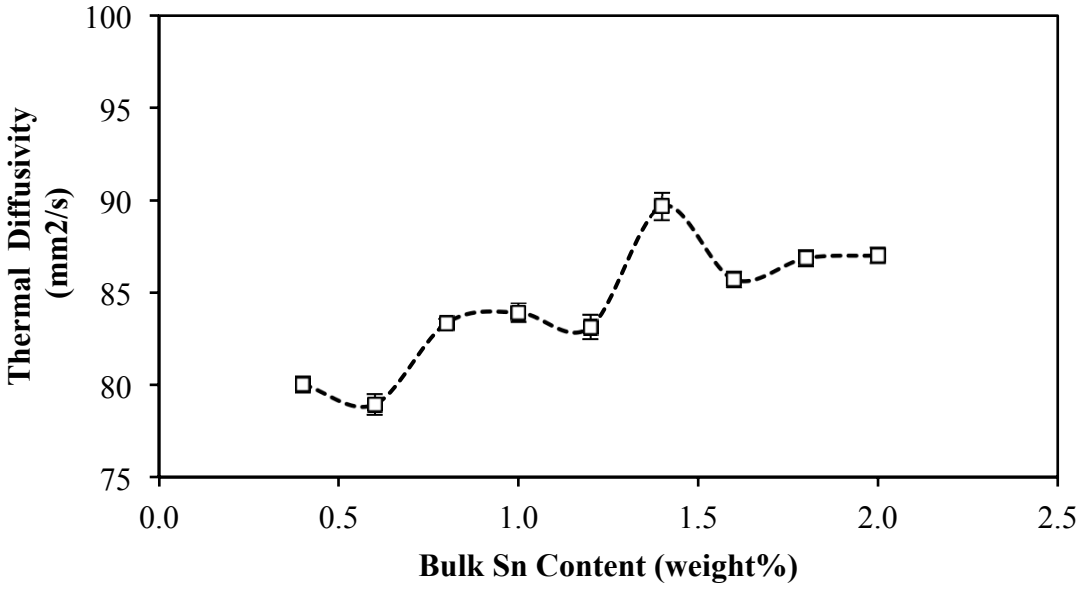

(a)

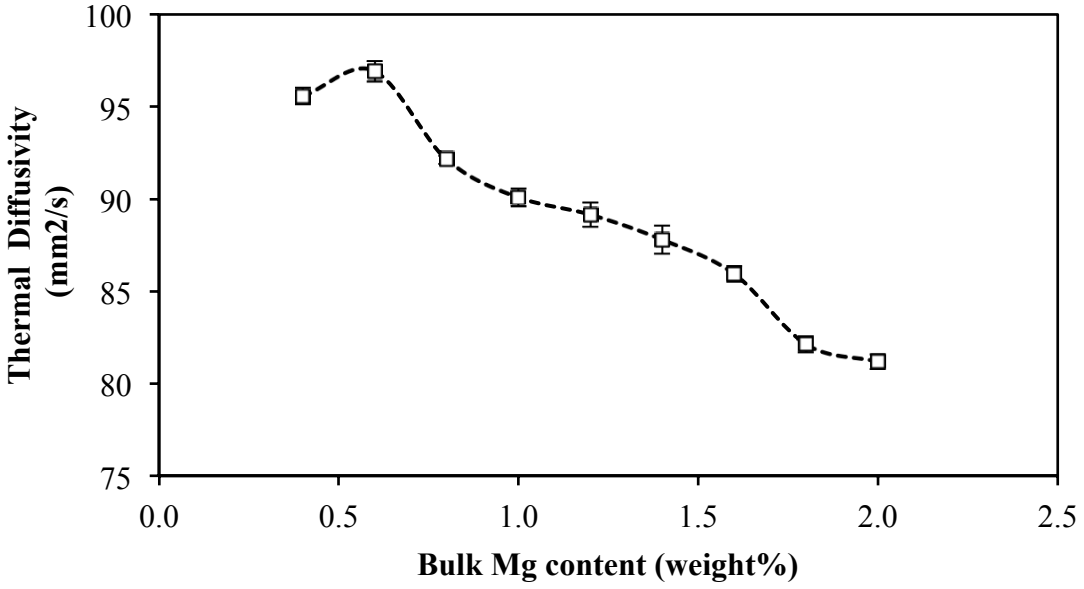

(b)

Figure 52. Variation in thermal diffusivity with bulk chemistry in (a) Al-1.5Mg-xSn and (b) Al-xMg-1.5Sn PM alloys ($0.4 \leq x \leq 2.0$). Data gathered from specimens at 50°C.

The final property measured was the coefficient of thermal expansion (CTE). Data on this attribute were required so as to determine the change in density that occurred in the materials over the temperature range of interest. Dilatometry tests were completed on a specimen of high purity (99.999%) aluminum and one of the more heavily alloyed PM materials (Al-1.5Mg-1.5Sn) for comparison purposes. The resultant CTE data measured in increments of 50°C are given in Table 7. Both materials exhibited a comparable response such that the average difference was only 0.2% among the measurements. Since the thermal expansions of these two materials were essentially equivalent, it was assumed that the other experimental PM alloys would behave in a similar manner.

Assuming that the PM materials expanded in an isotropic manner, the corresponding coefficient of volumetric expansion (α_v) was determined by simply multiplying the CTE over three dimensions for each temperature increment. Applying the relationship: $\frac{dV}{V_o} = \alpha_v dT$, the density for each specimen was calculated to have decreased by approximately 0.01 g/cm^3 with each incremental temperature rise of 50°C. The changing values of density were then utilized in the calculation of thermal conductivity as described in the following paragraphs.

Table 7. Comparison of the CTE values measured for pure aluminum and PM Al-1.5Mg-1.5Sn over various temperature ranges.

Temperature Range (°C)	**CTE (mm mm^{-1} K^{-1} x 10^6)**	
	Pure Aluminum	PM Al-1.5Mg-1.5Sn
RT – 50	21.0	21.4
50 – 100	24.6	24.6
100 – 150	27.4	27.1
150 – 200	26.1	26.2
200 – 250	27.2	27.1

With data on heat capacity, thermal diffusivity, and density all known over the complete temperature range of interest, the corresponding calculation of thermal conductivity (K) values commenced. Data on the two series of PM alloys are presented in Figure 53 as functions of temperature. Each PM alloy exhibited a similar phenomenon in that peak thermal conductivity was achieved at close to 100°C and then either plateaued, or began

to regress in a subtle manner as temperature shifted to higher values. Interestingly, it is known that the thermal conductivity of pure wrought aluminum varies in a similar manner transitioning from 237 up to 240 and then down to 233 $Wm^{-1}K^{-1}$ at temperatures of 25, 100, and 300°C respectively, due to more frequent electron collisions and scattering [95].

When directly assessing thermal conductivity as a function of bulk alloy chemistry (constant temperature) a number of trends were noted (Figure 54). The series of alloys with varying tin showed the same trend found for thermal diffusivity; namely, that there was a gradual rise in thermal conductivity with increased bulk tin concentration. The peak thermal conductivity in this series of alloys was 208±8.7 $Wm^{-1}K^{-1}$ and occurred in the alloy with 1.4% tin. Higher tin concentrations yielded sintered materials with similar thermal conductivities. Hence, a minimum tin content of 1.4% was deemed to be appropriate for enhanced heat dissipation. Changes in density did not have any measureable effect on thermal conductivity, since the property remained essentially static in alloys with 0.4 and 0.6% tin despite the fact that differences in density were known to exist (Figure 43). The results for the Al-xMg-1.5Sn series showed a decrease in thermal conductivity with increasing magnesium. The highest calculated value for this series was 225±9.5 $Wm^{-1}K^{-1}$, which occurred in PM alloy Al-0.6Mg-1.5Sn. Not surprisingly, these results, again, show a similar trend to that found in thermal diffusivity wherein a lower bulk concentration of magnesium was favored.

Although the aforementioned trends were opposing from the perspective of bulk alloy chemistry, they each worked to modify the underlying microstructure in a similar manner. In particular, with regards to the amount of magnesium that diffused into the aluminum matrix grains. Here, it was confirmed that tin reacted with magnesium to form Mg_2Sn and that the extent of the reaction increased as more tin was included in the alloy. Magnesium stannide is a relatively stable compound that melts in a congruent manner at 771°C. Given that sintering occurred at a lower temperature of 630°C, formation of the reaction product would have subsequently limited the amount of magnesium that was free to dissolve into the aluminum grains. In this scenario, raw powder particles of elemental

tin and magnesium would need to be in direct contact during the sintering process to facilitate their reaction. This would not always be the case for each and every particle in light of the relatively low concentrations studied. Indeed, some portion of the magnesium particles would be in contact with aluminum particles alone thereby prompting diffusion into the matrix metal as opposed to reacting with tin. Tin additions thereby exerted a degree of control over the amount of magnesium in the aluminum grains but the approach was somewhat indirect. Lowering the bulk magnesium content was a more definitive means of reducing the amount of this element that was dissolved in the aluminum grains. Hence, this invoked a steeper transition in thermal conductivity with composition (Figure 54) and the realization of sintered materials with an even higher capacity for heat dissipation.

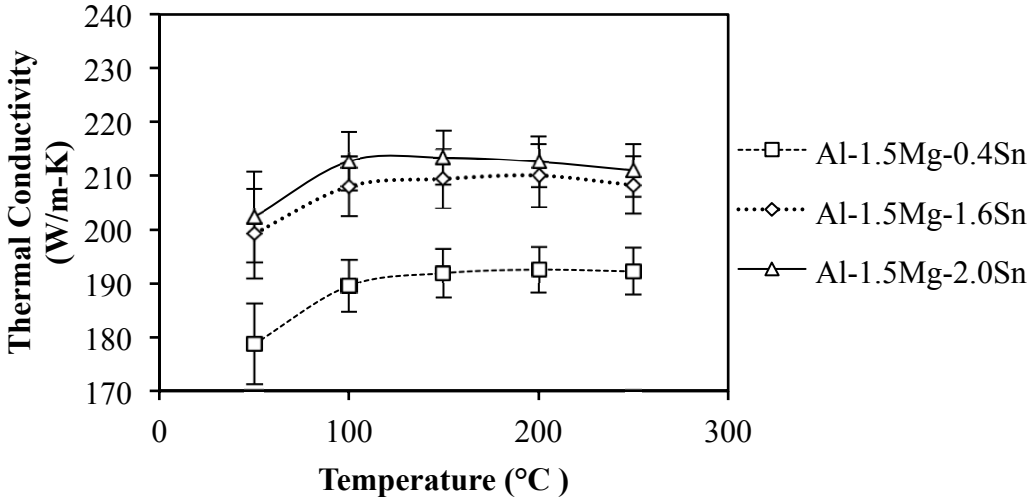

(a)

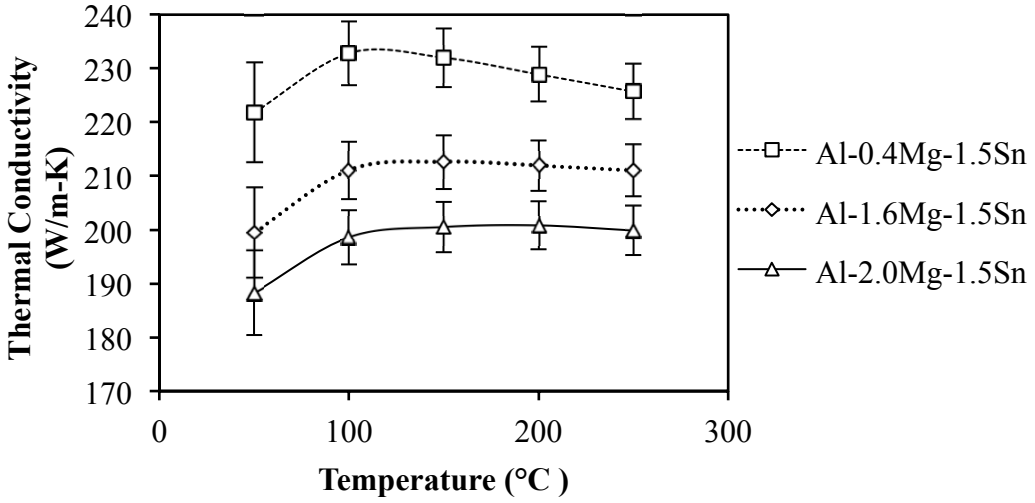

(b)

Figure 53. Influence of temperature on the thermal conductivity of PM alloys from the (a) Al-1.5Mg-xSn and (b) Al-xMg-1.5Sn ($0.4 \leq x \leq 2.0$) series.

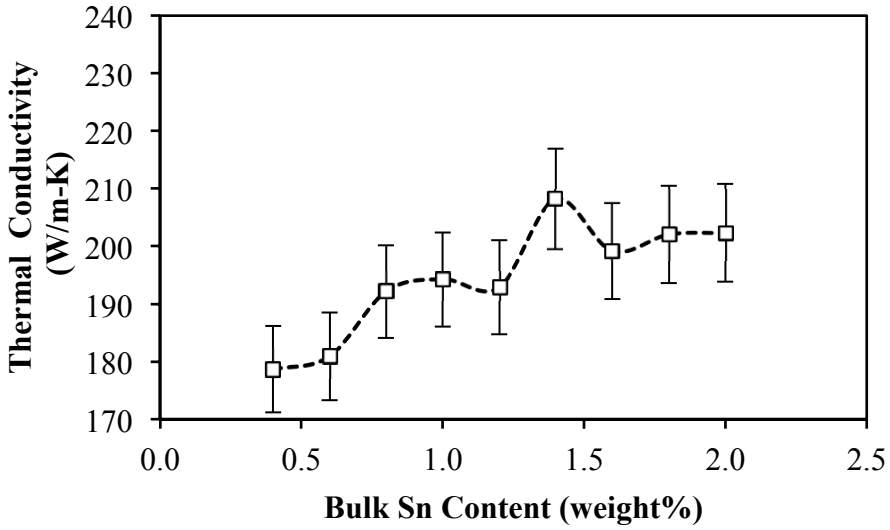

(a)

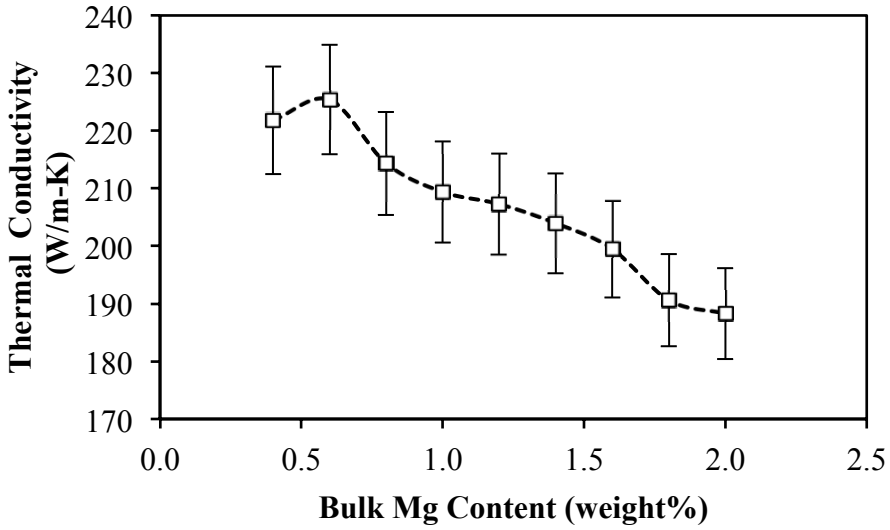

(b)

Figure 54. Variation in the calculated thermal conductivity with bulk chemistry in (a) Al-1.5Mg-xSn and (b) Al-xMg-1.5Sn PM alloys ($0.4 \leq x \leq 2.0$). Data gathered from specimens heated to 50°C.

To verify the accuracy of thermal conductivity values derived from first principal calculations ($K = \alpha\, C_p\, \rho$), bulk thermal conductivity measurements were also completed using a TPS approach on larger samples of select PM alloys. Comparisons of the resultant values achieved with each approach are shown in Table 8. In all instances the agreement between the methods was within 0.5 to 5% confirming the accuracy of the experimental approach. As such, the experimental PM alloys clearly exhibited thermal conductivities that rivaled that of pure aluminum [95], which was viewed as a promising development.

To place the new PM systems in greater industrial context, additional tests were completed on a number of materials commonly employed in the commercial production of aluminum heat sinks (Table 9). Industrially, such devices are typically machined from wrought bar stock or die cast. In die casting operations, alloy A390 is one of the alloys commonly employed. However, as shown in Table 9, this particular system exhibited a thermal conductivity that was nearly 60% less that the highest performing PM alloy. Although not tested in this work, another common die casting alloy is A380. With a reported thermal conductivity of only 96 $Wm^{-1}K^{-1}$ [96], the advantage that the PM-based materials have over this type of die cast alloy is even more striking. When higher levels of thermal conductivity are needed wrought 6xxx series alloys such as 6061 and 6063 are commonly utilized. Measurements on these materials revealed thermal conductivities that were again inferior to the most conductive PM material developed. Furthermore, the advantageous position of the PM alloy was maintained over the full range of temperatures assessed (Figure 55).

It is also worthy to note that the advantageous thermal conductivity was not simply a fundamental trait of any PM-processed alloy. To substantiate this notion, measurements were also completed on the standard commercial PM alloy AC2014 (Table 9). This particular alloy has been utilized in high volume production since the mid 1990's and currently remains the preferred material for PM component manufacture [97]. The thermal conductivity of this material was largely comparable to die cast A390 and as such, it too was demonstrably inferior to the new PM materials developed.

Table 8. Thermal conductivities of select PM alloys as acquired through transient plane source (TPS) measurements and when calculated from fundamental material properties.

	Thermal Conductivity ($Wm^{-1}K^{-1}$)	
Alloy	TPS (20°C)	Calculated (50°C)
Al-0.4Mg-1.5Sn	224.6 ± 0.7	221 ± 9.3
Al-1.0Mg-1.5Sn	214.8 ± 2.0	209 ± 8.8
Al-2.0Mg-1.5Sn	186.8 ± 0.6	188 ± 7.9
Al-1.5Mg-2.0Sn	212.4 ± 1.1	202 ± 8.4

Table 9. Average thermal conductivities measured at 50°C for experimental and commercial aluminum-based materials.

Alloy	**Thermal Conductivity** ($Wm^{-1}K^{-1}$)
PM Al-0.6Mg-1.5Sn	225.4
Die Cast A390	142.3
Wrought 6061-T6	195.3
Wrought 6063-T1	217.1
PM AC2014-T1	144.3

Overall, the thermal conductivity of numerous PM materials studied in this work was >200 $Wm^{-1}K^{-1}$ with select alloys achieving values upwards of 225 $Wm^{-1}K^{-1}$. Such capacity for heat dissipation approaches the known values of highly conductive pure aluminum and exceeds that of conventional aluminum-based alloys traditionally employed in heat sink manufacture. Coupling this material property advantage with the near-net-shape manufacturing capabilities inherent to aluminum PM processing is felt to present a novel and strategic approach towards the near-term manufacture of heat dissipating devices in an economical manner.

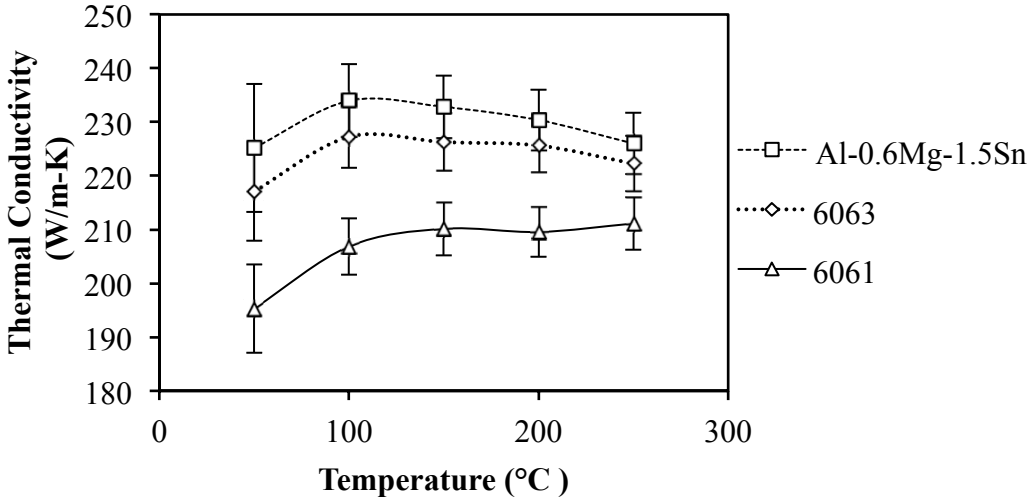

Figure 55. Comparison of the thermal conductivities measured for PM alloy Al-0.6Mg-1.5Sn, wrought 6061-T6 and wrought 6063-T1 as functions of temperature.

3.5. Conclusions

In completing the research detailed in this paper, the following conclusions have been reached:

1. All of the Al-Mg-Sn PM alloys considered in this study were responsive to sintering and the majority could be sintered to >98.8% of their full theoretical value.
2. The microstructures of all PM alloys included aluminum grains, Mg_2Sn and in select instances, elemental tin.
3. As the bulk content of Mg was increased, so too did the amount of Mg in solid solution within the aluminum grains. Conversely, Sn was found to impede the diffusion of Mg into the α-aluminum grains through a reaction that prompted the formation of Mg_2Sn.
4. Heat capacities of the PM materials increased in systematic a manner with temperature. However, bulk alloy chemistry did not have a clear effect.
5. Increasing concentrations of magnesium had a negative influence on thermal conductivity whereas tin concentrations had an opposing effect. It was postulated that this behaviour was directly attributable to the influence of each element on the concentration of magnesium dissolved within the aluminum grains.

6. The PM alloy Al-0.6Mg-1.5Sn exhibited a nominal thermal conductivity of 225$Wm^{-1}K^{-1}$. This was the highest value measured for the PM systems assessed and was at a level that was comparable to wrought heat sink materials and highly advantageous over those that are die cast.

CHAPTER 4. SUMMARY AND CONCLUSIONS

This research focused on steering away from the traditional processing means of fabricating aluminum heat sink alloys in order to create new research opportunities and effectively expand the market for PM manufacturing. By employing a PM approach, it was possible to create new materials, comprised of aluminum, magnesium and tin, which yielded thermal properties rivaling the highest performing wrought and cast aluminum alloys in production today. This was accomplished by leveraging the proven advantages of PM processing such as precise control over alloying additions and liquid-phase sintering. The first step in this new alloy development was to analyze the sintering response of a series of alloys with varying concentrations of magnesium and tin. From there, two methods of thermal analysis were employed: i) a calculated approach based on discrete measurements of pertinent physical properties (namely, heat capacity, density, and thermal diffusivity) and ii) direct thermal conductivity evaluations using a TPS unit.

4.1. Sintering Response

The PM sintering response of each experimental alloy was characterized through density measurements, electron microscopy, chemical analysis, and x-ray diffraction. Each of these measurement techniques proved to be helpful in understanding the underlying metallurgical properties.

4.1.1. Density Measurements

It was found that tin played the predominant role in achieving high levels of densification through the formation of a liquid phase during sintering. Small levels of tin (>0.4 weight%) combined with 1.5 weight% magnesium resulted in highly dense (>99.0% of full theoretical) alloys. Even lower concentrations of magnesium (0.4 weight%) were found to effectively break up the refractory oxide layer surrounding the aluminum powder particles, thereby promoting interparticle diffusion and an intense sintering response.

4.1.2. Microstructure Analyses

Visually, SEM and EPMA showed that each of the experimental PM alloys were multi-phase in nature. The matrix was comprised of seemingly 'pure' α-aluminum grains with

sparse pores intermittent throughout. Along the grain boundaries there was a secondary phase, which varied in concentration according to the amount of tin present in the starting powder blend. Under higher magnification, this secondary phase was actually found to be comprised of several different structures, albeit too small for separate analyses. Due to the nature of the materials, the clearest images were obtained through EPMA using a backscatter detection mode.

Using WDS it was possible to determine the bulk-grain chemistry of each alloy to better predict/understand the subsequent thermal properties. Not surprisingly, each alloy was found to have small amounts of magnesium present in the α-aluminum grains. Furthermore, the magnesium content increased as the amount of magnesium in the starting powder blend was raised. The tin was, for the most part, absent from the aluminum grains due to its negligible solubility in aluminum. However, it did have some effect on the amount of magnesium present in the grains. The secondary, intergranular phase was resolved to be rich in tin and magnesium, leading to the assumption that it was comprised mainly of magnesium stannide with excess elemental tin.

In order to substantiate these findings, XRD was conducted on each sample. These results confirmed that the only detectable phases in each of the experimental materials were α-aluminum, Mg_2Sn, and in certain cases, elemental tin. Tin was only detected in the alloys with starting chemistries that were rich in tin (≥1.4 weight%) or lean in magnesium (<1.0 weight%).

4.2. Thermal Analysis

The two methods used to analyze the thermal conductivity of PM alloys were found to deviate by 0.5-5% in all cases. This validated both approaches as feasible means of thermal analysis. The calculated approach, consisting of discrete measurements, tended to result in a higher degree of error due to the subsequently compounding standard deviation of each test. This means of analysis also required more (expensive) equipment and thus was not recommended as the optimal approach. The only drawback to the bulk testing

approach was in the use of larger test samples, resulting in a higher degree of wasted material.

4.2.1. Calculated Approach

The first measured property was the specific heat capacity. The chemistry of the materials tested did not tend to vary the energy required to raise their temperature. Similarly, small amounts of porosity had no discernable effect on the heat capacity. In each instance, there was a similar rise in C_P with increasing temperature.

The thermal diffusivity, or rate of temperature change, was found to be the highest in alloys containing the lowest concentrations of magnesium. The opposite was found to be true in terms of the presence of tin. The lower values of thermal diffusivity tended to correspond with higher levels of magnesium in the α-aluminum grains and thus it was concluded that in order to maintain higher levels of thermal diffusivity, the magnesium concentration had to be kept to a minimum (~0.4 - 0.8 weight%). In terms of temperature dependence, in all instances the thermal diffusivity was found to decrease in a linear manner with increased temperature.

The CTE of the experimental alloys were determined to match that of pure aluminum, resulting in a relatively small decrease in density with increased temperature (0.01g/cm^3 per 50°C). Isotropic expansion was assumed and thus the coefficient of volumetric expansion was found by tripling the CTE.

The overall calculated thermal conductivities followed the same trend as the thermal diffusivity, in that the alloys containing the lowest concentrations of magnesium performed the best.

4.4.2 Direct Measurement

Bulk measurements of thermal conductivity using a TPS unit were found to follow the same trend as the calculated results. The main advantage was realized in the lower degree of error resulting in better repeatability.

4.3 Industrial Relevance

The highest performing novel PM alloy (Al-0.6Mg-1.5Sn) was found to be comparable with wrought 6063 in the T1 temper. Furthermore, Al-0.6Mg-1.5Sn was found to exceed both wrought 6061 and cast A390 in terms of thermal conductivity by 15% and 58% respectively. The level of thermal conductivity in a PM alloy is very promising. For comparison purposes, a popular commercial aluminum PM alloy (AC2014) was tested and found to have a nominal thermal conductivity of 80 $Wm^{-1}K^{-1}$ lower than that of Al-0.6Mg-1.5Sn.

Coupling this high thermal conductivity with the near-net-shape advantage of PM processing presents an excellent opportunity for PM to make inroads in the globally expanding market of aluminum heat sinks.

4.4. Future Work

Due to constraints in time, the scope of this research was limited to providing the initial framework for novel alloy development. This section outlines the recommendations for future work. The observations for further advancement of this alloy are as follows:

- Further lower the concentration of magnesium to determine, specifically, the minimum level required to achieve a highly dense sintered product.
- Look at lowering the amount of tin present in the alloys that are lean in magnesium (0.4 – 0.8%). This should help determine an optimal chemistry to achieve maximum thermal properties.
- Experiment with different alloying additions (such as boron) that may react with magnesium to inhibit diffusion into the α-aluminum grains.
- Analyze the effects on thermal properties for composite additions (AlN, SiC) in order to tailor the thermal expansion for certain applications.
- Determine the effects of sizing (cold work) on the thermal properties.
- Look for changes in the microstructure and thermal conductivity due to long-term thermal exposure.
- Experiment with varying particle size distributions for the starting powders.

- Finally, since surface area plays such a factor in the level of heat convection, it would be beneficial to delve into different surface finishes (i.e. peened, machined, porous or as-sintered).

REFERENCES

1. T.M. Tritt: *Thermal Conductivity: Theory, Properties, and Applications, 2004, Academic/Plenum Publishers, New York, NY, p. 22.*

2. A. Salazar: *Eur. J. Phys., 2003, vol. 24, no. 4, pp. 351-358.*

3. R.P. Tye: *Thermal Conductivity, 1969, vol. 2, Academic Press, New York, NY, p. 218.*

4. Edited by R. E. Taylor: *Thermal Conductivity, 1968, vol. 8, United States Department of Congress, National Bureau of Standards, p.797.*

5. J.Y. Barghout: *Mater. Sci. Forum, 1996, vol. 217, no. 2, pp. 975-980.*

6. C. Kittel: *Introduction to Solid State Physics, 1986, 6th, Wiley, p. 150.*

7. A.M. Ramirez: *J. Mater. Res., 1999, vol. 14, no. 10, pp. 3901-3906.*

8. L.R. Ingersoll, O. J. Zobel, & A. C. Ingersoll: *Heat Conduction, with Engineering and Geological Applications, 1948, McGraw-Hill Book Co., p. 4.*

9. A.V. Luikov: *Analytical Heat Diffusion Theory, 1968, Academic Press, Inc., New York, NY, p. 7, 20.*

10. D.R. Askeland, & P. Webster: *The Science and Engineering of Materials, 1990, Chapman and Hall, p. 756.*

11. W. Kauzmann: *Thermodynamics and Statistics: with Applications to Gasses, 1967, W.A. Benjamin, Inc., New York, NY, p. 41.*

12. C. Kittle: *Thermal Physics, 1969, John Wiley & Sons, New York, NY, pp. 230-234*

13. Edited by C.Y. Ho & R.E. Taylor: *Thermal Expansion of Solids, 1998, ASM International, Materials Park, OH, pp. 1-2, 121-127.*

14. K. Hori: *J. Jpn. I. Met., 1955, p. 19.*

15. F. Ono & H. Maeta: *J. Phys. - Paris, 1988, vol. 49, no. 12, pp. 63-64.*

16. F. Cverna: *ASM ready reference: Thermal properties of metals, 2002, ASM International, Materials Park, OH, pp. 223-224.*

17. L. Pauling: *The Nature of the Chemical Bond and the Structure of Molecules and Crystals, 1960, Cornell University Press, Ithaca, NY, pp. 5-10.*

18. S.O. Kasap: *Principles of Electronic Materials and Devices, 2006, 3rd, McGraw-Hill, pp. 14-18.*

19. F.C. Campbell: *Elements of Metallurgy and Engineering Alloys, 2008, ASM International, Materials Park, OH, p. 6.*

20. L. Solymar & D. Walsh: *Lectures on the Electrical Properties of Materials, 1984, Oxford University Press, p. 3.*

21. G. Lehmann & P. Ziesche: *Electronic Properties of Metals, 1990, Elsevier, p. 81.*

22. R. H. Bube: *Electronic Properties of Crystalline Solids: An introduction to Fundamentals, 1974, Elsevier, pp. 211-233.*

23. B.R. Coles & A.D. Caplin: *The Electronic Structures of Solids, 1976, Crane Russak, pp.121-128*.

24. G.K. Narula, K.S. Narula & V.K. Gupta: *Materials Science, 1989, Tata McGraw-Hill Education, p. 227*.

25. W.R. Hamburgen: Digital Equipment Corporation, Western Research Laboratory, Palo Alto, CA, unpublished research, 1986.

26. S. Lee: *IEEE Semi-Therm™ Symposium, 11th, 1995, Laconia, NH, pp. 48-54.*

27. D.R. Poirier & G.H. Geiger: *Transport Phenomena in Materials Processing, 1994, Wiley, Section 6.1.*

28. A.T. Morrison: *ITherm 1992, Intersoc. Conf. Therm. Phenom. Electron. Syst., 1992, 3rd, Austin, TX, pp. 145-148.*

29. X.C. Tong: *Advanced Materials for Thermal Management of Electronic Packaging, 2011, Springer, pp. 374-375.*

30. J. Domingo: Lumex, Palatine, Il, unpublished research, 2011.

31. J. Szumera & J.A. Szumera: *The Metal Stamping Process: Your Product from Concept to Customer, 2003, Industrial Press Inc., pp. 1-2.*

32. W.G.E. Mosher, G.J. Kipouros, W.F. Caley, I.W. Donaldson & D.P. Bishop: *Powder Metall., 2011, vol. 54, no. 3, pp. 366-375.*

33. Metal-Stamping-China.com, Goldenmay, China, unpublished research, 2012.

34. P.K. Saha: *Aluminum Extrusion Technology, 2000, ASM International, Materials Park, OH, pp. 2-5.*

35. A. Bar-Cohen & M. Iyengar: *IEEE T. Compon. Pack. T., 2001, vol. 24, no. 2, pp. 150-158.*

36. A. Reikher & M.R. Barkhudarov: *Casting: An Analytical Approach, 2007, Springer, London, England, pp. 1-10.*

37. T.F. Waters: *Fundamentals of Manufacturing for Engineers, 1996, CRC Press, pp. 14-30.*

38. G.A. Roberts & R. Kennedy: *Tool Steels, 1998, ASM International, Materials Park, OH, p. 27.*

39. P.M. Geffroy, J. D. Mathias & J. F. Silvain: *Adv. Eng. Mater., 2008, vol. 10, no. 4, pp. 400-405.*

40. R. Saraswati and F.J. Polese: *Proc. Int. Symp. Microelectron., 1998, vol. 3582, Society of Photo-Optical Instrumentation Engineers, Bellingham, WA, pp. 681-686.*

41. T. Lye-King & J. Ma: *ITherm 2004, Intersoc. Conf. Therm. Thermomech. Phenom. Electron. Syst., 2004, 9th, vol. 1, pp. 451-454.*

42. ASM: *ASM Metals Handbook, 1990, vol. 2, ASM International, Materials Park, OH.*

43. W.F. Smith: *Structure and Properties of Engineering Alloys, 1993, McGraw-Hill, p. 162-211.*

44. G.S. Upadhyaya: *Powder Metallurgy Technology, 1997, Cambridge International Science Publishing, Cambridge, England, pp. 1-3.*

45. H. Fischmeister: *Proc. - Inst. Mech. Eng., 1982, vol. 196, pp. 105-121.*

46. H.A. Al-Qureshi, A. Galiotto & A.N. Klein: *J. Mater. Process. Technol.. 2005, vol. 166, no. 1, pp. 135-143*.

47. T. Hirohata, S. Masaki & S. Shima: *J. Mater. Process. Technol., 2001, vol. 111, no. 1-3, pp. 113-117.*

48. H.A. Al-Qureshi, M.R.F. Soares, D. Hotza, M.C. Alves & A.N. Klein: *J. Mater. Process. Technol., 2008, vol. 199, no. 1-3, pp. 417-424.*

49. V.D. Khramtsov: *Russ. J. Non-Ferrous Met., 2009, vol. 50, no. 3, pp. 294-297.*

50. H. Chtourou, M. Guillot & A. Gakwaya: *Int. J. Solids Struct., 2002, vol. 39, no. 4, pp. 1059-1075.*

51. J.R. Davis: *Aluminum and Aluminum Alloys, 1993, ASM International, Materials Park, OH, p. 143.*

52. S.C. Lee & K.T. Kim: *Int. J. Mech. Sci., 2002, vol. 44, no. 7, pp. 1295-1308.*

53. R.R. Brewin, O. Coube, P. Doremus & J.H. Tweed: *Modelling of Powder Die Compaction, 2008, Springer, pp. 121-123.*

54. L. Lefebvre: *J. Light Metals, 2002, vol. 2, no. 4, pp. 239-246.*

55. S.A. Tsukerman: *Powder Metallurgy, 1965, Pergamon Press, p. 58.*

56. T.K. Sherwood, R.L. Pigford & C.R. Wilke: *Mass Transfer, 1975, McGraw-Hill, p. 25*.

57. R.M. German: *Liquid Phase Sintering, 1985, Springer, p. 3.*

58. Z.A. Munir: *J. Mater. Sci., 1979, vol. 14, no. 11, pp. 2733-2740.*

59. J. Gurland & J.T. Norton: *Trans. AIME, 1952, vol. 194, no. 10, pp. 1045-1050.*

60. R.M. German, P. Suri & S.J. Park: *J. Mater. Sci., 2008, vol. 44, no. 1, p. 5.*

61. R.M. German: *Liquid Phase Sintering, 1985, Springer, p. 2.*

62. T. Courtney: *Metall. Mater. Trans. A, 1984, vol. 15, no. 6, pp. 1065-1074.*

63. J. Jean & T.K. Gupta: *J. Mater. Sci. Lett., 1992, vol. 11, no. 10, pp. 656-658.*

64. A. Nylund and I. Olefjord: *Powder Metall., 1993, vol. 36, no. 3, pp. 193-197.*

65. I.A. MacAskill, R.L. Hexemer Jr., I.W. Donaldson & D.P. Bishop: *J. Mater. Process. Tech., 2010, vol. 210, no. 15, pp. 2252-2260.*

66. R.N. Lumley, T.B. Sercombe & G.B. Schaffer: *Metall. Mater. Trans. A, 1999, vol. 30A, pp. 457-463.*

67. L. Darken & R. Gurry: *Physical Chemistry of Metals, 1953, McGraw-Hill, London, England, p. 349.*

68. C. Lall: *Int. J. Powder Metall., 1991, vol. 27, pp. 315-329.*

69. K. Kondoh: *Powder Metall., 2001, vol. 44, no. 2, pp. 161-164.*

70. Y.L. Zhang, H.L. Wang, H.R. Zhuang, R.S. Rao & X.R. Xu: *Chinese J. Low Temp. Phys., 2003, vol. 25, no. 2, pp. 132-136.*

71. Y. Iwamoto, A. Kuibira, I. Sigiura & J.I. Tsubaki: *J. Ceram. Soc. Jpn., 1992, vol. 100, no. 1161, pp. 652-656.*

72. J. Gao & D. Quesnel: *Metall. Mater. Trans. A, 2011, vol. 42, no. 2, pp. 356-364.*

73. C.F. Dixon: *Powder Metall., 1973, vol. 16, no. 32, pp. 366-373.*

74. G.B. Schaffer: *Mater. Sci. Forum, 2004, vol. 28, pp. 65-74.*

75. G.B. Schaffer, T.B. Sercombe & R.N. Lumley: *Mater. Chem. Phys., 2001, vol. 67, no. 1-3, pp. 85-91.*

76. T.B. Sercombe & G.B. Schaffer: *Advances in Powder Metallurgy & Particulate Materials – 1997: Proceedings of the 1997 International Conference on Powder Metallurgy & Particulate Materials, 1997, MPIF, Chicago, Il, pp. 10-21.*

77. G.B. Schaffer, Y.Y. Yao, S.J. Bonner, E. Corssin, S.J. Pas & A.J. Hill: *Acta Mater., 2008, vol. 56, pp. 2615-2624.*

78. A.A. Nayeb-Hashemi & J.B. Clark: *Bull. Alloy Phase Diagrams, 1984, vol. 5, no. 5, pp. 466-476.*

79. V. Raghavan: *J. Phase Equilib. Diffus., 2011, vol. 32, no. 1, pp. 57-60.*

80. M.L. Delgado, E.M. Ruiz-Navas E. Gordo & J.M. Torralba: *J. Mater. Process. Tech, 2005, vol. 162-163, pp. 280-285.*

81. L. Meluch: PHD candidate, University of Birmingham, Birmingham, England, unpublished research, 2009.

82. D.W. Heard, I.W. Donaldson & D.P. Bishop: *J. Mater. Process. Tech., 2009, vol. 209, no. 18-19, pp. 5902-5911.*

83. A.D. LaDelpha, H. Neubing & D.P. Bishop: *Mat. Sci. Eng. A-Struct., 2009, vol. 520, no. 1-2, pp. 105-113.*

84. Y.S. Lerner, V.E. Kouznetsov, G.V. Panteleev and J.T. Berry: *Foundry Manage. Technol., 2005, vol. 133, no. 3, pp. 46-57.*

85. R.Y Jou: *Key Eng. Mater., 2010, vols. 419-420, pp. 345-348.*

86. K.P. Keller: University of North Carolina, Chapel Hill, NC, unpublished research, 1997.

87. C. Alvin, W, Chu, Ching-Hung Cheng, Jyh-Tong Teng: *Microsystems, Packaging, Assembly and Circuits Technology Conference, 6th, 2011, Tai Pei, Taiwan, pp. 397-400.*

88. M.C. Yang: *IEEE Semi-Therm™ Symposium, 17th, 2001, Fort Worth, TX, pp. 102-106.*

89. E.J. Lavernia and N.J. Grant: *J. Mater. Sci., 1987, vol. 22, pp. 1521-1529.*

90. J.R. Pickens: *J. Mater. Sci., 1981, vol. 16, pp. 1437-1457.*

91. D.P. Bishop, B. Hofmann and K.R. Couchman: *Adv. Powder Metall. Part. Mater., Edited by H. Ferguson and D.T. Whychell, 2000, pp. 87-100.*

92. ASTM: *Annual book of ASTM Standards, 2005, ASTM International, West Conshohocken, PA, Section 2.*

93. Y.M. Kim, W.M. Griffith and F.H. Froes: *J. Metals, 1985, vol. 37, no. 8, pp. 27-33.*

94. P. Villars, A. Prince and H. Okamoto: *Handbook of ternary alloy phase diagrams, vol. 4, 1995, ASM International, Materials Park, OH, pp. 3918-3922.*

95. Y.S. Touloukian and C.Y. Ho: *Properties of Aluminum and Aluminum Alloys, no. 21, 1973, Thermophysical Properties Research Center, Perdue University, IN, p. 46.*

96. ASM: *ASM Metals Handbook, vol. 2, 2004, ASM International, Materials Park, OH, pp. 152-177.*

97. C. Lall and W. Heath: *Int. J. Powder Metall., 2000, vol. 36, no. 6, pp. 41-43.*

APPENDIX A - HEAT CAPACTY DATA

The following section shows DSC traces for the specific heat capacity of all of the experimental PM alloys tested.

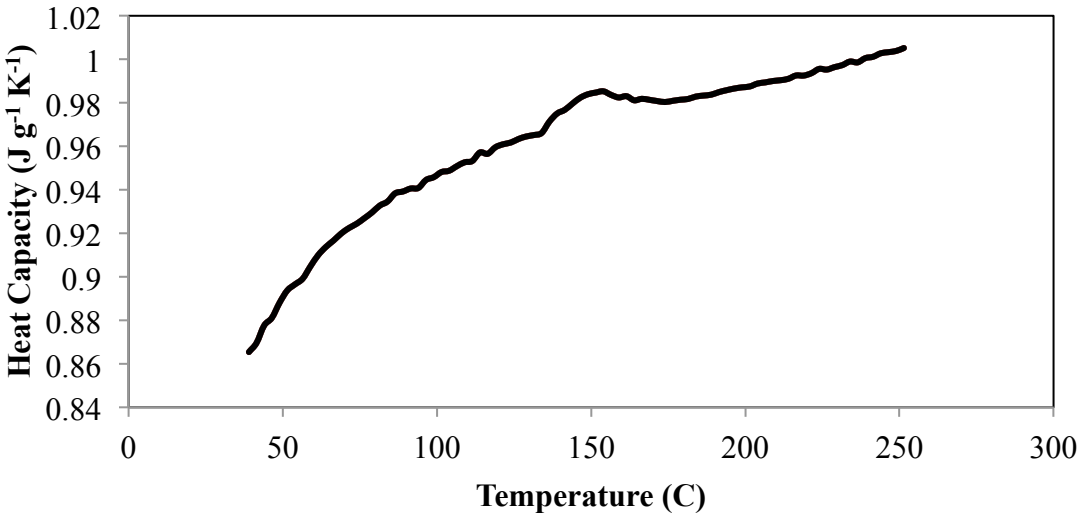

Figure A - 1. Specific heat capacity of Al-1.5Mg-0.4Sn with varying temperature.

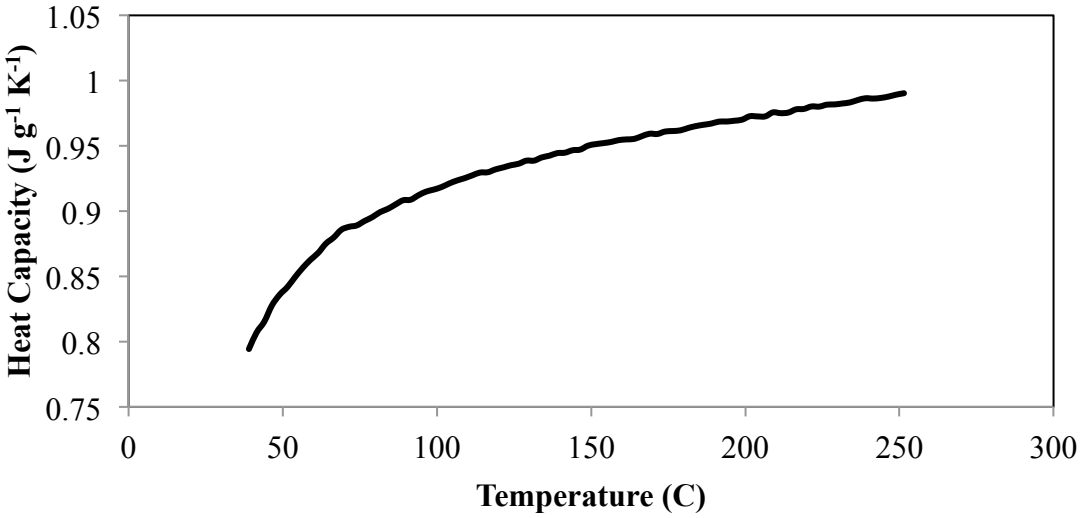

Figure A - 2. Specific heat capacity of Al-1.5Mg-0.6Sn with varying temperature.

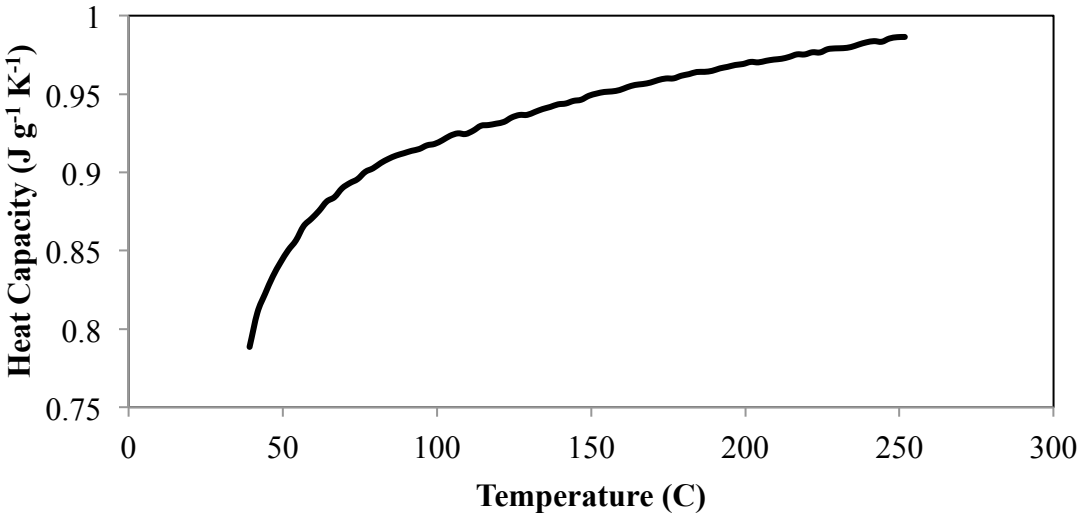

Figure A - 3. Specific heat capacity of Al-1.5Mg-0.8Sn with varying temperature.

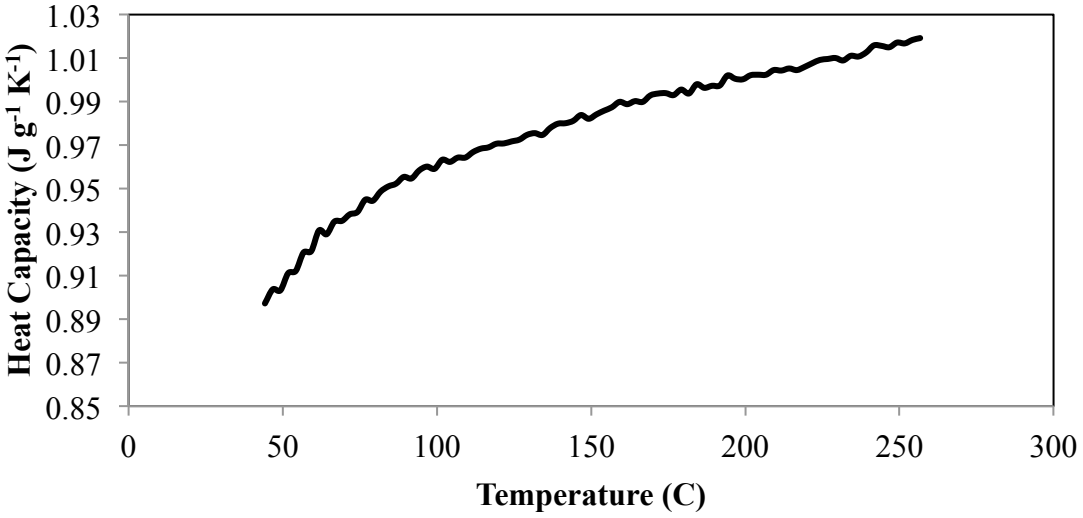

Figure A - 4. Specific heat capacity of Al-1.5Mg-1.0Sn with varying temperature.

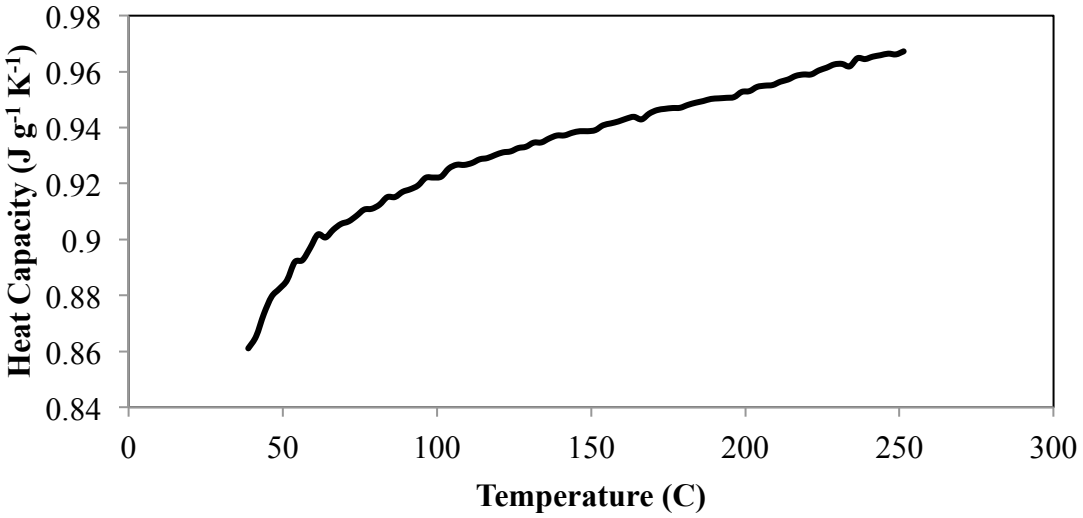

Figure A - 5. Specific heat capacity of Al-1.5Mg-1.2Sn with varying temperature.

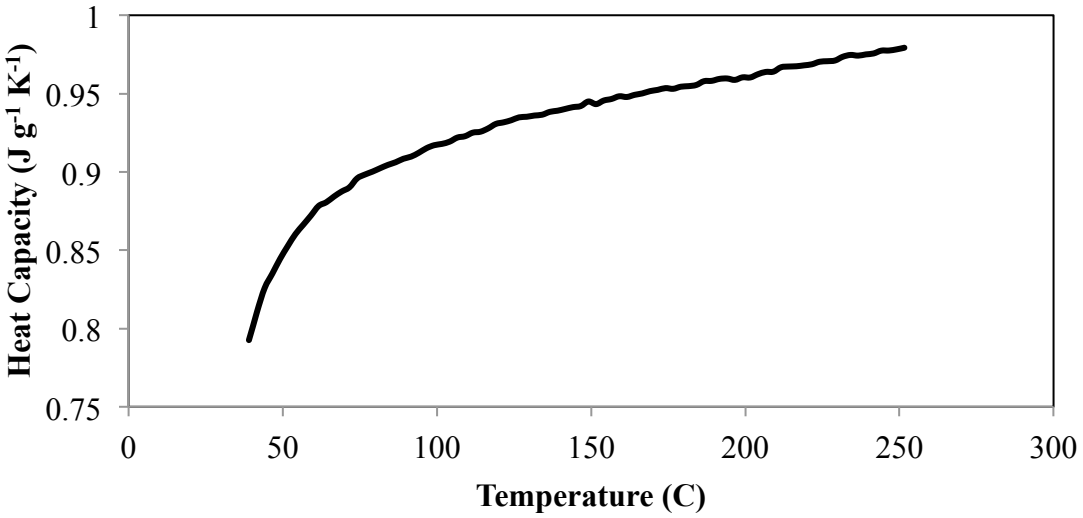

Figure A - 6. Specific heat capacity of Al-1.5Mg-1.4Sn with varying temperature.

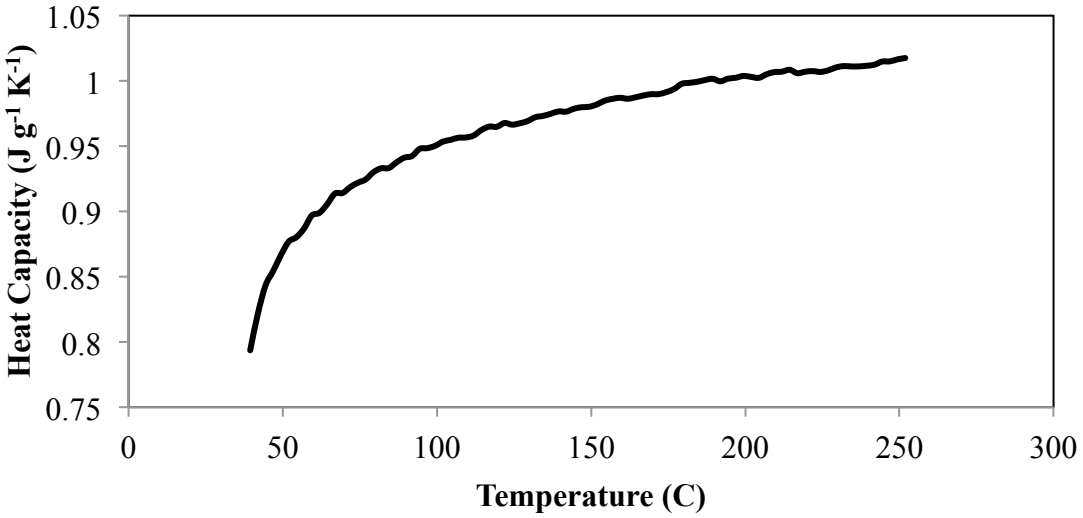

Figure A - 7. Specific heat capacity of Al-1.5Mg-1.6Sn with varying temperature.

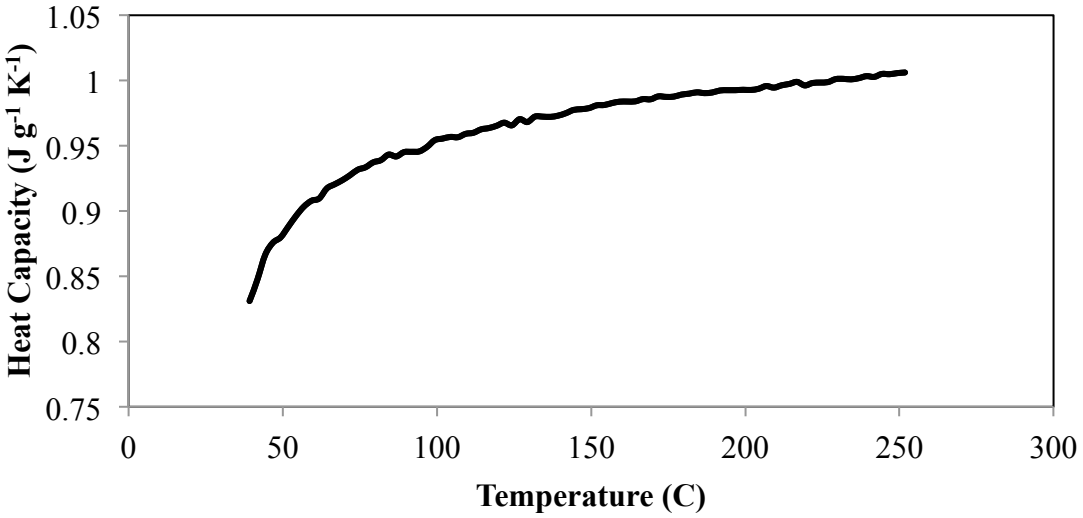

Figure A - 8. Specific heat capacity of Al-1.5Mg-1.8Sn with varying temperature.

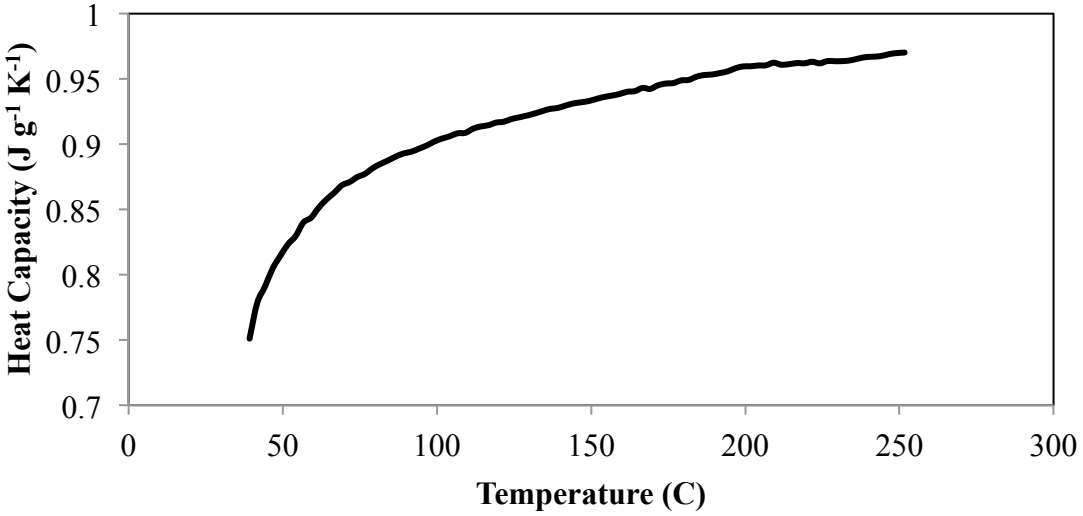

Figure A - 9. Specific heat capacity of Al-1.5Mg-2.0Sn with varying temperature.

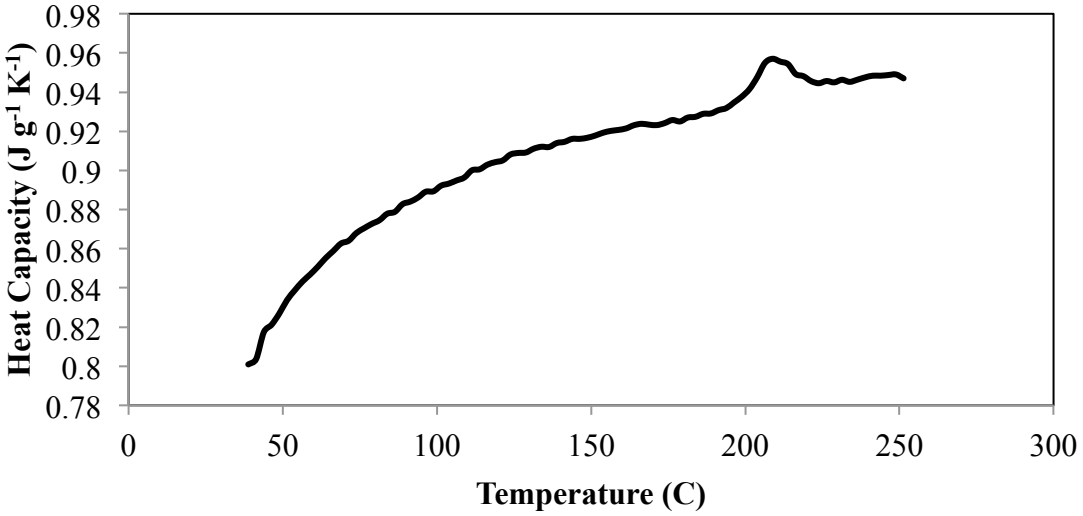

Figure A - 10. Specific heat capacity of Al-0.4Mg-1.5Sn with varying temperature.

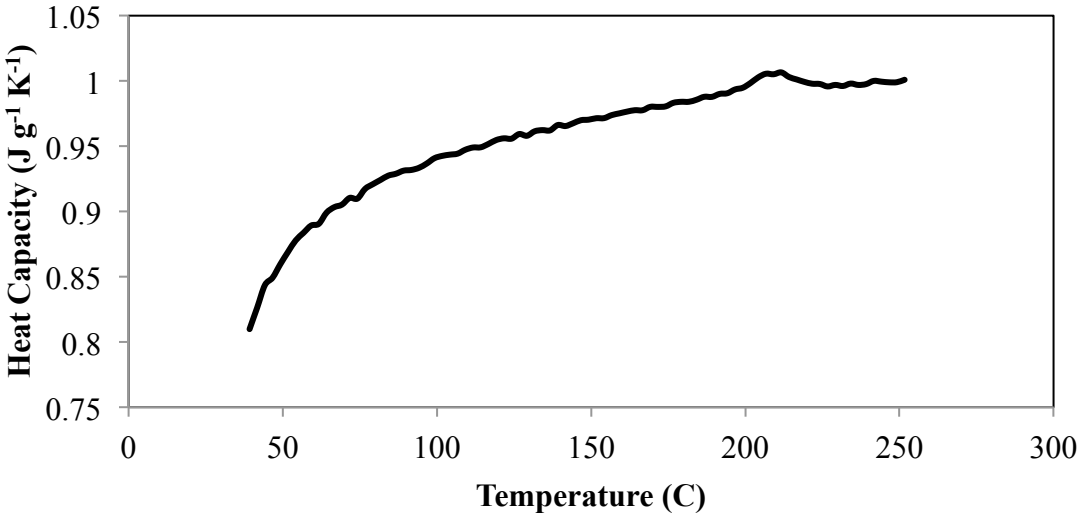

Figure A - 11. Specific heat capacity of Al-0.6Mg-1.5Sn with varying temperature.

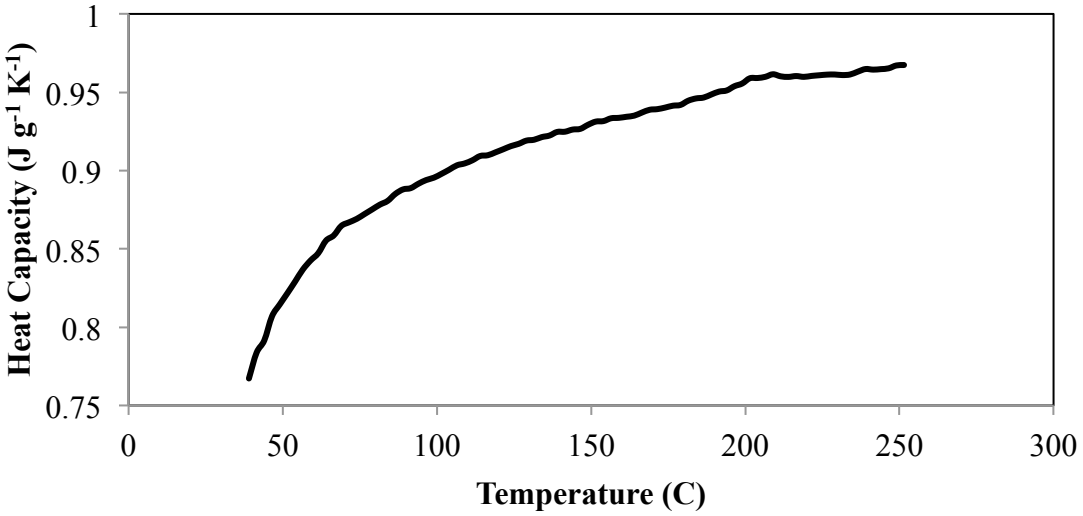

Figure A - 12. Specific heat capacity of Al-0.8Mg-1.5Sn with varying temperature.

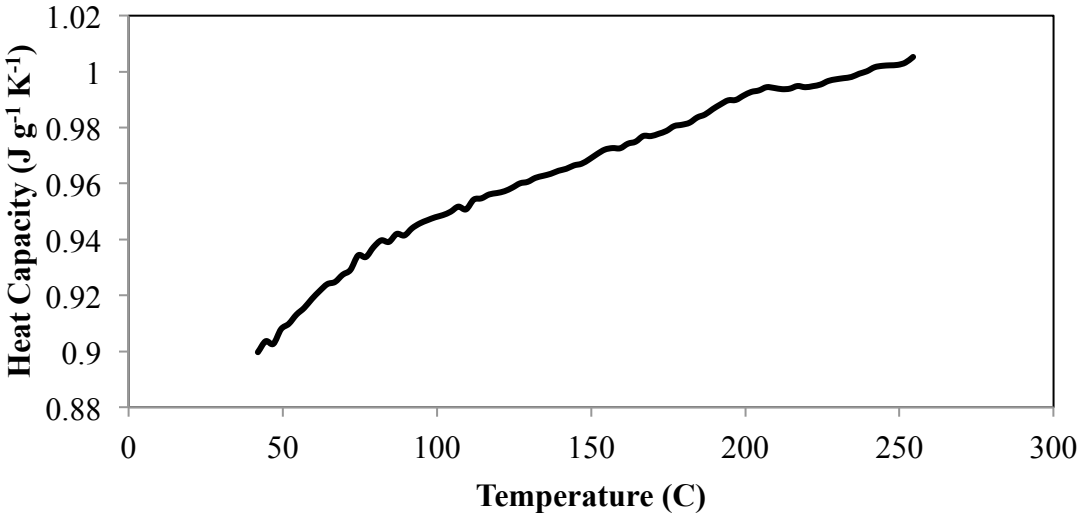

Figure A - 13. Specific heat capacity of Al-1.0Mg-1.5Sn with varying temperature.

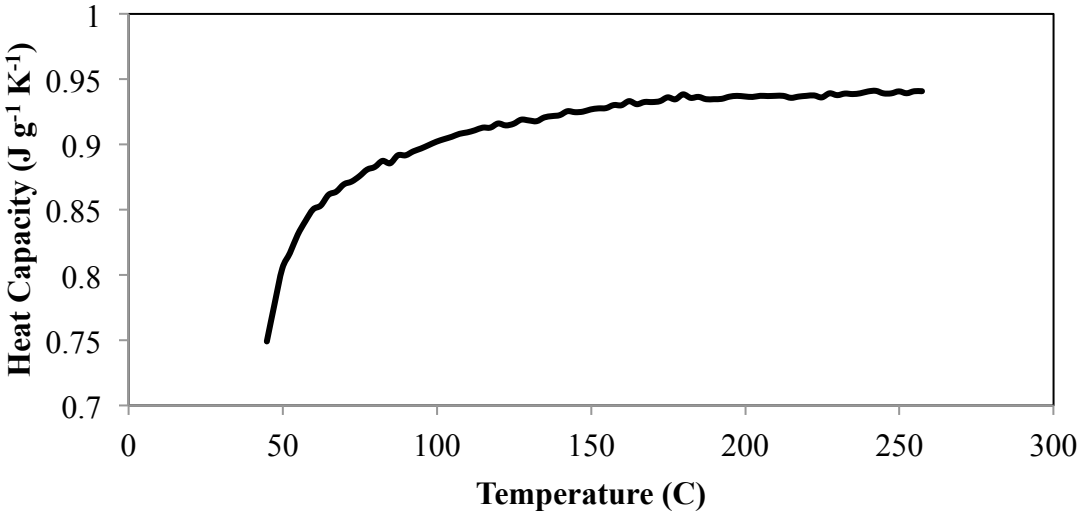

Figure A - 14. Specific heat capacity of Al-1.2Mg-1.5Sn with varying temperature.

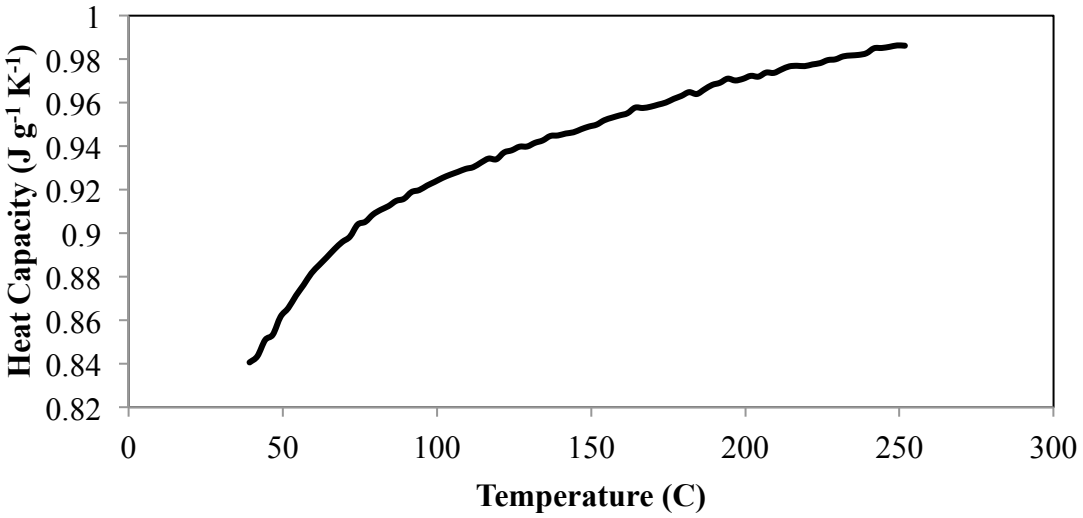

Figure A - 15. Specific heat capacity of Al-1.4Mg-1.5Sn with varying temperature.

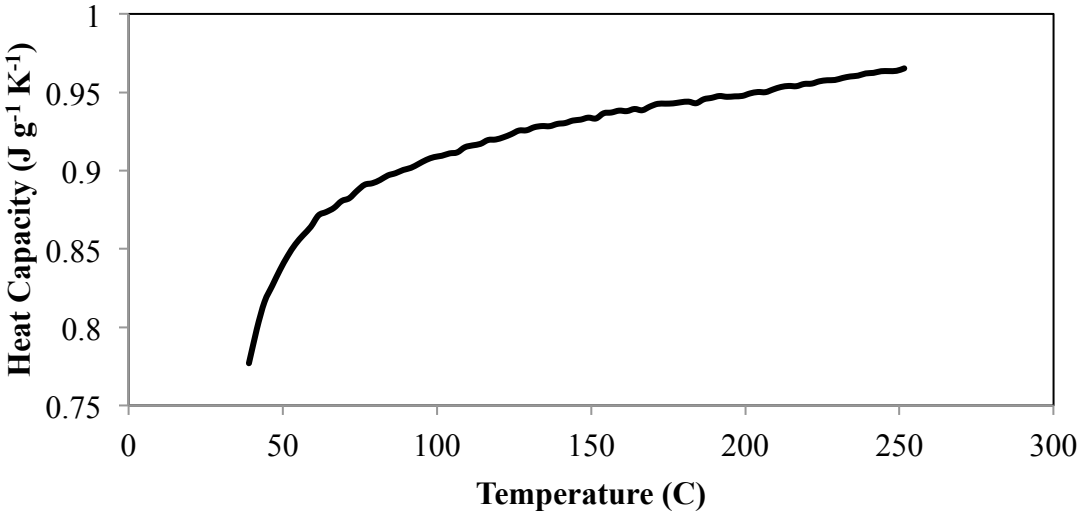

Figure A - 16. Specific heat capacity of Al-1.6Mg-1.5Sn with varying temperature.

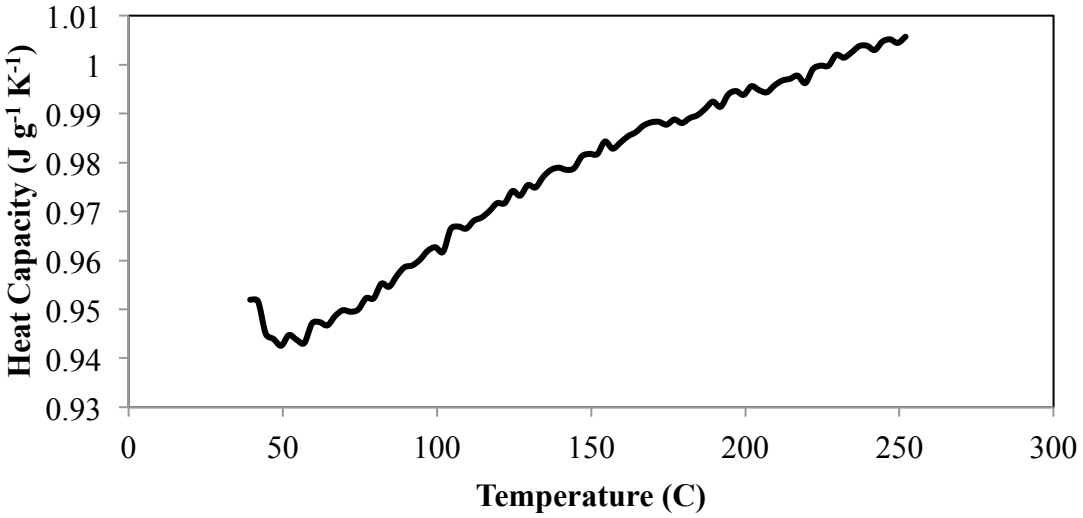

Figure A - 17. Specific heat capacity of Al-1.8Mg-1.5Sn with varying temperature.

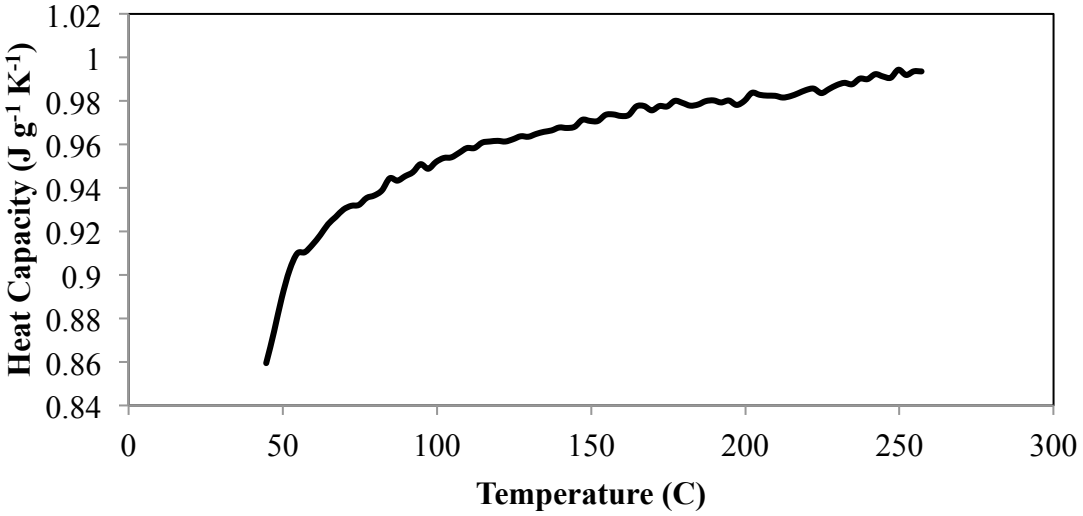

Figure A - 18. Specific heat capacity of Al-2.0Mg-1.5Sn with varying temperature.